# Deliverable D 4.3
# Thermomechanical characterization of subsystems finished

| | |
|---|---|
| Document type | **Deliverable D 4.3** |
| Document Version / Status | **1.6** |
| Primary Authors | **João Pereira, jpereira@civil.uminho.pt, UMINHO** |
| Distribution Level | **PU (Public)** |
| Project Acronym | **ATHOR** |
| Project Title | **Advanced THermomechanical multiscale mOdelling of Refractory linings** |
| Grant Agreement Number | **764987** |
| Project Website | www.etn-athor.eu |
| Project Coordinator | **Marc Huger, marc.huger@unilim.fr, UNILIM** |
| Document Contributors | **João Pereira, jpereira@civil.uminho.pt, UMINHO**<br>**Rafael Oliveira, rafael.oliveira@uc.pt, UMINHO**<br>**Alain Gasser, alain.gasser@univ-orleans.fr , UORL**<br>**Mahmoud Ali, mahmoud.ali@univ-orleans.fr, UORL** |

| Version | Date | Author (Organization) | Change | Page |
|---|---|---|---|---|
| 1.0 | 02.06.2021 | Rafael Oliveira | First version of the Deliverable created | All |
| 1.1 | 10.06.2021 | Mahmoud Ali | Review | All |
| 1.2 | 15.06.2021 | Alain Gasser | Review | All |
| 1.3 | 20.06.2021 | João Pereira | Review | All |
| 1.4 | 23.06.2021 | Alain Gasser, Glyn Derrick | Formatting and English check | All |
| 1.5 | 30.06.2021 | Alain Gasser, Mahmoud Ali, Glyn Derrick | Updated data | All |
| 1.6 | 07.07.2021 | Marc Huger, Glyn Derrick | Final Check | All |



European Commission
Horizon 2020
European Union funding
for Research & Innovation

Table of contents



# 1 Introduction

This report will gather the data obtained in the different experimental campaigns on the thermomechanical behaviour of refractory masonry at the subsystem scale. It includes the experimental campaigns performed in masonry wallets at UMINHO and RHI-Magnesita. The objective is to characterize the refractory masonry (composite) constituted of alumina spinel brick used in the working lining (layer in contact with liquid steel) of the steel ladle. The working lining of the steel ladle is built up from thousands of tapered shape bricks. However, for the sake of simplicity, while building the wallets, new cuboid bricks cast were used in the two experimental campaigns. Masonry wallets will be tested under different conditions: (a) uniaxial compression (UMINHO); (b) bi-axial compression (RHI); (c) at room and high temperatures (UMINHO and RHI). The obtained results will be used to validate the numerical models developed within WP3 at a subsystem scale.

# 2 Uniaxial compression tests

During service conditions, dry-stacked masonry used in the refractory linings of industrial vessels are subjected to high compressive loads, creep, abrasion, corrosion and thermal shock. The stability of these linings is essential to ensure the safety and efficiency of the industrial process. However, very few experimental studies have been conducted on the behaviour of dry-stacked refractory masonry at ambient and high temperatures at large scale. There is a need for more research to obtain an accurate understanding of the behaviour of these masonry structures, as highly nonlinear behaviour, cracks due to bricks' height imperfections and brittle failure has been observed. Nevertheless, only a few studies can be found in the literature with regards to sub-system scale (wallets) (Prietl, 2006; Prietl et al, 2006).

This section intends to present a test set-up that was previously used to test concrete masonry wallets at high temperatures (Lopes et al, 2017; Oliveira et al, 2020). Due to the high mechanical resistance of the tested material, the structural capacity of the reaction frame was improved, the columns and beams were replaced by profiles with a larger cross-section. A hydraulic actuator (3 MN) and a load cell (5 MN) with higher capacity were used. Moreover, DIC (Dupre et al, 2018; Belrhiti et al, 2017) was used to map the in-plane displacement fields.

The objective of this work was to study the behaviour of dry-stacked refractory masonry walls at ambient and high temperatures under uniaxial compression loads. Five different test series have been studied, two series at ambient temperature and three series at high temperatures. The experimental program comprised of fourteen tests (performed at ambient and high temperatures) divided in five series (Table 1):

- Test series S01.AT.LBC: carried out at Ambient Temperature (AT) with the objective of evaluating the Load Bearing Capacity (LBC) of the wall.
- Test series S02.AT.CIC: carried out at Ambient Temperature (AT) aiming to assess the behaviour of the dry stacked masonry under CyclIC loads (CIC).
- Test series S03.HT.LL8: carried out at High Temperatures (HT) aiming to evaluate the thermomechanical performance of the masonry under constant Load Level of 8 MPa (LL8). The mechanical load was applied and then the specimen was heated according to the standard ISO 834-1 (1999).

- Test series S04.HT.RTE: tested at High Temperatures (HT) aiming to assess the behaviour of masonry under Restrained Thermal Elongation (RTE). First, a mechanical load of 5 MPa was applied to the specimen, the hydraulic jack is blocked at its current position and the specimen was heated with the same heating rate of test series S03.HT.LL8.
- Test series S05.HT.LL10: carried out at High Temperatures (HT) aiming to evaluate the thermomechanical behaviour of the masonry wall with a higher slenderness ratio under a 10 MPa Load Level (LL10). The mechanical load was applied and then the specimen was heated with the same heating rate of S03.HT.LL8 and S04.HT.RTE.

**Table 1 – Test series for the uniaxial tests.**

<table>
<tr><th>Series</th><th>Specimen</th><th>Temperature of the test</th><th>Thermal restraining</th><th>Type of control</th><th>Load level</th></tr>
<tr><td rowspan="3">S01.AT.LBC</td><td>S01.AT.LBC.01</td><td rowspan="6">Ambient Temperature</td><td rowspan="3">None</td><td rowspan="3">Displacement</td><td rowspan="3">Up to failure</td></tr>
<tr><td>S01.AT.LBC.02</td></tr>
<tr><td>S01.AT.LBC.03</td></tr>
<tr><td rowspan="3">S02.AT.CIC</td><td>S02.AT.CIC.01</td><td rowspan="3">None</td><td rowspan="3">Displacement</td><td rowspan="3">Cyclic loading<br>1, 2, 5 and 8 MPa</td></tr>
<tr><td>S02.AT.CIC.02</td></tr>
<tr><td>S02.AT.CIC.03</td></tr>
<tr><td rowspan="3">S03.HT.LL8</td><td>S03.HT.LL8.01</td><td rowspan="8">High Temperatures</td><td rowspan="3">Constant loading and no thermal restraining</td><td rowspan="3">Load</td><td rowspan="3">8 MPa</td></tr>
<tr><td>S03.HT.LL8.02</td></tr>
<tr><td>S03.HT.LL8.03</td></tr>
<tr><td rowspan="3">S04.HT.RTE</td><td>S04.HT.RTE.01</td><td rowspan="3">Thermal restraining</td><td rowspan="3">Displacement</td><td rowspan="3">Pre-load: 5 MPa<br>+ Effects of restrained thermal elongation</td></tr>
<tr><td>S04.HT.RTE.02</td></tr>
<tr><td>S04.HT.RTE.03</td></tr>
<tr><td rowspan="2">S05.HT.LL10</td><td>S05.HT.LL10.01</td><td rowspan="2">Constant loading and no thermal restraining</td><td rowspan="2">Load</td><td rowspan="2">10 MPa</td></tr>
<tr><td>S05.HT.LL10.02</td></tr>
</table>

## 2.1 TEST SETUP

The experimental tests were carried out at the Laboratory of Testing Materials of the University of Coimbra, in Portugal. The test setup has been used before (Lopes et al, 2017; Oliveira et al, 2020) and was improved for this experimental campaign. The schematic view of the test set-up is shown in Figure 1. The test set-up consisted of one reaction frame composed of two HEB500 columns and two overlapping HEB600 beams (4500 mm span). The hydraulic jack had the capacity of 3 MN and the load cell used to measure the applied load had the capacity of 5 MN. For the experiments performed at high temperatures one modular electric furnace (45 kVA) was used to heat the specimens. The hydraulic jack applied the load in the plane of the wall using two load beams. The top one was a HEB240 steel beam and the bottom one was a composite beam (tubular steel section filled with concrete). The verticality of the load application was ensured by two lateral steel frames working as guides. The hydraulic jack was controlled by a servo hydraulic central unit W+B NSPA700/DIG2000. Aiming to limit the heat loses, two masonry columns were built at the edges of the specimens, the gap between the masonry wallet and columns (15 mm) was filled with rockwool, therefore, there was no mechanical restraint at the sides of the specimen. The reaction frame was bolted to the laboratory slab by steel anchors (ø40 mm). The specimens were built in the reaction slab over a 10 mm grout layer. Rockwool was used for the thermal insulation of the reaction slab and to fill the gap between the specimens and the lateral masonry columns. The pictures of the experimental set-up are presented in Figure 2 and Figure 3 for the tests at ambient and high temperatures, respectively. The load cell used to measure the loading applied to the specimen was placed between the hydraulic jack's head and the loading beams (Figure 4). The connection between the hydraulic jack and the load beams was pinned.

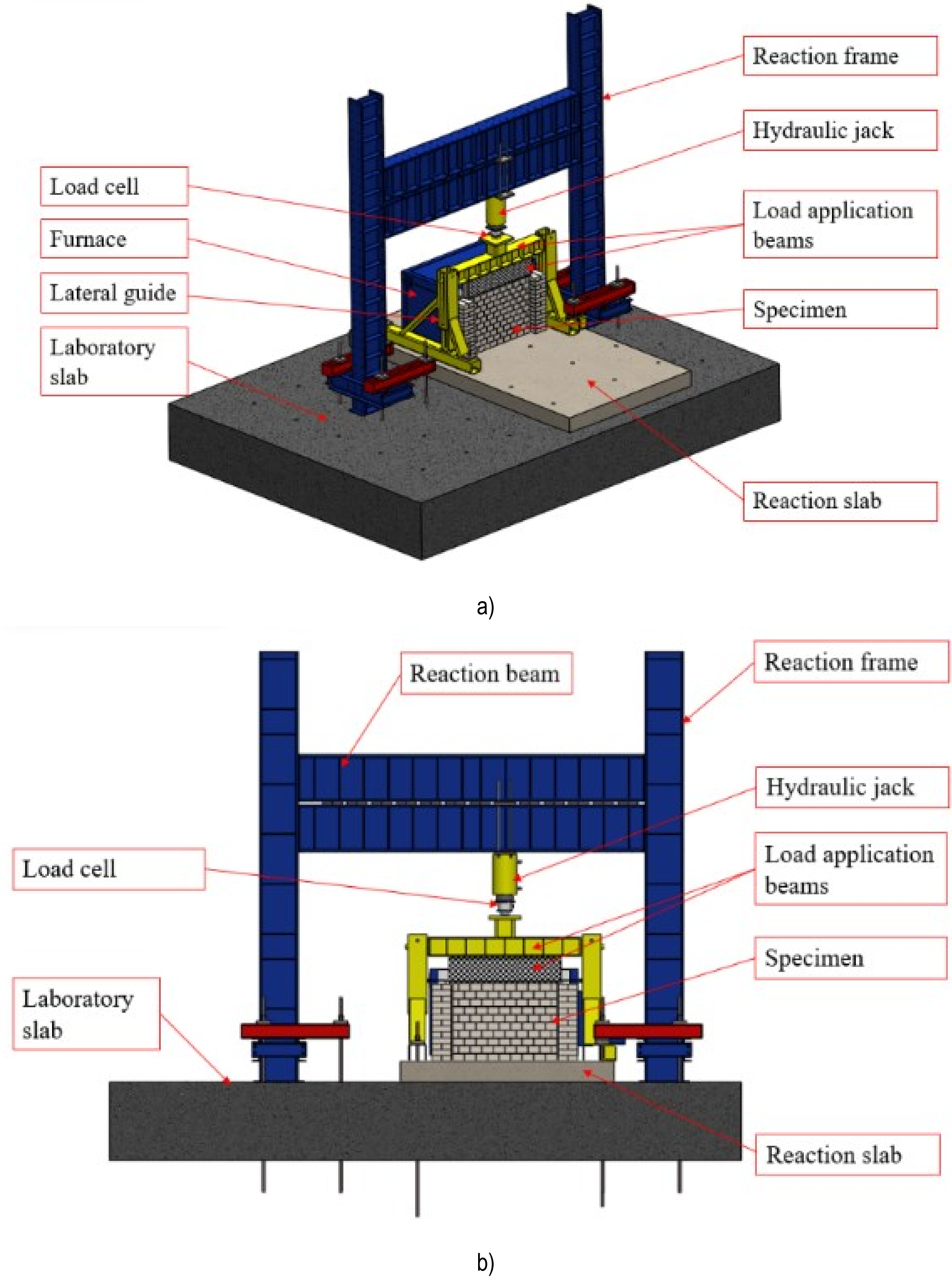


**Figure 1 – Test set-up: a) Isometric view and b) Front view.**

a) b)

Figure 2 – Test set-up at ambient temperatures: a) Front view and b) Back view.

a) b)

Figure 3 – Test set-up at high temperatures: a) Front view and b) Detail of bottom insulation.

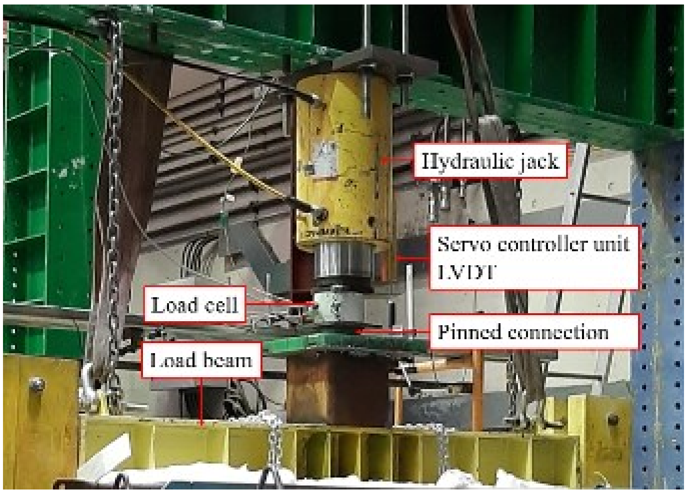


Figure 4 – Hydraulic jack and load cell details.

Three Linear Variable Differential Transformers (LVDTs) placed at the top of the steel loading beam were used to measure the In-Plane displacements (LVDT-IP). The distance between the LVDTs was 150 mm for test series S01.AT.LBC and 600 mm for the others test series. The positioning of the three in-line LVDTs allowed to identify possible rigid body rotations in the load application beam. Three laser LVDTs were used to measure the Out-of-Plane displacements (LVDT-OoP) in the specimens of test series S01.AT.LBC and five LVDTs were used for the other series. Due to the temperatures developed in the specimens, non-contact LVDTs were chosen (Panasonic HL-G1 series). The positioning of the LVDTs is detailed in Figure 5.

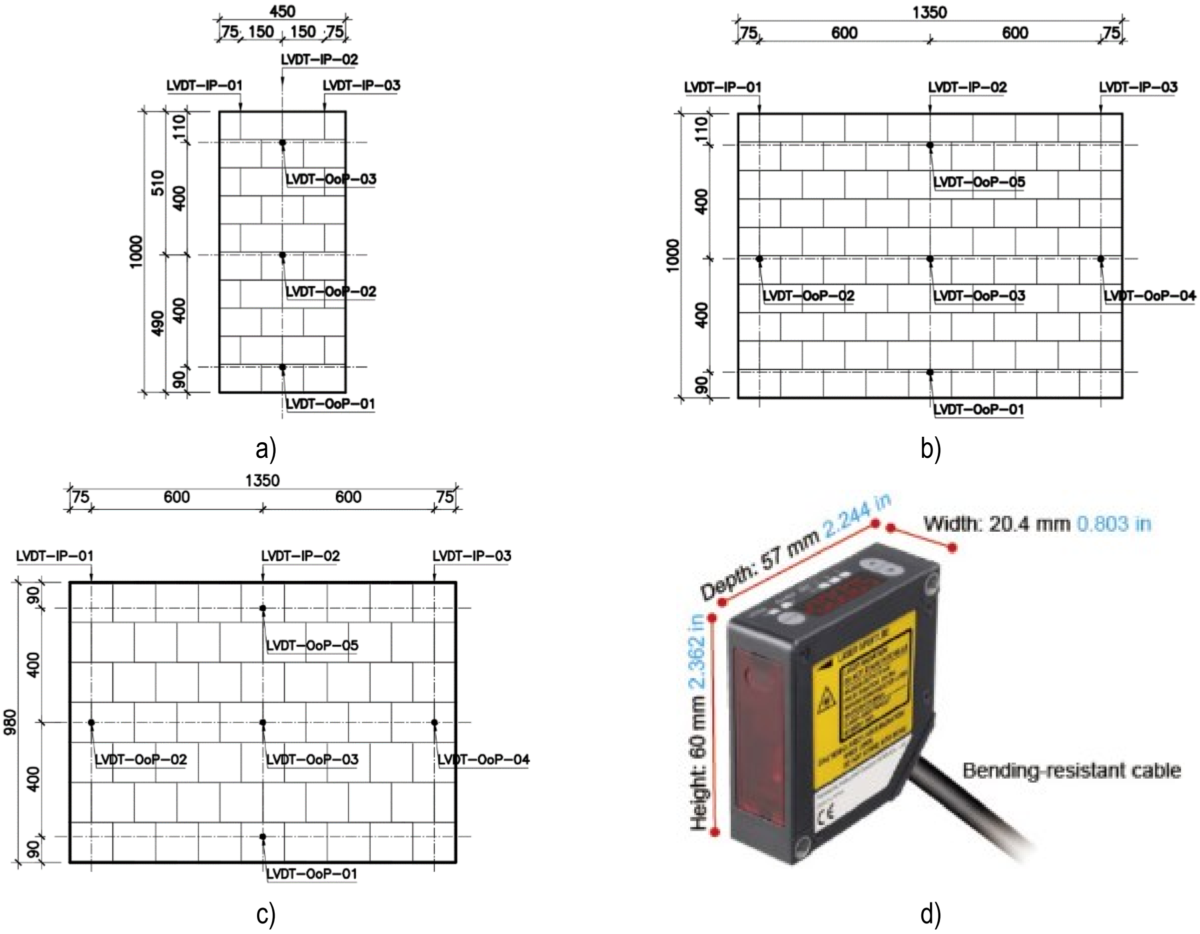


**Figure 5 – LVDTs instrumentation: a) Series S01.AT.LBC, b) Series S02.AT.CIC, S03.HT.LL8 and S04.HT.RTE, c) Series S05.HT.LL10, d) Detail of the laser LVDT.**

Digital image correlation (DIC), a contactless measurement technique, was used to measure the in-plane displacements fields. This technique was developed in the beginning of the 1980's and improved over time (Besnard et al, 2006). The basic principle is to compare two images that represent different states of the specimen, a reference and a deformed condition. The technique assumes that the grey level distribution follows the material strains and remains homogenous in the subset (Dupre et al, 2018; Belrhiti et al, 2017). An 18 MPx (5184 x 3486) camera was used for image acquisition and three LED reflectors were used to provide suitable lighting conditions. The image processing was performed using subsets of 100 × 100 pixels. The speckle pattern application had the following steps: *i*) the bricks were laid on a horizontal plane; *ii*) the speckle pattern was applied by means of an aerograph; *iii*) a dwell time of 48 hours was considered for drying. The speckle pattern application, its details and the DIC system are shown in Figure 6.

The thermal instrumentation comprised eighteen type K wire thermocouples (TC) embedded in the bricks (10 mm depth). Nine installed in the hot face (TC-HF) and nine in the cold face (TC-CF), as detailed in Figure 7. The holes used to install the TCs (ø6 mm) were made in the bricks using diamond crown drills. Subsequently, the thermocouples were put in place and grout was used to close the hole. Additionally, one type K probe thermocouple was used to feed the furnace controller and one type K probe thermocouple was used to record the temperature in the furnace. The type K thermocouples are composed of Nickel-Chromium / Nickel-Alumel alloys and can operate between -270 ºC and 1260 ºC.

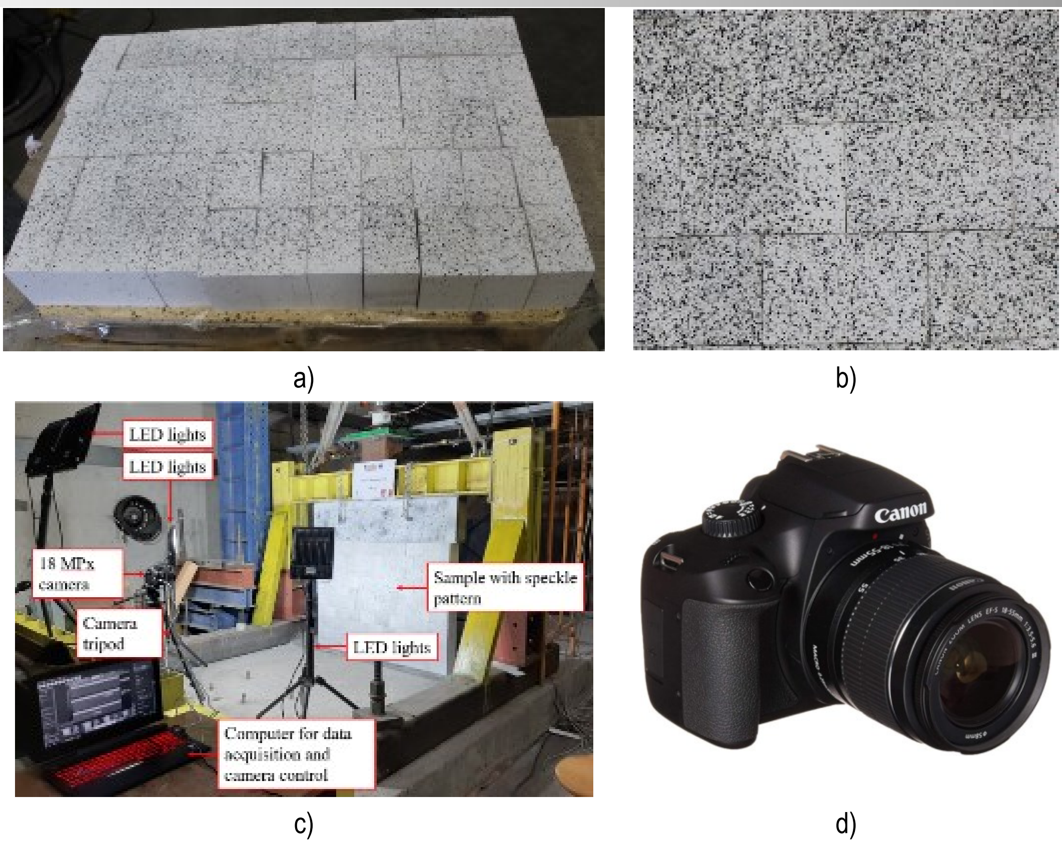


Figure 6 – DIC: a) Speckle pattern preparation, b) Details of the speckle pattern, c) DIC set-up, d) Camera.

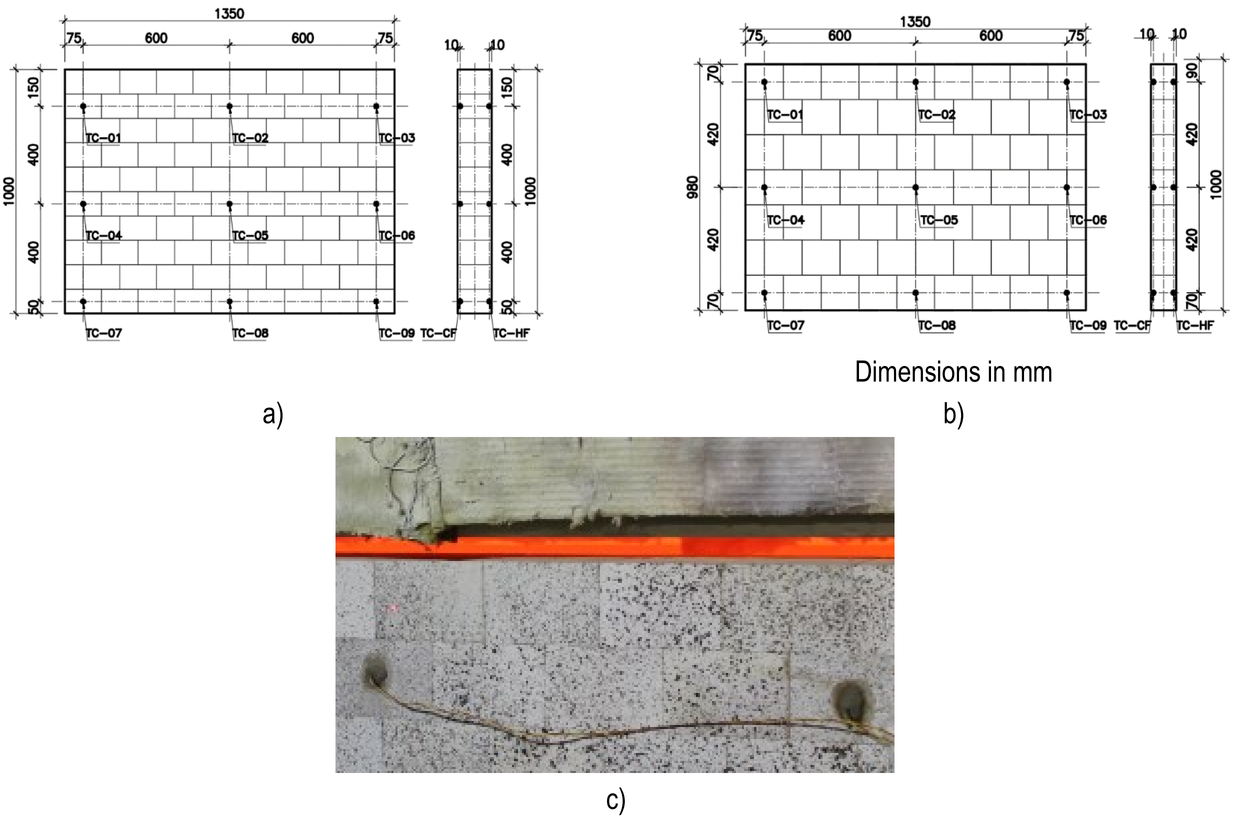


Figure 7 – Thermal instrumentation: a) Test series S03 and S04, b) Test series S05 and c) Detail of thermocouples embedded in the bricks.

## 2.2 SPECIMENS AND TEST PROCEDURE

The specimens consisted of dry-stacked masonry walls made of alumina spinel bricks. In order to fully characterize the masonry thermomechanical behaviour, three different configurations were used in the tests. Figure 8 presents the general arrangement of the specimens. The choice of the thickness for test series S01 to S04 (140 mm) was based on the usual thickness of the working lining of steel ladles. For test series S05, a smaller thickness (100 mm) was used to increase the slenderness of the wall. The length of the wall for test series S01 (450 mm) was chosen based on the structural capacity of the loading frame and the maximum capacity of the hydraulic jack, as this series aims to assess the loadbearing capacity of the wall. The length of the specimens used in test series S02 to S05 (1350 mm) was chosen based on the dimensions of the opening of the electric furnace used.

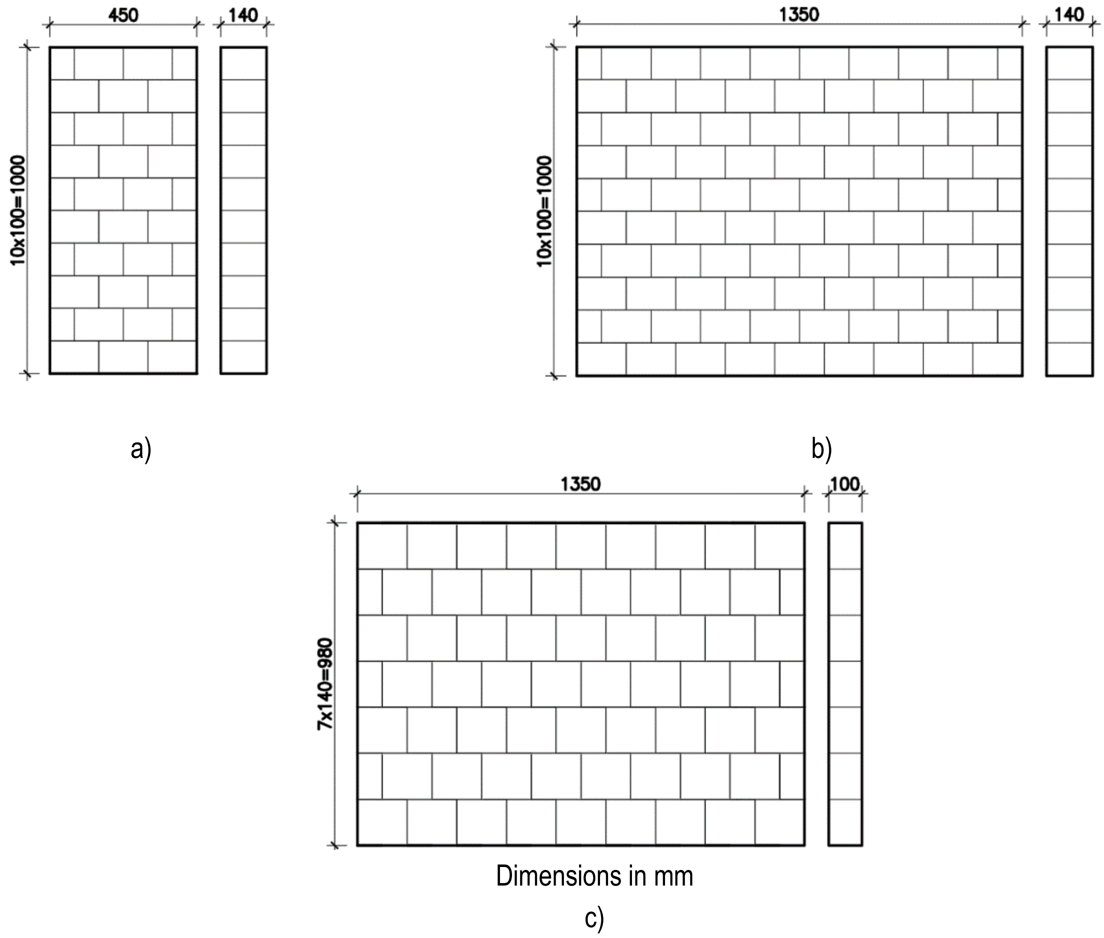


**Figure 8 – Uniaxial specimen dimensions:**
**a) Test series S01.AT.LBC, b) Test series S02.AT.CIC, S03.HT.LL8 and S04.HT.RTE and c) Test series S05.HT.LL10.**

The following test procedures were used in the different test series:

- **Test series S01.AT.LBC:** The objective of test series S01.AT.LBC was to assess the loadbearing capacity of the refractory masonry walls. The test procedure in series S01.AT.LBC had the following steps: *i*) the masonry specimens were built in the testing system; *ii*) the loading beams were placed on the top of the specimens using a crane; *iii*) the instrumentation was installed; *iv*) the loadbearing capacity test was performed under displacement control at a rate of 0.01 mm/s up to failure of the specimen.
- **Test series S02.AT.CIC:** The objective of test series S02.AT.CIC was to assess the behaviour of refractory masonry under cyclic loading. Steps *i*, *ii* and *iii* of this test procedure were similar to the ones presented for test series S01.AT.LBC. Then: *iv*) the test was performed under displacement control at a rate of 0.01 mm/s; *v*) the wall was submitted to four loading and unloading cycles with increasing load, to the following stress levels: 1, 2, 5 and 8 MPa. The specimens were not tested up to the failure.
- **Test series S03.HT.LL8:** Series S03.HT.LL8 was tested at high temperatures. Steps *i*, *ii* and *iii* of the test procedure were similar to the ones presented for series S01.AT.LBC. Then: *iv*) the specimen was loaded under displacement control at a rate of 0.01 mm/s up to 8 MPa at ambient temperature, *v*) the control procedure was changed to load control

and set to keep the current load; *vi*) the furnace was turned on and the specimen was heated according to the standard fire curve ISO 834-1 (1999); *vii*) the wall was monitored for five hours: the temperatures, applied load, in-plane and out-of-plane displacements were recorded. The specimens were not tested up to the failure due to limitations on the maximum operating time of the furnace.

- **Test series S04.HT.RTE:** The objective of series S04.HT.RTE was to assess the mechanical behaviour of refractory masonry walls subjected to restrained thermal elongation. Steps *i*, *ii* and *iii* of the test procedure were similar to the ones presented for series S01.AT.LBC. Then: *iv*) the specimen was loaded under displacement control at the rate of 0.01 mm/s up to 5 MPa; *v*) the hydraulic jack was fixed at its current position; *vi*) the furnace was turned on and the specimen was heated according to the standard fire curve ISO 8341-1 (1999); *vii*) the wall was monitored for five hours: the temperatures, applied load, in-plane and out-of-plane displacements were recorded. The specimens were not tested up to the failure due to limitations on the maximum operating time of the furnace.
- **Test series S05.HT.LL10**: The objective of series S05.HT.LL10 was to assess the mechanical behaviour of refractory masonry walls subject to constant load (10 MPa) under increasing temperature. Steps *i*, *ii* and *iii* of the test procedure were similar to the ones presented for series S01.AT.LBC. Then: *iv*) the specimen was loaded under displacement control at a rate of 0.01 mm/s up to 10 MPa at ambient temperature, *v*) the control procedure was changed to load control and set to keep the current load; *vi*) the furnace was turned on and the specimen was heated according to the standard fire curve ISO 834-1 (1999); *vii*) the wall was monitored for five hours: the temperatures, applied load, in-plane and out-of-plane displacements were recorded. Failure occurred to the combined stress level and temperature increase.

## 2.3 RESULTS AND DISCUSSION

The experimental results are presented and discussed in this section. For each test series, results in terms of displacements, strains, forces, stresses, temperatures are presented and discussed. Wherever possible, comparisons with literature results are made.

### 2.3.1 Test series S01.AT.LBC

Test series S01.AT.LBC aimed to evaluate the loadbearing capacity of the specimen. The evolution of the in-plane displacements measured in the tests are presented in Figure 9. A small scattering of the in-plane displacements was observed, as expected for masonry walls. The differences in the readings of LVDT-IP-1 and LVDT-IP-3 indicated a slight rotation of the load application beam. The positive displacement rate at LVDT-IP-1 of specimen S01.AT.LBC.02 (Figure 9b) and the LVDT-IP-3 of specimen S01.AT.LBC.03 (Figure 9c) also indicated this rotation.

The maximum force was 1100 kN (17.5 MPa), 851 kN (13.5 MPa) and 1417 kN (22.5 MPa) for the tested specimens, respectively. The maximum average in-plane displacement by the end of the test was 4.71 mm ($\varepsilon$ = 0.00473), 5.11 mm ($\varepsilon$ = 0.00465) and 6.12 mm ($\varepsilon$ = 0.00607), respectively.

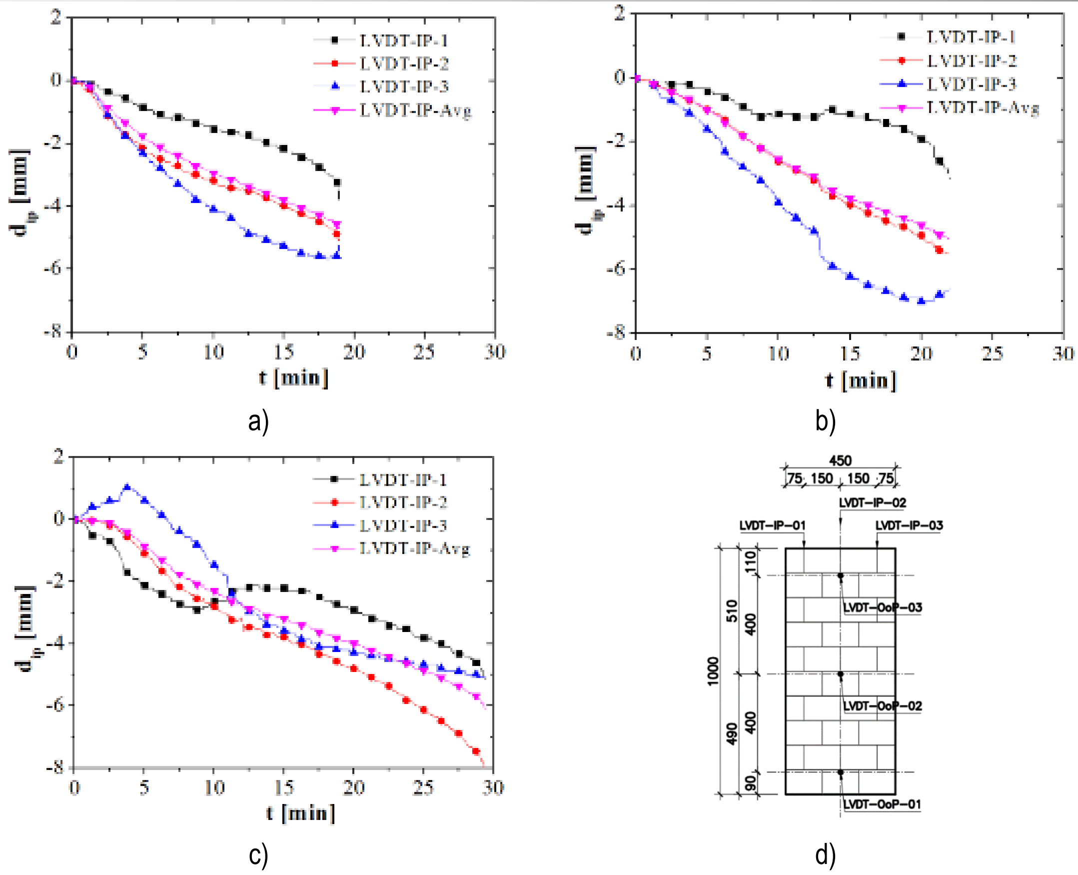


**Figure 9 – Test series S01.AT.LBC – In-plane displacements:**
**a) S01.AT.LBC.01, b) S01.AT.LBC.02, c) S01.AT.LBC.03 and d) LVDT locations.**

The stress-strain curves of test series S01.AT.LBC are presented in Figure 10. Three different stages were observed: *i*) joint closure; *ii*) linear behaviour; *iii*) plastic and damageable behaviour and failure. During stage *i*, the tangent Young's modulus of the wall increased from almost zero up to 6.2 GPa. In this stage, crushing of brick's initial non-plane surfaces occurs (Allaoui et al, 2018; Gasser et al, 2004; Andreev et al, 2012). The joint closure curve is strongly heterogeneous along the joints as it is influenced by the bricks shape imperfections, bricks surface roughness and construction faults (Allaoui et al, 2018; Gasser et al, 2004; Andreev et al, 2012; Zahra et al, 2018; Ngapeya et al, 2018).

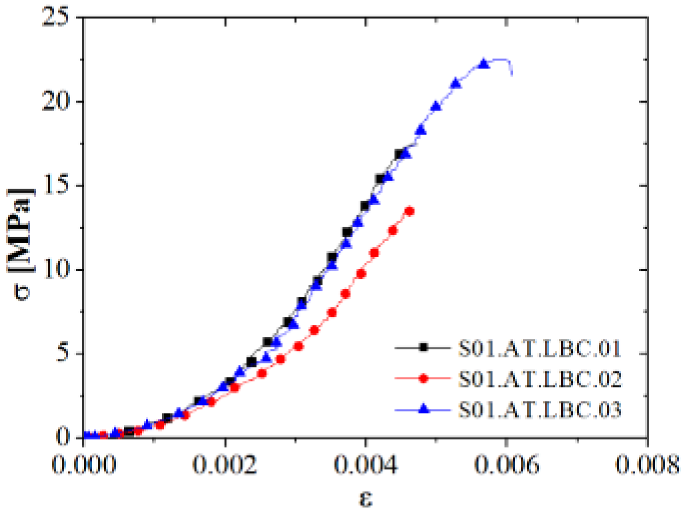


**Figure 10 – Test series S01.AT.LBC – Stress-strain curves.**

During stage *ii*, a linear behaviour was observed in the stress-strain curves, however the Young´s modulus of the wall ($E_{wall}$ = 6.2 GPa) was significantly smaller than the Young's modulus of the brick ($E_{brick}$ = 28.8 GPa), indicating a non-homogeneous stress distribution in the wall, most likely caused by the bricks' shape imperfections. Ngapeya et al (2018) reported a similar behaviour where the non-homogeneous stress distributions along the wall led to a reduction of its structural capacity. The non-homogeneous stress distribution in the wall was also evidenced by the DIC analysis. Figure 11 presents the measured in-plane displacement fields for specimens S01.AT.LBC.02 and S01.AT.LBC.03.

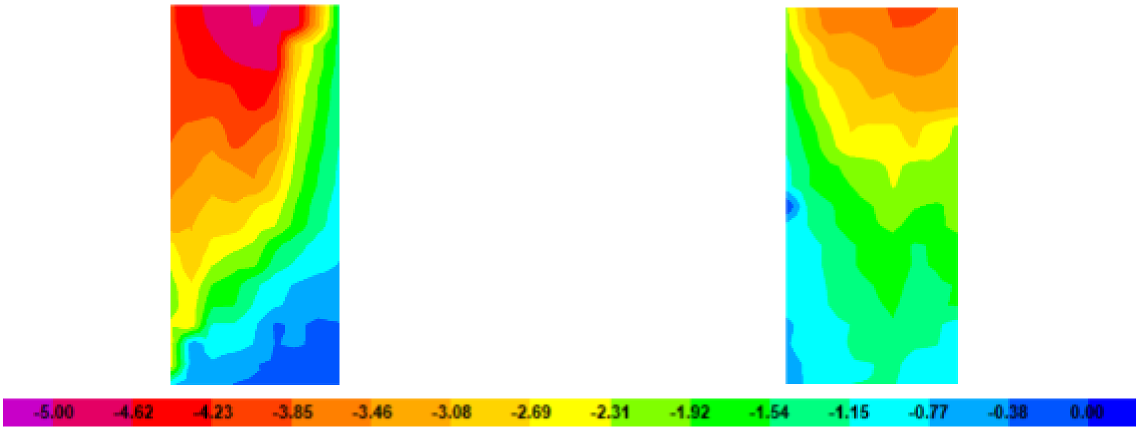


a) b)

**Figure 11 – Test series S01.AT.LBC – In-plane displacement fields: a) S01.AT.LBC.02 and b) S01.AT. LBC.03 (in mm).**

During stage *iii*, a slight decrease of the wall's Young's modulus was observed, which is typical on masonry due to the development of cracks in the material. These cracks are mostly thin and distributed in the specimen. A brittle failure was observed in all specimens. The compressive strength for specimens S01.AT. LBC.01, S01.AT. LBC.02 and S01.AT. LBC.03 was 17.5 MPa, 13.5 MPa and 22.5 MPa, respectively. Specimen S01.AT.LBC.02, presented a low compressive strength due to an uneven load distribution in the specimen, caused by a relatively large shape imperfection, as observed in the DIC analysis (Figure 11a). The average compressive strength was 17.8 MPa (20.0 MPa if specimen S01.AT.LBC.02 is disregarded). The failure sequence is presented in Figure 12. Figure 13 presents the picture taken by the DIC camera during the failure of specimen S01.HT.LBC.02.

a) b) c)

**Figure 12 – Test series S01.HT.LBC – Images of testing sequence: a) Before testing, b) Failure and c) After testing.**



European Commission
Horizon 2020
European Union funding
for Research & Innovation

Figure 13 – Test series S01.HT.LBC.02 – Specimen failure.

### 2.3.2 Test series S02.AT.CIC

Test series S02.AT.CIC aimed to evaluate the behaviour of refractory masonry under cyclic load. The evolution of the in-plane displacements measured in the tests are being presented in Figure 14. As expected, a small scattering of the in-plane displacements was observed.

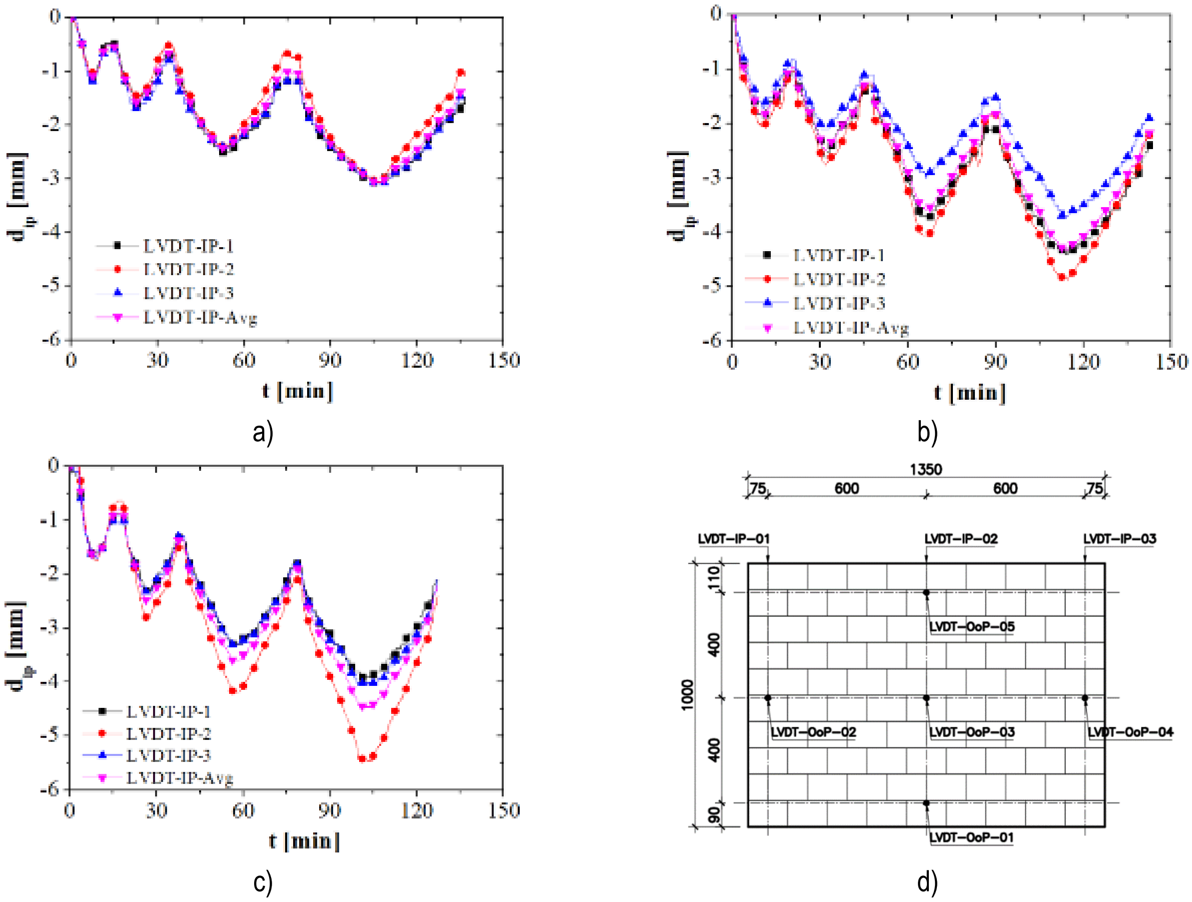


Figure 14 – Test series S02.AT.CIC – In-plane displacements:
a) S02.AT.CIC.01, b) S02.AT.CIC.02, c) S02.AT.CIC.03 and d) LVDT locations.

Figure 15 presents the stress-strain curves obtained experimentally for test series S02.AT.CIC. Based on the stress-strain curve, it is possible to observe an increasing residual strain after each loading cycle. This residual strain was caused by the crushing of initially non-flat brick's surfaces in contact at the bed joints.

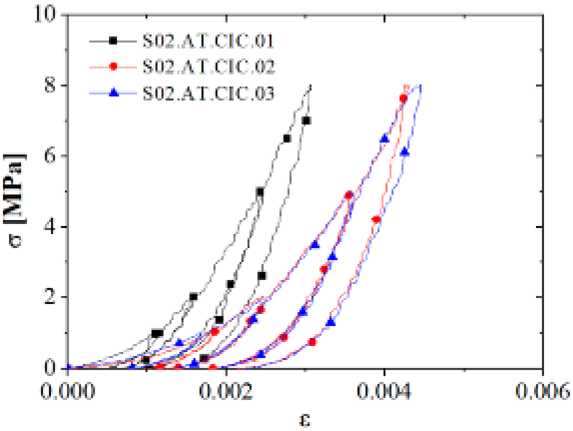


**Figure 15 – Test series S02.AT.CIC – stress-strain curves.**

The evolution of the residual strain with the applied load is shown in Figure 16a. The crushing of brick's surfaces happened during the loading cycles of the tests and resulted in the increase of the contact area between the bricks. Consequently, it increased the Young's modulus of the wall. For example, the evolution of the tangent Young´s modulus of the specimen S02.AT.CIC.02 with the load cycles is presented in Figure 16b. The values shown in the graph are the maximum tangent Young's modulus measured for each cycle. The values measured during the loading and unloading stages are presented in blue and red, respectively. The numbers in the subscript stand for the load cycle and the letters L and U stand for loading and unloading stages, respectively. The Young's modulus of the wall (13.0 GPa in the last unloading cycle) was significantly lower than the one of the material (28.8 GPa), indicating stress concentrations in the specimen.

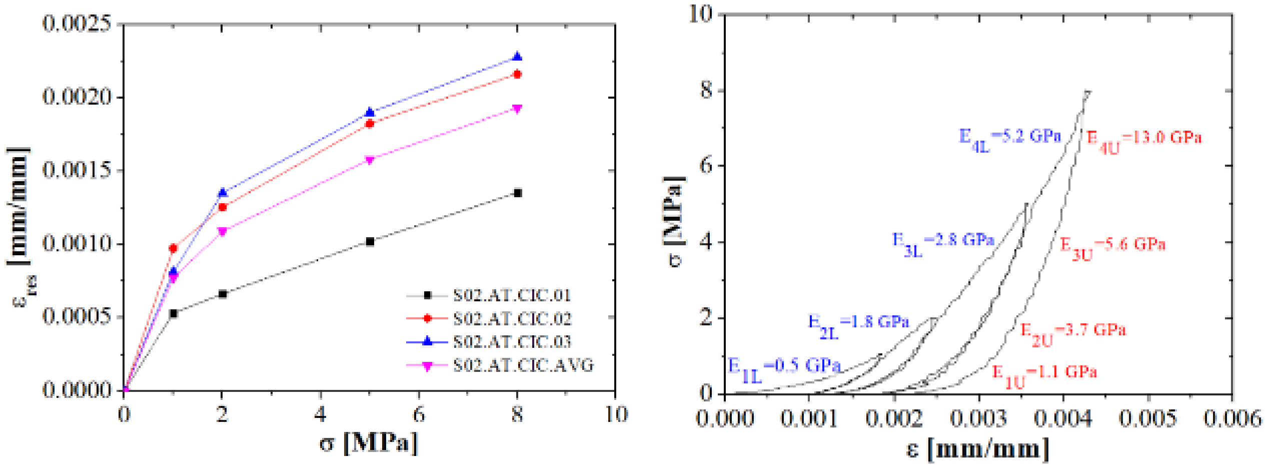


a) b)

**Figure 16 – Test series S02.AT.CIC – Joint crushing process:**
**a) Evolution of residual strain with load level and b) Evolution of wall's Young's modulus after joint crushing.**

The bricks' shape imperfections are the main contributor for the unevenness stress distribution obtained along the wall (Ngapeya et al, 2018), as observed in the test series S01.AT.LBC. Figure 17 presents the in-plane displacement fields measured by DIC for specimen S02.AT.CIC.02. The flow of in-plane forces can be easily identified: the regions with higher displacements indicate the presence of two pressure bulbs in the wall. It is also observed that the residual displacements are higher in the areas of the pressure bulbs.

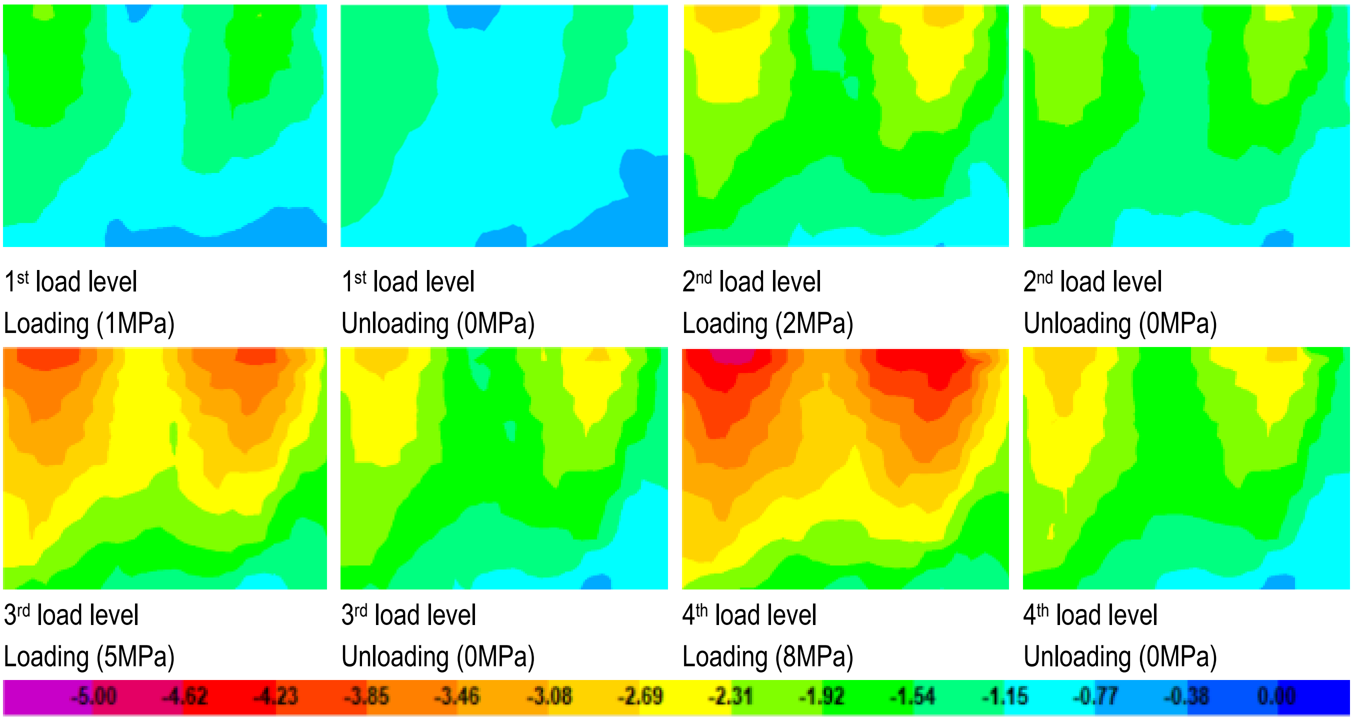


Figure 17 – In plane vertical displacement fields measured by DIC for test series S02.AT.CIC.02 [in mm].

The bricks' shape imperfections, in dry-stacked masonry, led to stress concentrations in the wall. Consequently, cracks were observed for even relatively low load levels that were applied (8 MPa), as shown in Figure 18. The cracks were mostly located in the middle of the bricks (cross joints) and were caused by the non-uniform loading and support conditions of the bricks.

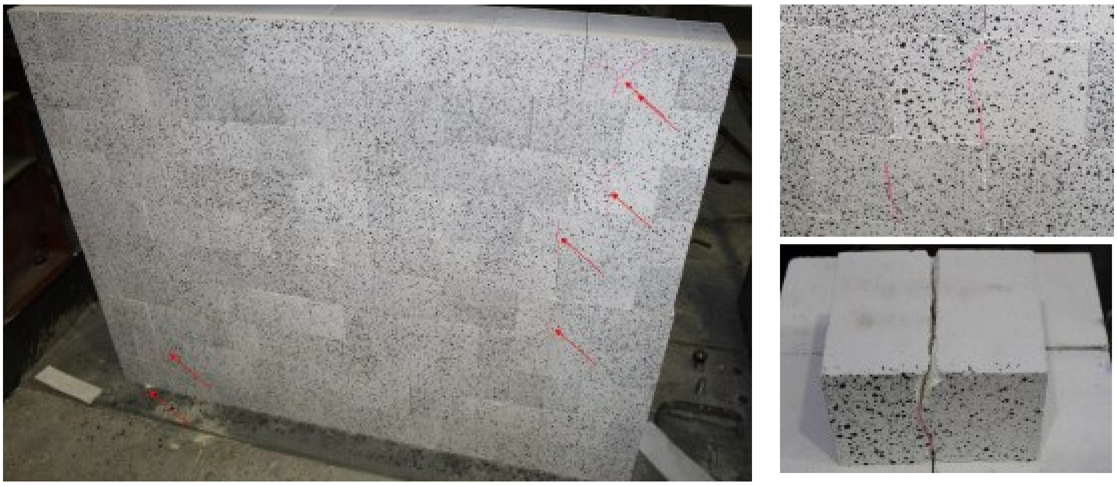

Figure 18 – Test series S02.AT.CIC: Crack patterns observed at the end of the test.

### 2.3.3 Test series S03.HT.LL8

The temperatures measured by the thermocouples within the specimens of test series S03.HT.LL8 are presented in Figure 19. The standard fire curve ISO 834-1 (1999) and the temperature measured inside the furnace are presented in red. The purple dashed line indicates the beginning of the heating process. In this figure, "HF" and "CF" stand for the thermocouples of the hot and cold face, respectively. The position of the thermocouples in the wall can be seen in Figure 19d.

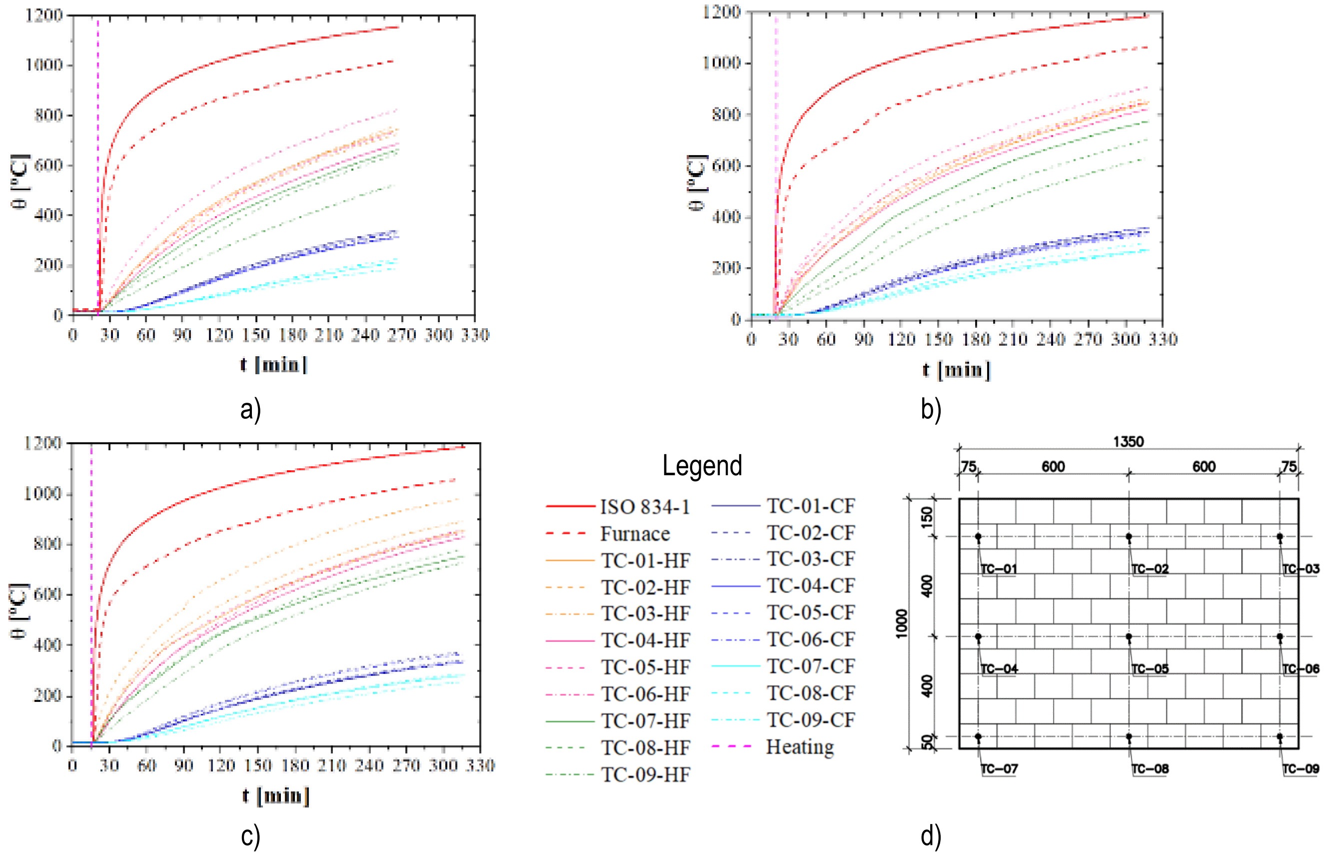


**Figure 19 – Test series S03.HT.LL8 – Temperature evolution:**
**a) S03.HT.LL8.01, b) S03.HT.LL8.02, c) S03.HT.LL8.03 and d) Legend and thermocouple's location.**

Due to the high thermal capacitance of the specimen, the furnace was not able to follow the programmed curve. The temperatures in the hot face started to increase rapidly when the thermal load was applied. Due to the relatively low thermal conductivity of the refractory materials, the temperatures on the cold face took some time to start increasing. The temperatures in the first course of the bricks (bottom of the wall), measured by TC-07, TC-08 and TC-09, were lower than the average temperatures of the wall. This was caused in part by the furnace's internal arrangement of the resistances, making this area less exposed to radiation (Figure 3), due to heat losses through the reaction slab (Figure 3b), and due to the air convective currents inside the furnace. In general, a relatively homogeneous temperature distribution was found in the wall within a range of ±15 %. The difference between the average and the maximum and minimum temperatures measured were also slightly influenced by the depth at which the thermocouples were embedded and by heat losses at the edges of the specimens. The accurate measurement of the temperature fields within the specimen along the test is important as it has a significant impact on the thermomechanical behaviour of the specimens. The temperature gradient through the thickness of the wall led to thermal bowing on the specimen. Consequently, significant out-of-plane displacements were observed during the heating stage of the tests.

The in-plane displacements measured by the LVDTs and the average of these values are presented in Figure 20. The out-of-plane displacements are given in Figure 21. Small out-of-plane displacements are observed during the load stage. The out-of-plane displacements increase during the heating stage, due to the thermal bowing of the wall. The average of the measured in-plane displacements is presented in Figure 22a. At the beginning of the test, from 0 to 20 minutes, the pre-compression stress of 8 MPa was applied, and negative displacements (towards the furnace) were observed as a result of the joint closure and bricks deformation. The maximum displacements after load application were -3.12 mm ($\varepsilon$ = - 0.0031), -3.76 mm ($\varepsilon$ = - 0.0038) and -3.49 mm ($\varepsilon$ = - 0.0035) for specimens S03.HT.LL8.01, S03.HT.LL8.02 and S03.HT.LL8.03, respectively.

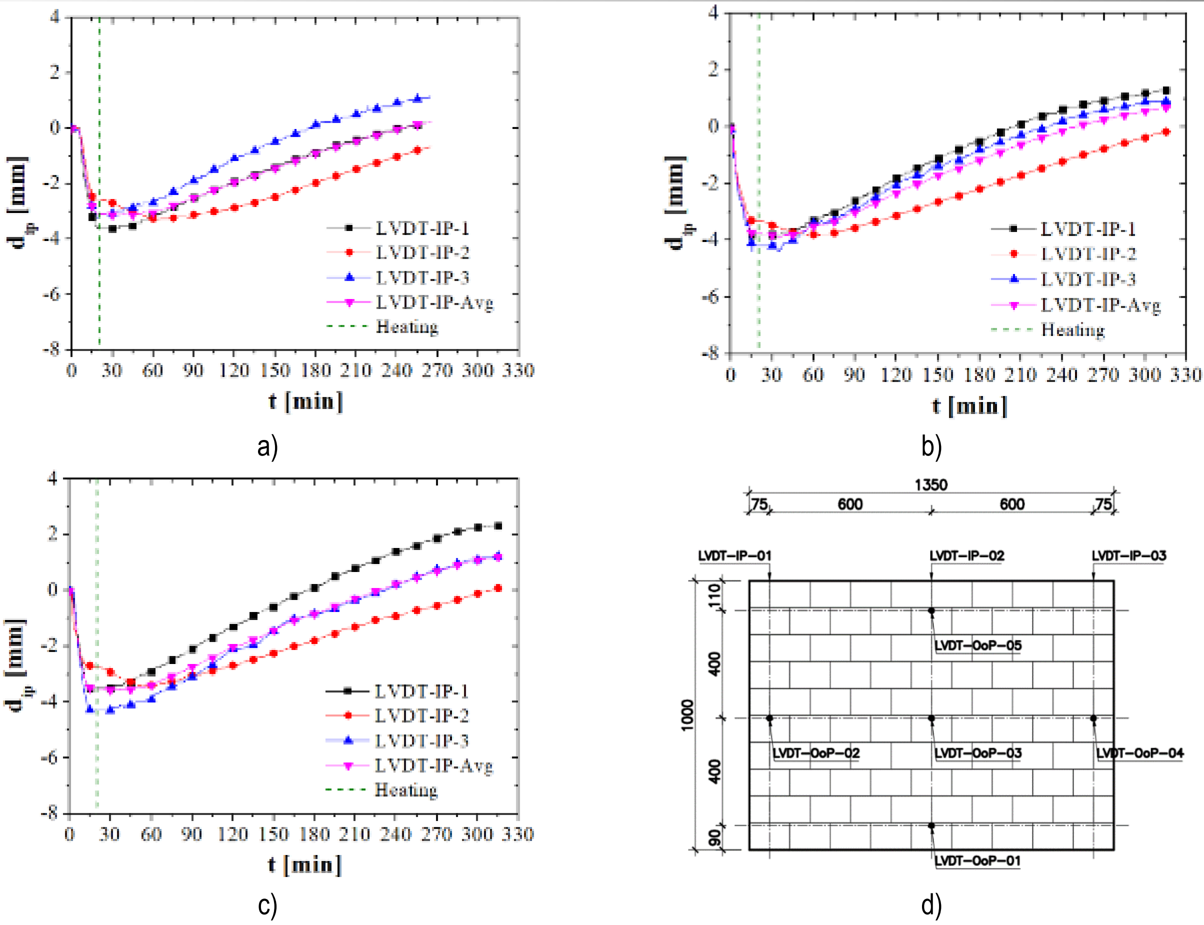


**Figure 20 – Test series S03.HT.LL8 – In-plane displacements:**
**a) S03.HT.LL8.01, b) S03.HT.LL8.02, c) S03.HT.LL8.03 and d) LVDT locations.**

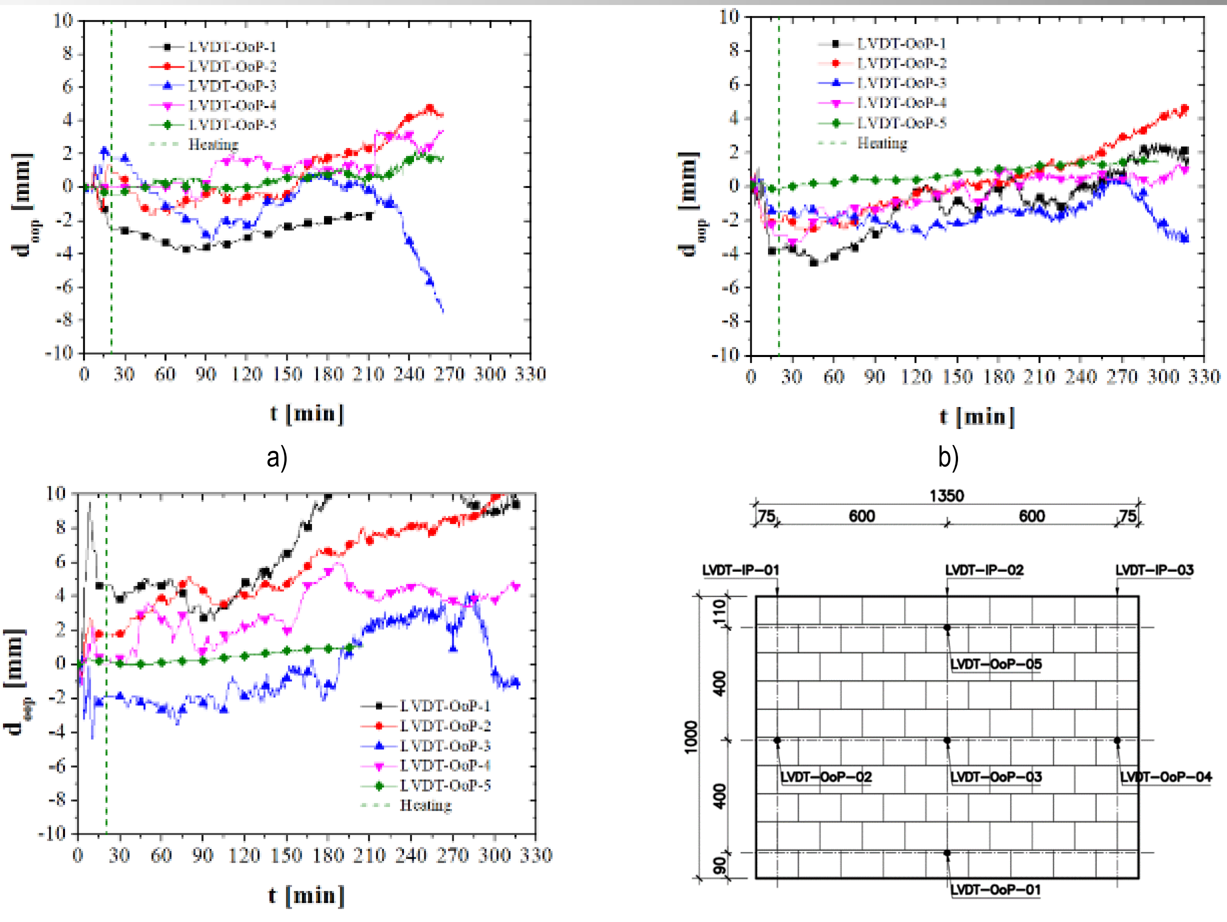


a) b) c) d)

**Figure 21 – Test series S03.HT.LL8 – Out-of-plane displacements:**
**a) S03.HT.LL8.01, b) S03.HT.LL8.02, c) S03.HT.LL8.03 and d) LVDT locations.**

At 20 minutes after the beginning of the test, the furnace was turned on and the temperatures at the hot face started to increase. After 45 to 60 minutes from the beginning of the test, the effects of the thermal elongation started to increase and the wall presented a positive strain rate. The thermal elongation surpassed the displacements caused by the mechanical loading after 244 min, 249 min and 252 min of the beginning of the test, for specimens S03.HT.LL8.01, S03.HT.LL8.02 and S03.HT.LL8.03, respectively. Test S03.HT.LL8.01 was stopped after 265 minutes, with a positive displacement of 0.24 mm ($\varepsilon$ = 0.0002). Tests S03.HT.LL8.02 and S03.HT.LL8.03 were stopped after 300 minutes, with maximum displacements of 0.61 mm ($\varepsilon$ = 0.0006) and 0.80 mm ($\varepsilon$ = 0.0008), respectively. The force measured by the load cell positioned at the top of the steel loading beam is given in Figure 22b. The load level remained constant during the tests, the load of 1512 kN resulted in the stress level of 8 MPa.

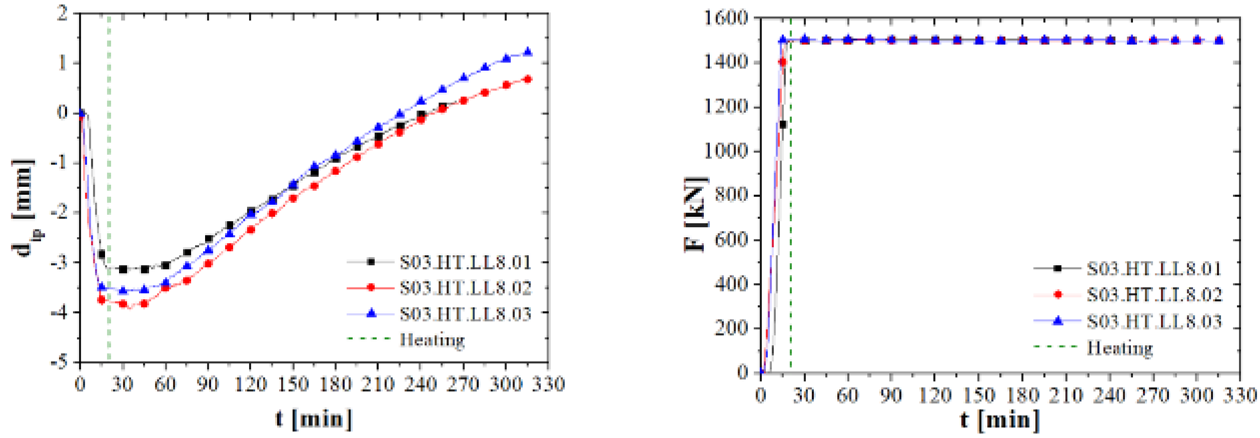


a) b)

**Figure 22 – Test series S03.HT.LL8: a) Average in-plane displacements and b) Average forces**

Despite the relatively low load level in the wall, some cracks were observed in the specimen upon completion of the test. Figure 23 shows the cracks observed in the interface between the load application beam and the wall's top surface. These cracks were caused by a high stress state reached in this region, as the mechanical load restrains the elongation of the specimen.

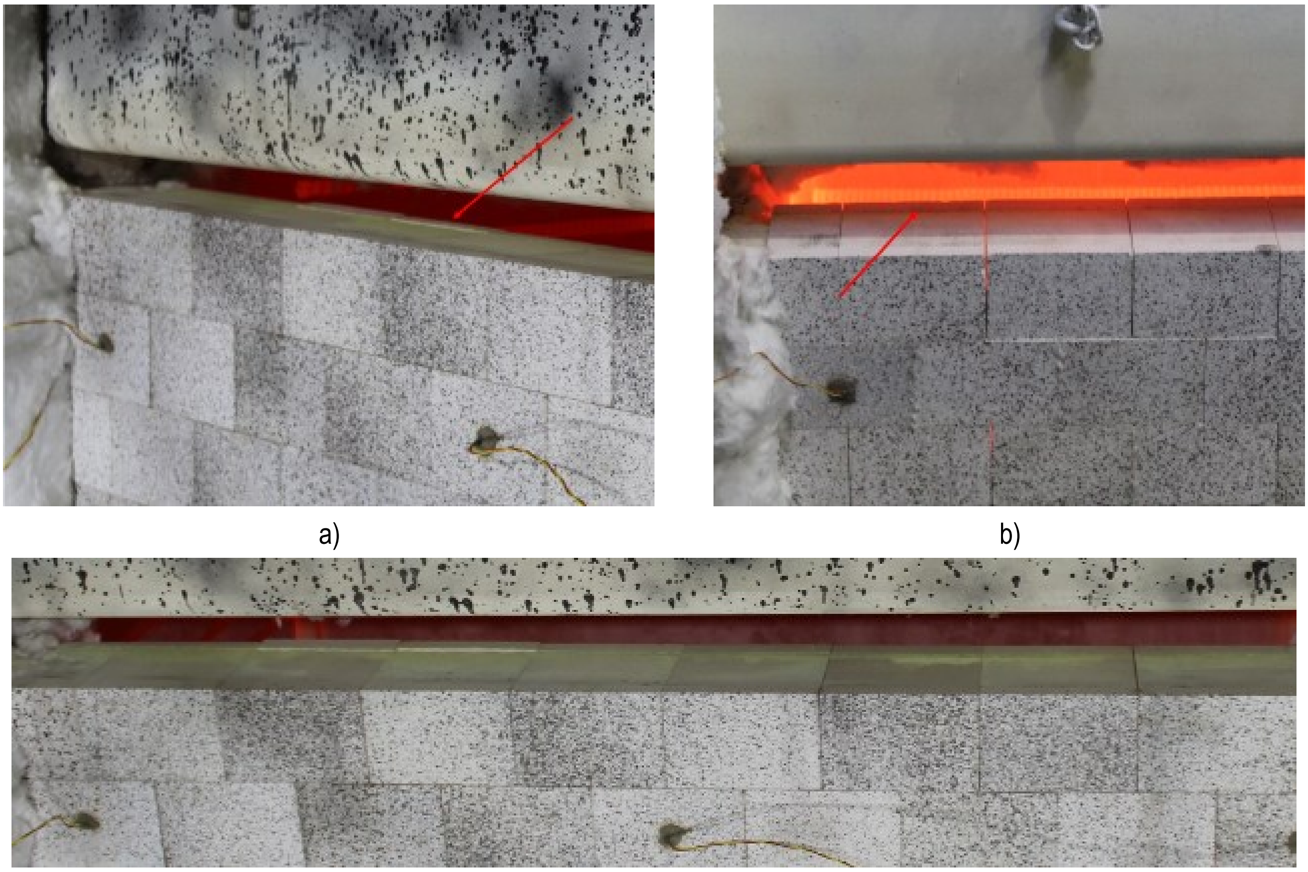

a) b)

c)

**Figure 23 – Test series S03 – Damage in the wall upon completion of the test - Cracks in the interface between load application beam and wall: a) S03.HT.LL8.01, b) S03.HT.LL8.02 and c) S03.HT.LL8.01.**

Figure 24 shows the vertical cracks observed in the middle of the bricks (indicated by the red arrows), caused by the unevenness stress distribution, as discussed in Series S02.AT.CIC. The cracks of the bricks, resulted in rigid body motion of the adjacent bricks, leading to head joint opening (indicated by the green arrows).

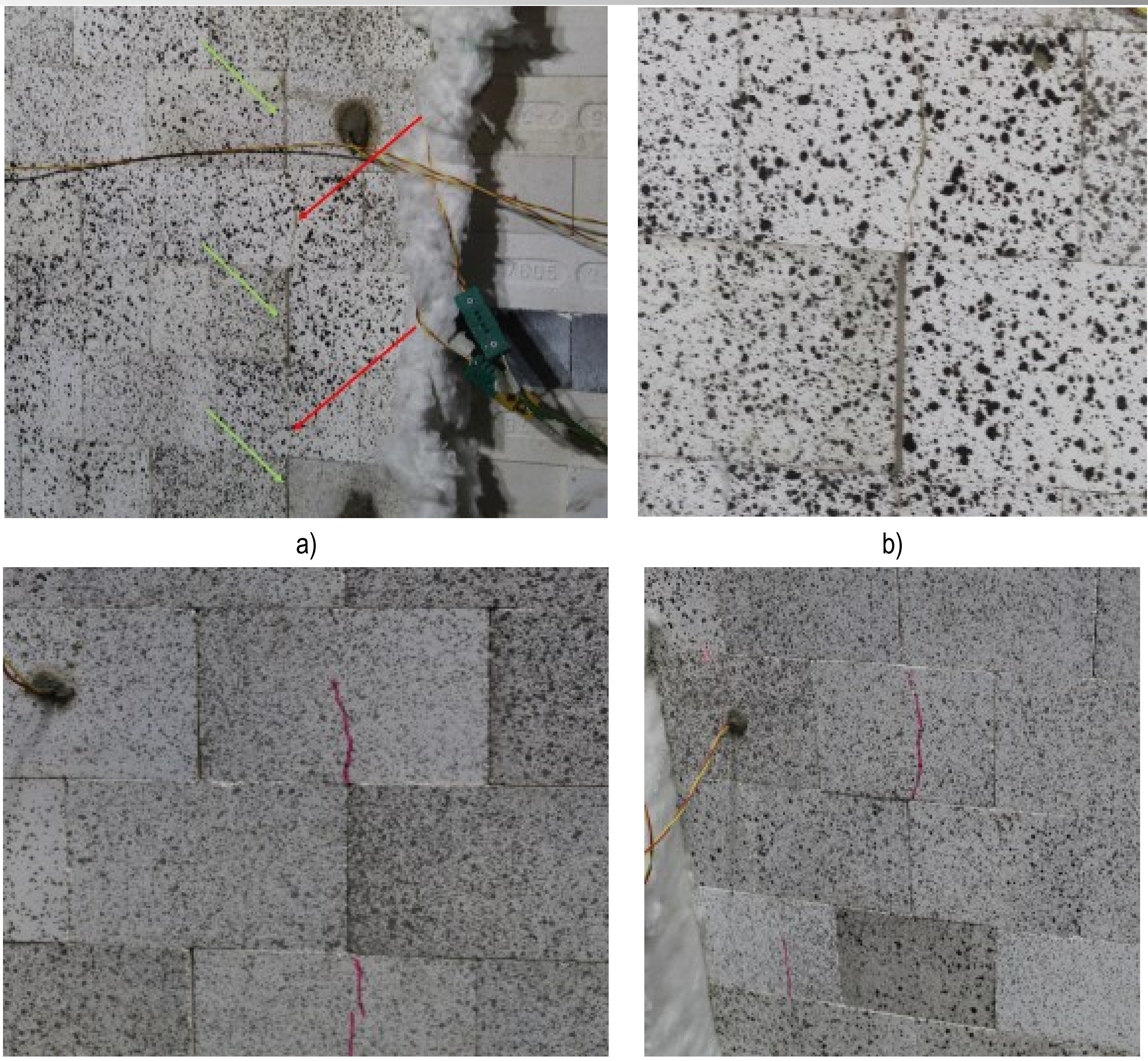

a) b)

c) d)

**Figure 24 – Test series S03 – Damage in the wall upon completion of the test:**
**a) Vertical cracks in bricks and joint openings, b) Crack details, c) Cracks details and d) Cracks details.**

### 2.3.4 Test series S04.HT.RTE

The temperatures measured by the thermocouples within the specimens of test series S03.HT.LL8 are presented in Figure 25. The standard fire curve ISO 834-1 (1999) and the temperature measured inside the furnace are presented in red. The purple dashed line indicates the beginning of the heating process. In this figure “HF” and “CF” stands for the thermocouples of the hot and cold face, respectively. The position of the thermocouples in the wall is highlighted in Figure 25d.

As in the previous test series, the high thermal capacitance of the specimen did not allow the furnace to follow the programmed curve. The temperatures in the hot face started to increase rapidly at the beginning of the heating phase. Due to the relatively low thermal conductivity of the refractory materials, the temperatures on the cold face took some time to start increasing. Once again, the temperatures in the first layer of the bricks (bottom of the wall) were lower than the average temperatures of the wall. In some cases (*e.g.* TC-02-HF and TC-05-HF of specimen S04.HT.RTE.02), the detachment of the thermocouple was observed. In these cases, the thermocouple and the grout layer used to fix it disconnected from the hole made in the brick and fell out. Consequently, the measurements of these thermocouples were removed from the graphs after the moment of the detachment.

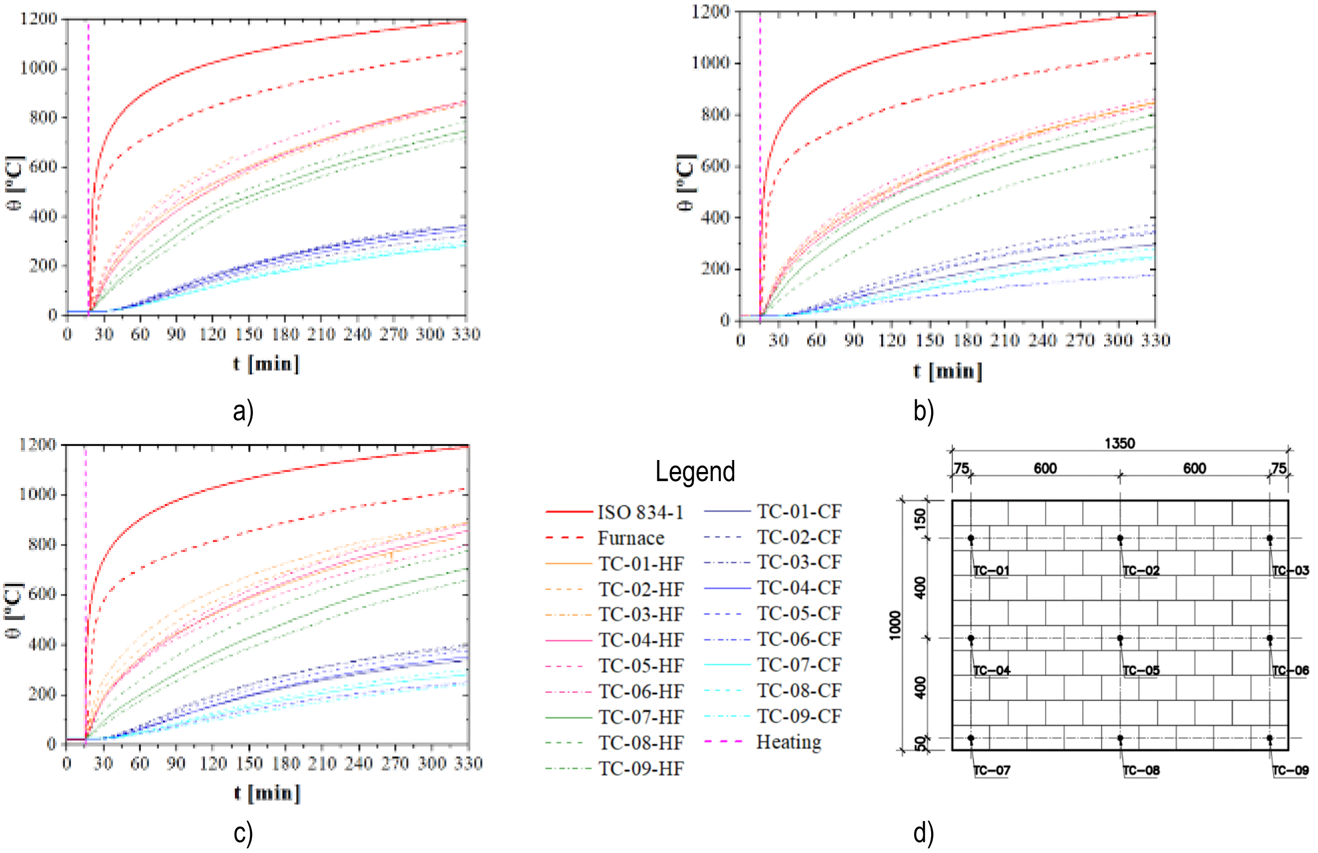


**Figure 25 – Test series S04.HT.RTE – Temperature evolution:**
**a) S04.HT.RTE.01, b) S04.HT.RTE.02, c) S04.HT.RTE.03 and d) Legend and thermocouple location.**

The in-plane displacements measured by the LVDTs and the average of these values are presented in Figure 26. The LVDT-IP-2 of test S04.HT.RTE.02 malfunctioned, therefore, for this test, only the LVDT-IP-1 and LVDT-IP-3 were used to calculate the average displacement. The equipment was replaced for the following tests.

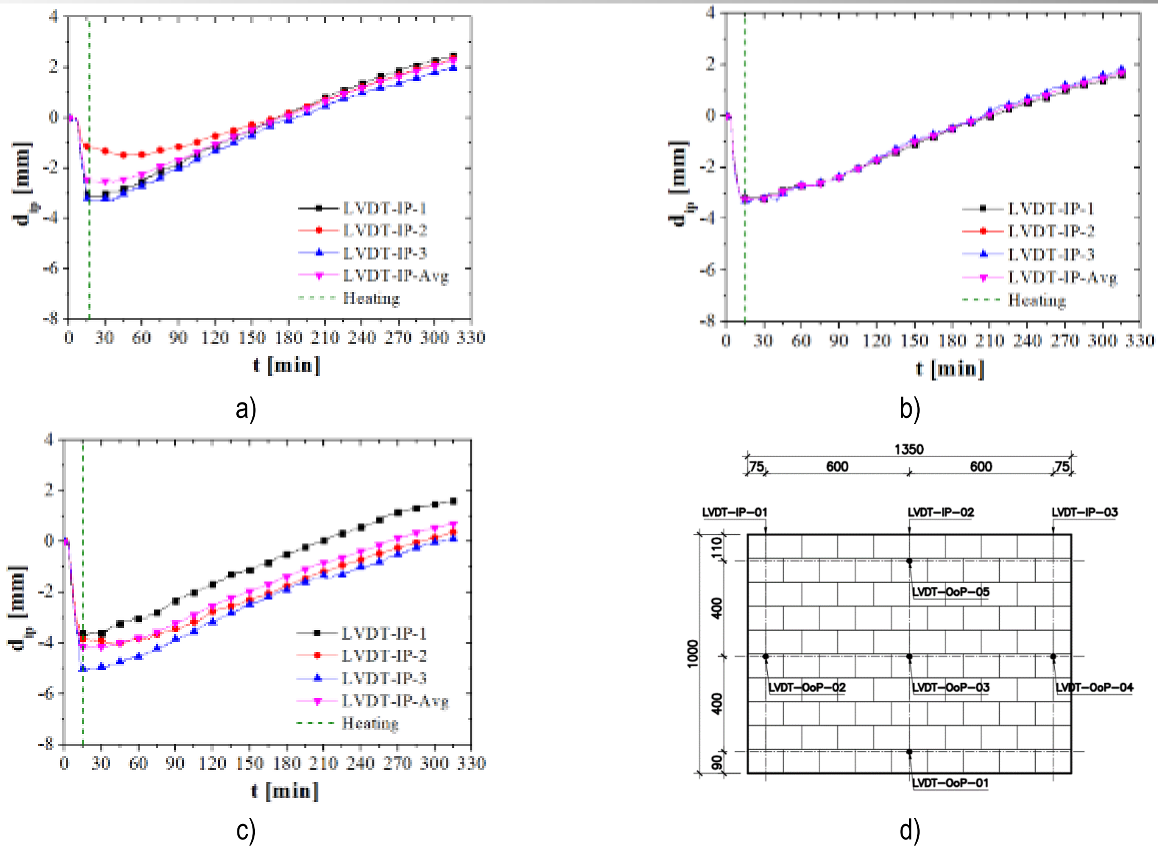


**Figure 26 – Test series S04.HT.RTE – In-plane displacements:**
**a) S04.HT.RTE.01, b) S04.HT.RTE.02, c) S04.HT.RTE.03 and d) LVDT positions.**

The out-of-plane displacements are given in Figure 27. Relatively small out-of-plane displacements are obtained during the load application at ambient temperature. When the heating started, it was possible to identify a significant increasing in the out-of-plane displacements, caused by the thermal bowing due to the thermal gradient through the thickness of the wall.

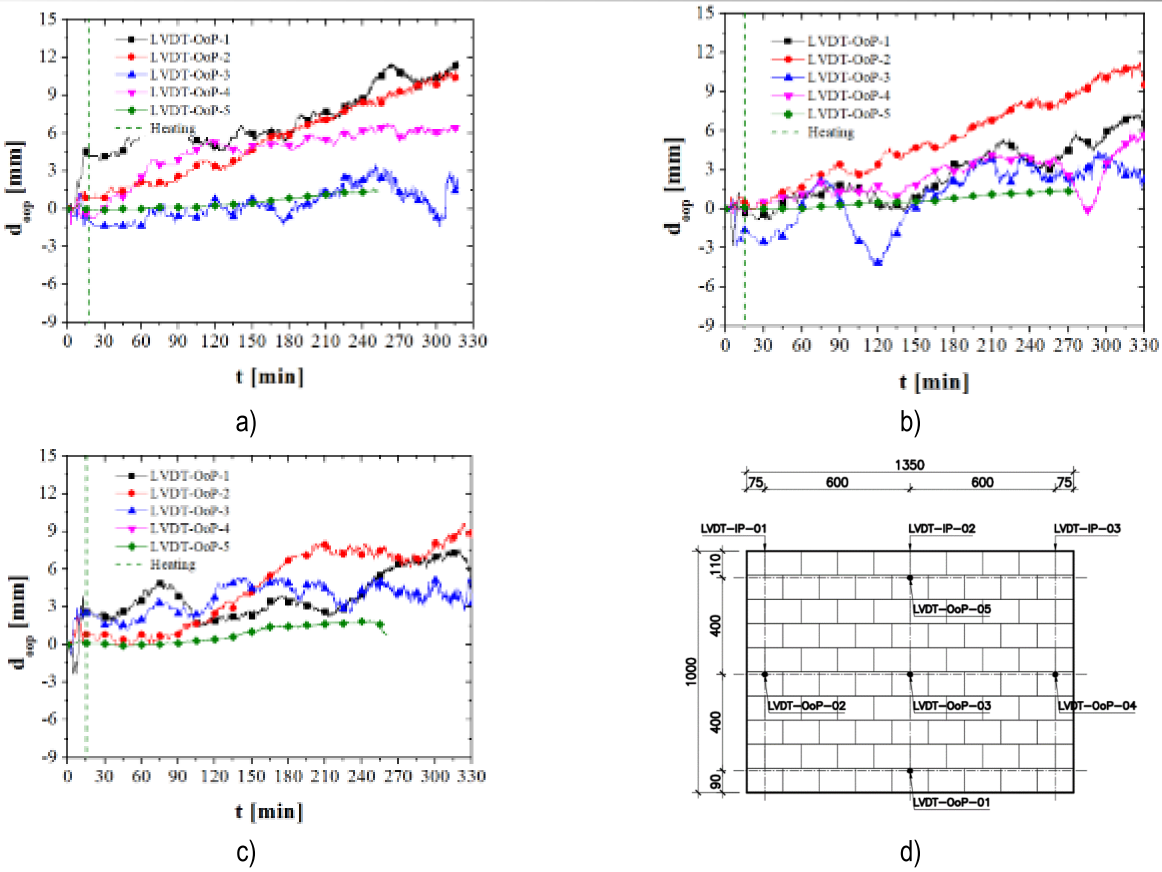


**Figure 27 – Test series S04.HT.RTE – Out-of-plane displacements:**
**a) S04.HT.RTE.01, b) S04.HT.RTE.02, c) S04.HT.RTE.03 and d) LVDT positions.**

The average in-plane displacements are presented in Figure 28a. At the beginning of the test, from 0 to 20 minutes, the mechanical load of 5 MPa (945 kN) was applied, and a negative displacement was observed, as a result of the joint closure and brick´s behaviour. The maximum displacements after load application were -2.53 mm ($\varepsilon$ = -0.0025), -3.22 mm ($\varepsilon$ = -0.0032) and -4.15 mm ($\varepsilon$ = -0.0042) for test specimens S04.HT.RTE.01, S04.HT.RTE.02 and S04.HT.RTE.03, respectively. After 20 minutes, the furnace was turned on and the heating started, consequently the temperature increased, and the effects of thermal elongation led to a positive strain rate. The thermal elongation surpassed the displacements caused by the mechanical load after 173 min, 206 min and 261, for the test specimens S04.HT.RTE.01, S04.HT.RTE.02 and S04.HT.RTE.03, respectively. All tests were stopped after 320 minutes. At this moment, the maximum displacements observed were 2.31 mm ($\varepsilon$ = 0.0023), 1.74 mm ($\varepsilon$ = 0.0017) and 0.75 mm ($\varepsilon$ = 0.0008) for test specimens S04.HT.RTE.01, S04.HT.RTE.02 and S04.HT.RTE.03, respectively.

Figure 28b presents the evolution of the forces developed in the specimen. From 0 to 20 minutes, a pre-load of 5 MPa was applied. Then, the position of the hydraulic jack was blocked, and the thermal load was applied. As expected, the thermal elongation led to an increasing compressive force in the wall. By the end of the test, the measured stresses for test series S04.HT.RTE.01, S04.HT.RTE.02 and S04.HT.RTE.03 were 6.47 MPa (1222kN), 6.22 MPa (1185 kN) and 6.08 MPa (1149 kN), respectively.

During the heating stage of series S04.HT.RTE the hydraulic jack was set to be blocked at its current position, in fact the LVDT used to feed the servo-controller unit of the jack did not provide measurements during the heating stage. However, the reaction frame (composed by two HEB500 columns and two HEB600 beams) worked as a spring with axial stiffness $K_B$ (see Figure 28c). The increasing of the vertical load in the wall caused by the restrained thermal elongation led to displacements in the reaction frame and consequently to strains in the wall.

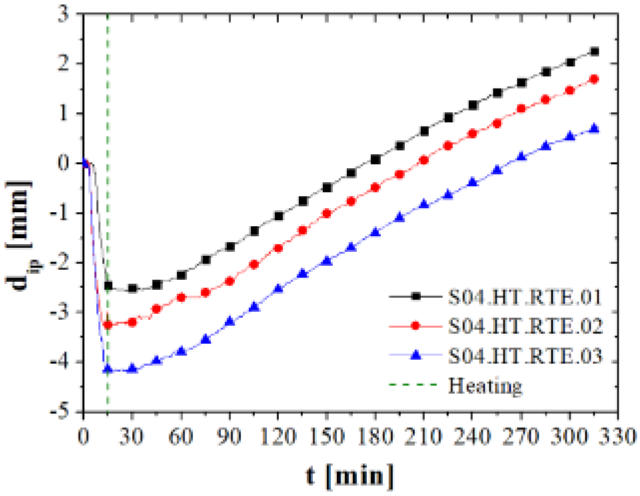


a)

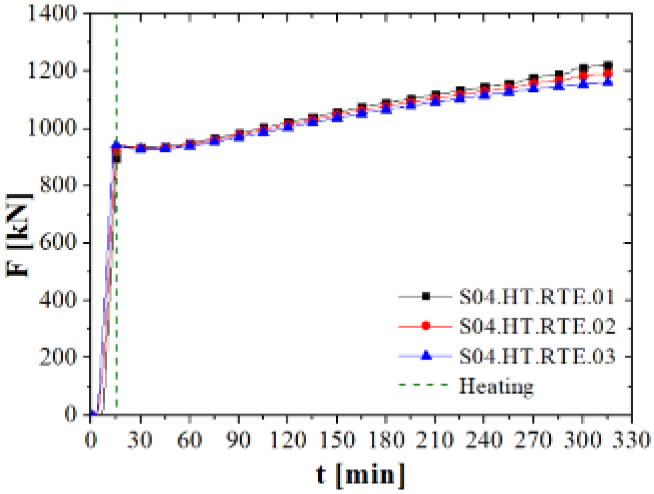


b)

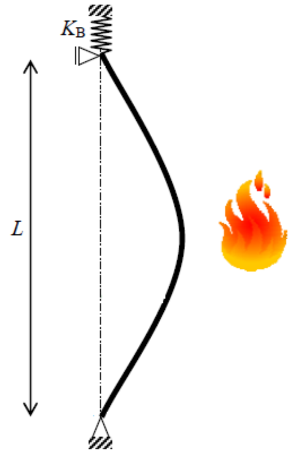


c)

**Figure 28 – Test series S04.HT.RTE: a) Average in-plane displacements, b) Forces and c) Structural schematics.**

Despite the relatively low load level in the wall, again some cracks were observed between the load application beam and the wall's top surface (similar to Figure 23). Figure 29 presents vertical cracks observed in the middle of the bricks (indicated by the red arrows), caused by an unevenness stress distribution, as discussed in test series S02.AT.CIC and S03.HT.LL8. Rigid body motions caused by the cracks in the bricks were also observed, leading to head joint opening (indicated by the green arrows). Figure 30 presents the cracks observed in specimen S04.HT.RTE.01 after the end of the test. The observed cracks were located at the cross-joints and were caused by the brick shape imperfections. These imperfections resulted in a non-homogeneous stress distribution in the wall. The stress concentrations were also responsible for the crushing observed in Figure 30b.



European Commission
Horizon 2020
European Union funding
for Research & Innovation

Figure 29 – Test series S04.HT.RTE – Failures in the wall: Vertical cracks in bricks and joints openings (S04.HT.RTE.02).

a)

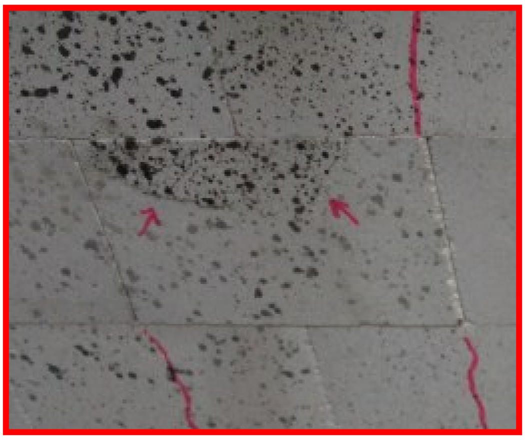

b)

c)

Figure 30 – Test series S04.HT.RTE – a) Overview of vertical cracks in specimen S04.HT.RTE.01, b) Brick crushing due to stress concentrations at the cross joints and c) Brick cracks and joint opening.

### 2.3.5 Test series S05.HT.LL10

The measured temperatures are presented in Figure 31. The positions of the thermocouples are also shown. The temperatures in specimen S05.HT.LL10.02 were slightly higher than in the specimen S05.HT.LL10.01 since an insulation was placed in the cold face of the wall. The objective was to heat the specimen as much as possible.

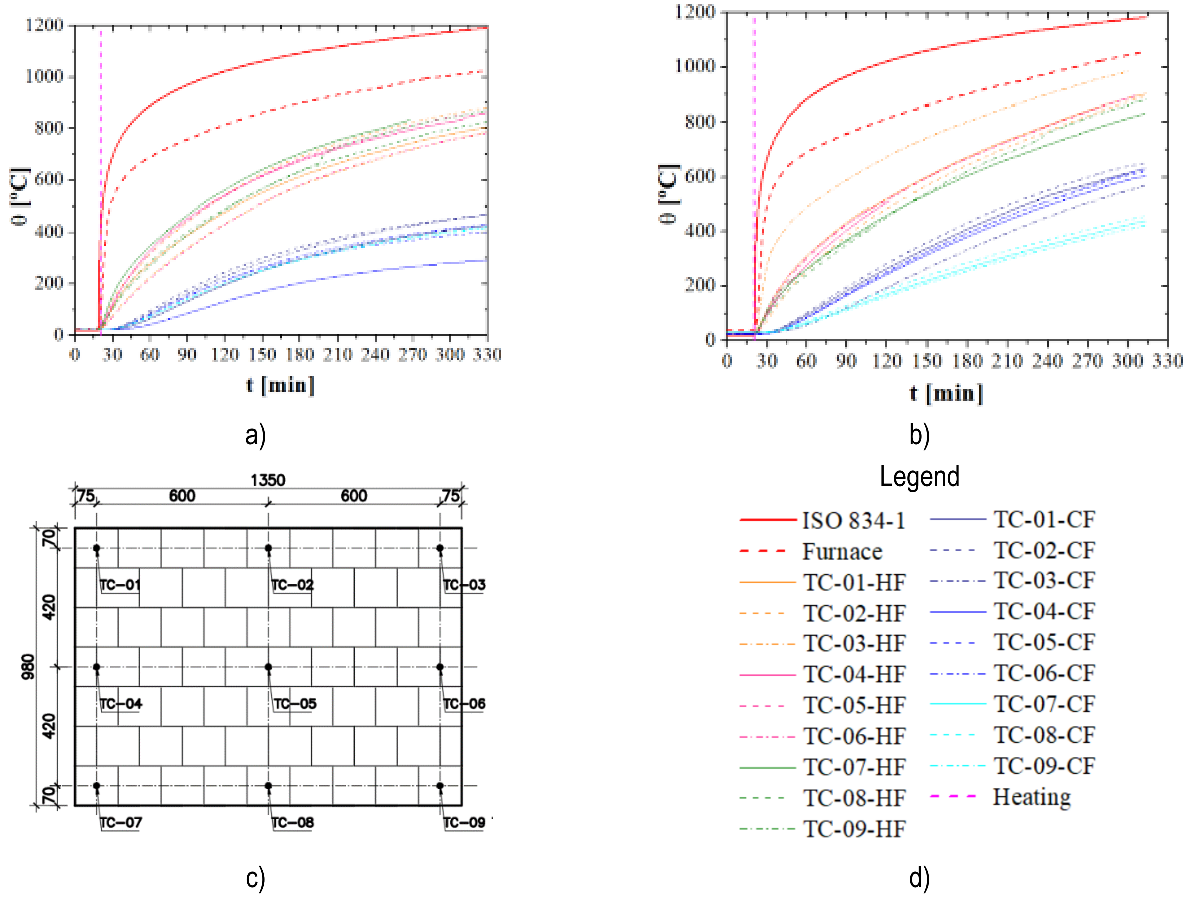


**Figure 31 – Test series S05.HT.LL10 – Temperature evolution:**
**a) S05.HT.LL10.01, b) S05.HT.LL10.02, c) Thermocouple location and d) Legend.**

The in-plane displacements measured by the LVDTs and the average of these values are presented in Figure 32. The average displacement of both tests after load application were similar, however in the case of test S05.HT.LL10.02 the failure of the specimen was observed, as shown in Figure 32b. The specimen S05.HT.LL10.01 did not reach failure, however, it was possible to observe a reduction of stiffness after 300 minutes of testing (Figure 32a). The out-of-plane displacements are given in Figure 33. The smaller thickness of the wall (100 mm), when compared to the specimens of test series S02.AT.CIC, S03.HT.LL8 and S04.HT.RTE (140 mm), resulted in a smaller inertia of the wall and consequently higher out-of-plane displacement during the loading stage. During the heating stage, the out-of-plane displacements increased significantly.

The average of the in-plane displacements is presented in Figure 34a. At the beginning of the test, from 0 to 20 minutes, the load was applied, and a negative displacement was again observed. The displacements after load application were - 5.25 mm ($\varepsilon$ = - 0.0053) and - 4.86 ($\varepsilon$ = - 0.0049) mm for specimens S05.HT.LL10.01 and S05.HT.LL10.02, respectively. When the furnace was turned on (at 20 minutes) the temperatures at the hot face started to increase, consequently the thermal elongation started, and the wall presented a positive strain rate. The thermal elongation surpassed the displacements caused by the mechanical load after 296 min and 214 min for specimens S05.HT.LL10.01 and S05.HT.LL10.02, respectively.

Figure 34b presents the measured load during the test. A small pressure drop was observed in the hydraulic jack for specimen S05.HT.LL10.01, most likely caused by cracks in the bricks. However, the servo-controller unit corrected it immediately, increasing the pressure in the hydraulic jack and returning the applied force to the target. The brittle rupture of the specimen S05.HT.LL10.02 resulted in a quick reduction of the force measured by the load cell positioned at the top of the steel loading beam.

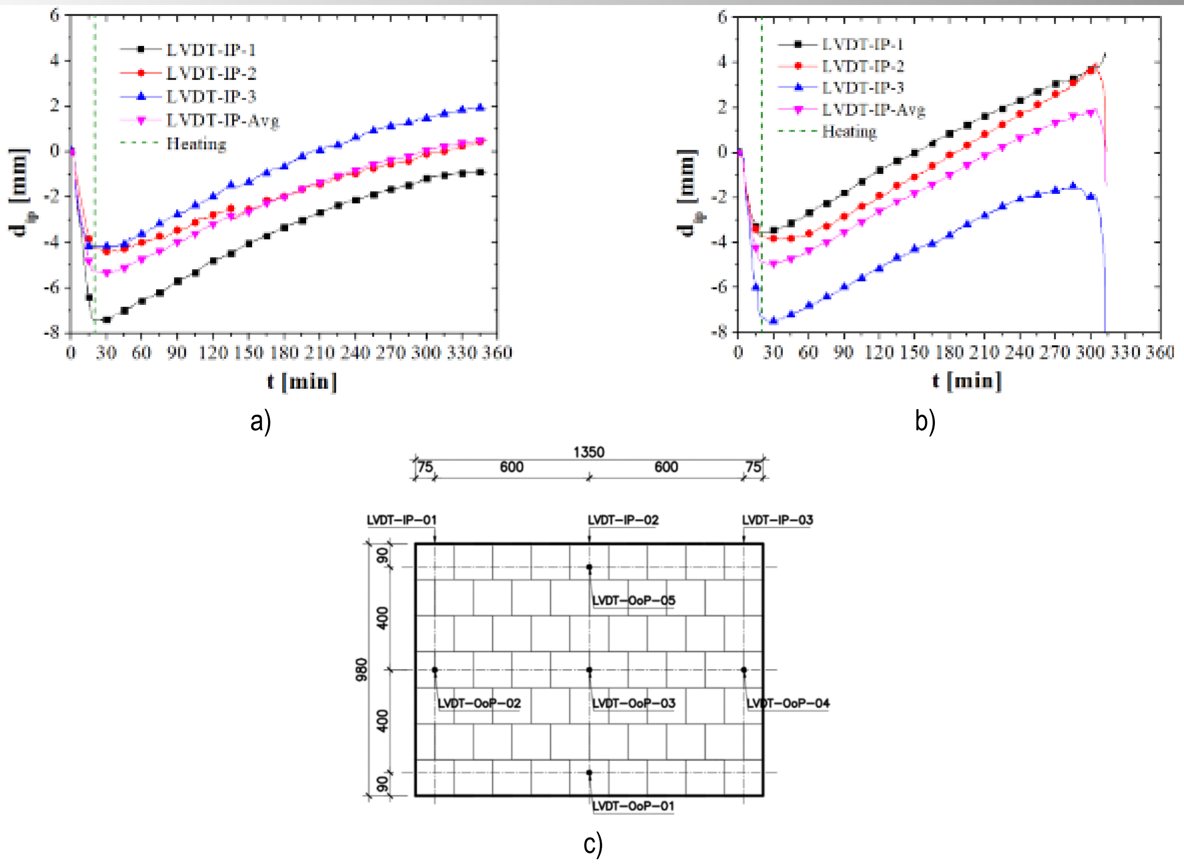


Figure 32 – Test series S05.HT.LL10 – In-plane displacements: a) S05.HT.LL10.01, b) S05.HT.LL10.02 and c) LVDT locations.

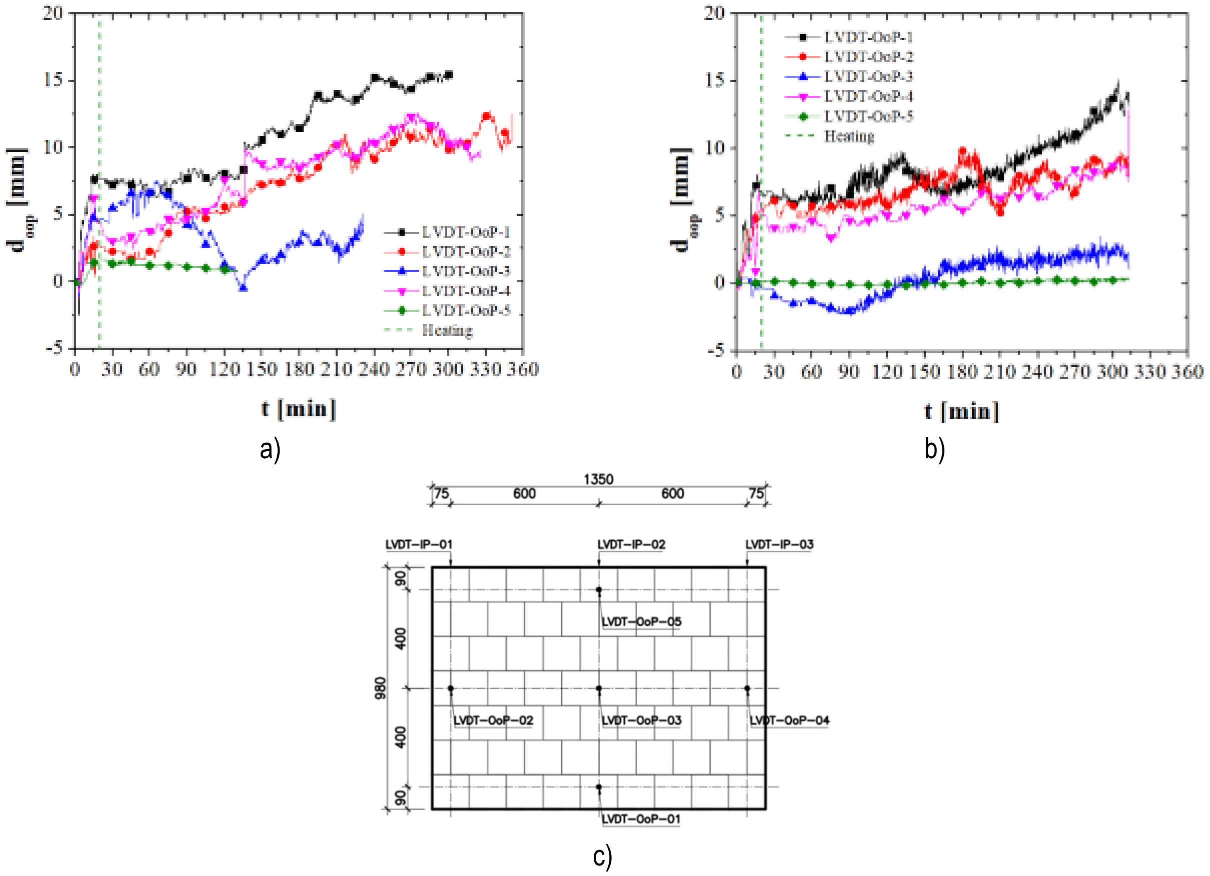


Figure 33 – Test series S05.HT.LL10 – Out-of-plane displacements: a) S05.HT.LL10.01, b) S05.HT.LL10.02 and c) LVDT locations.

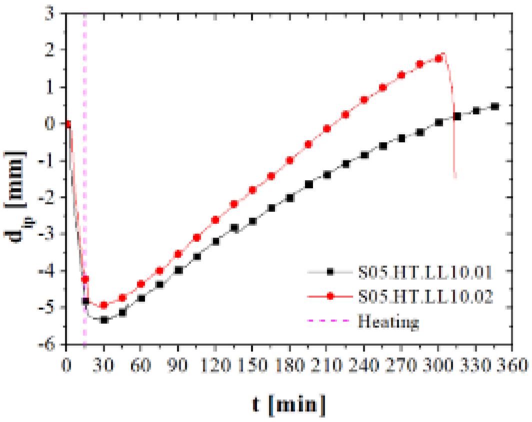


a)

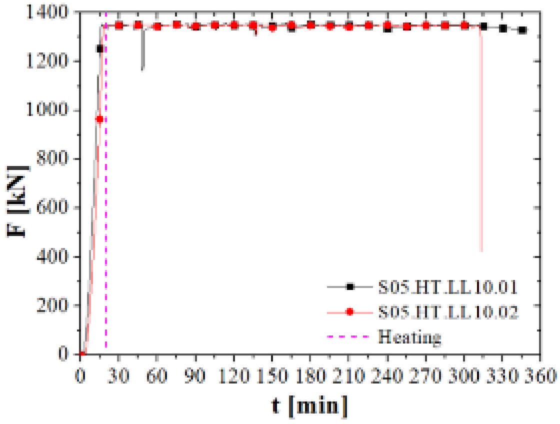


b)

**Figure 34 – Test series S05.HT.LL10: a) Average in-plane displacements and b) Forces.**

The test for specimen S05.HT.LL10.01 was stopped after 360 minutes. At this moment, a positive displacement of 0.49 mm ($\varepsilon$ = 0.0005) was registered. The failure of this specimen was not observed in the test. Nevertheless, some cracks and crushing were observed in the specimen, as shown in Figure 35a. The temperatures in specimen S05.HT.LL10.02 increased slightly faster in comparison with the other specimen due to the thermal insulation installed in front of the wall. As shown in Figure 35a, the strain rate of S05.HT.LL10.02 was higher as the thermal elongation is more significant. The thermal gradient in the wall led to significant thermal bowing, defined as an out-of-plane displacement of the specimen. The thermal bowing caused an eccentricity in the vertical load and led to sudden failure of the wall, as seen in Figure 36.

a)

b)

c)

**Figure 35 – Test series S05.HT.LL10 – Vertical cracks in bricks and joint openings in specimen S05.HT.LL10.01: a) Crack locations, b) Details of the top left side and c) Details of the bottom left side.**

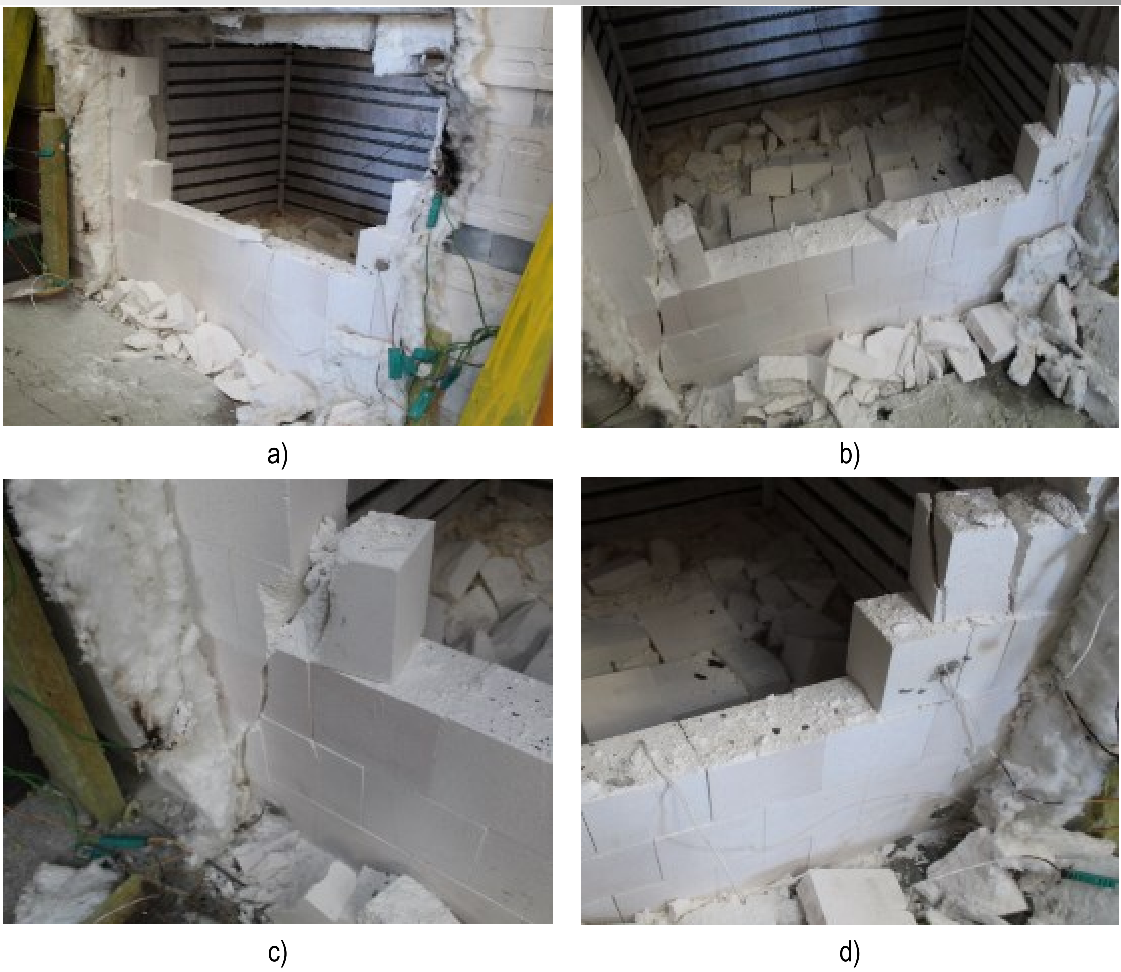

Figure 36 – Test series S05.HT.LL10 – Failure of specimen S05.HT.LL10.02: a) Overview, b) Top view, c) Details of bricks' failure from the left side of the wall and d) Details of bricks' failure from the right side of the wall.

# 3 Biaxial compression tests

The previous section presented experimental characterization of refractory masonry under uniaxial compression at ambient and elevated temperatures (up to 1100 ºC). However, refractory linings are usually subjected to higher temperatures (up to 1650 ºC) and complex stress states. Currently available literature only presents results of biaxial compression tests (Prietl, 2006) up to 1200 ºC, which is still far from service temperature.

The experimental campaign presented in this section is an extension of in the research carried out by Prietl (2006) on refractory wallets under biaxial compression. Several improvements were made to the experimental setup: *i*) the heating elements were replaced to reach temperatures up to 1500 ºC; *ii*) the insulation of the device was redesigned to reduce the heat losses; *iii*) DIC was used in the tests at room temperature to map the strain fields in the specimens.

The objective of this work was to study the behaviour of dry-stacked refractory wallets at ambient and elevated temperatures (up to 1500 ºC) under uniaxial and biaxial compression loads. Six different test series were studied. At ambient temperature, series S06.AT.LBJ and S07.AT.LHJ aimed at assessing the mechanical behaviour of masonry wallets subjected to Loading in the directions of the Bed and Head Joints, respectively. Series S08.AT.LBI aimed at assessing the behaviour of the wallet at ambient temperature under BIaxial load. At high temperatures, series S09.HT.CBJ and S10.HT.CBI aimed to assess the Creep Behaviour of the specimen in the direction of the bed Joints and under BIaxial loads, respectively. Series S11.HT.RBI aimed to evaluate the behaviour of the specimen under BIaxial Relaxation. The experimental results are being used for validation of the numerical models within WP3. The detailed description of each test series can be seen in the list below and Table 2:

- Series S06.AT.LBJ: carried out at ambient temperature (AT) with the objective of evaluating the mechanical behaviour of the wallet loaded at the bed joints (LBJ).
- Series S07.AT.LBJ: carried out at ambient temperature (AT) aiming to assess the behaviour of the dry stacked masonry loaded at the head joints (LHJ).

- Series S08.AT.LBI: carried out at ambient temperature (AT) with the objective of evaluating the mechanical behaviour of the wallet loaded in biaxial conditions (LBI).
- Series S09.HT.CBJ: carried out at high temperatures (HT) aiming to evaluate the creep (C) behaviour of the wallet under loading in the bed joints (BJ)
- Series S10.HT.CBI: carried out at high temperatures (HT) aiming to evaluate the creep (C) behaviour of the wallet under loading in biaxial conditions (BI)
- Series S11.HT.RBI: carried out at high temperatures (HT) aiming to evaluate the relaxation (R) behaviour of the wallet under loading in biaxial conditions (BI)

**Table 2 – Test series for the biaxial tests.**

| *Series* | Test Number | Temperature of the test | Load conditions | Type of control | Maximum load |
|---|---|---|---|---|---|
| *S06.AT. LBJ* | S06.AT. LBJ.01<br>S06.AT. LBJ.02 | Ambient Temperature | Bed directions: Loaded<br>Head direction: Constrained | Displacement | 6 MPa |
| *S07.AT. LHJ* | S07.AT. LHJ.01<br>S07.AT. LHJ.02 | | Bed directions: Constrained<br>Head direction: Loaded | Displacement | 6 MPa |
| *S08.AT.LBI* | S08.AT.LBI.01<br>S08.AT.LBI.02 | | Bed directions: Loaded<br>Head direction: Loaded | Displacement | 6 MPa |
| *S09.HT.CBJ* | S09.HT.CBJ.01<br>S09.HT.CBJ.02 | High Temperatures | Bed directions: Loaded<br>Head direction: Constrained | Load | 6 MPa<br>4 MPa |
| *S10.HT.CBI* | S10.HT.CBI.01<br>S10.HT.CBI.02 | | Bed directions: Loaded<br>Head direction: Loaded | Load | 4 MPa |
| *S11.HT.RBI* | S11.HT.RBI.01<br>S11.HT.RBI.02 | | Bed directions: Loaded<br>Head direction: Loaded | Displacement | 1st cycle: 4MPa<br>2nd cycle: 6MPa |

## 3.1 TEST SETUP

These experimental tests were carried out at the Technology Centre Leoben (TCL) of RHI-Magnesita, in Austria. This test setup has been used before (Prietl, 2006) and was improved for this experimental campaign. The schematic view of the test setup is presented in Figure 37. The test setup consisted of a monolithic reaction frame in which the hydraulic jacks, LVDTs and heating system were connected. Two orthogonal hydraulic jacks with the capacity of 1000 kN were used, with a Rexroth controller unit. The applied forces were measured by two pressure gauges per cylinder. A 48-channel data acquisition system was used to record the data from the experiments. The biaxial press is shown in Figure 38.

The specimens were placed on the top of an insulated platform, as shown in Figure 37b. The platform was responsible for holding the specimen and guarantee thermal insulation. It was composed of a 10 mm steel shell reinforced by square tubes (Figure 37b). Scaffolding feet were used to allow the proper levelling. The platform was lined with four refractory insulation layers (Figure 39). Ceramic wool was used to fill the gaps and guarantee proper insulation (Figure 39d). The last insulation layer had smaller dimensions, to allow the movement of the hydraulic jack. The gaps were filled using ceramic wool. The details of the bottom section are presented in Figure 39.



European Commission
Horizon 2020 European Union funding for Research & Innovation

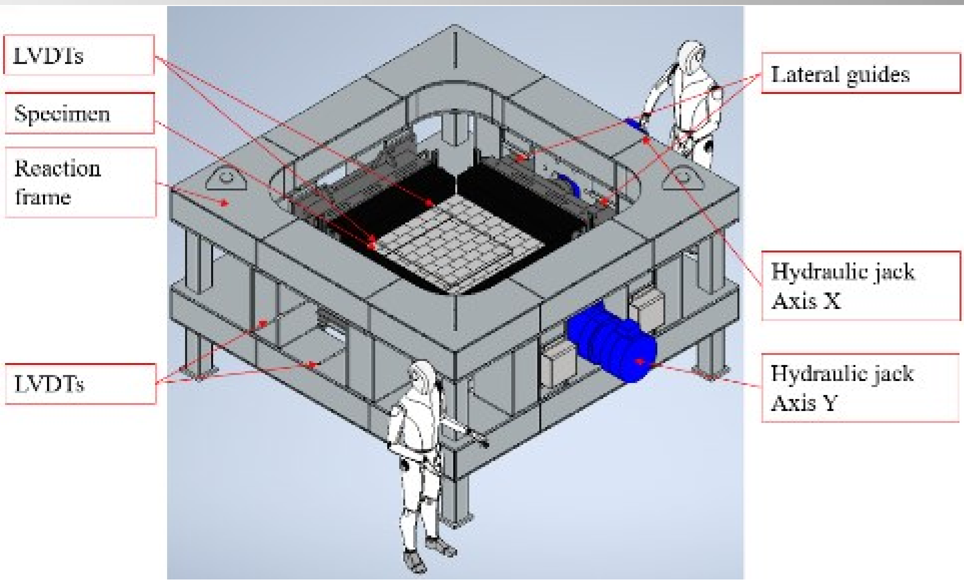


a)

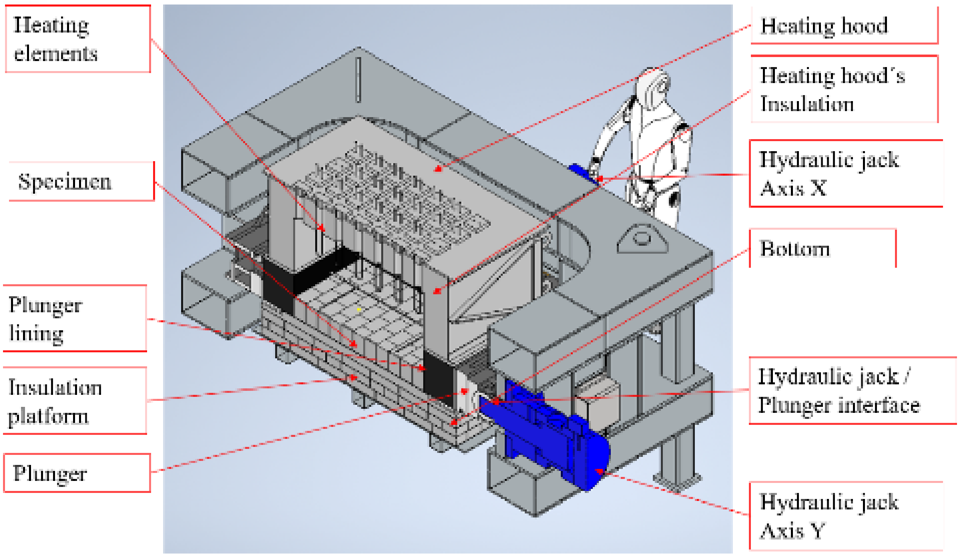


b)

**Figure 37 – Test setup: a) Isometric view and b) Section view.**

Figure 38 – Test setup for biaxial compression tests.

a)

b)

c)

d)

Figure 39 – Assembly of the insulation platform: a) Steel shell and first insulation layer, b) Second insulation layer, c) Last insulation layer and d) Last insulation layer with thermocouples and rockwool.

The mechanical load was applied to the specimen by the plungers. The machine was equipped with two fixed plungers and two movable plungers, as shown Figure 40. The plungers are composed of a water-cooled steel part and a refractory lining. The steel part was responsible for ensuring the loadbearing capacity, the refractory linings were responsible for withstanding the higher temperatures. Three openings were present in the fixed plungers for the placement of the instrumentation (thermocouples and LVDTS). The fixed plungers were rigidly connected to the machine frame. The moveable plungers were connected to the hydraulic jacks with pinned connectors, two additional lateral guides were employed to avoid rotations.



European Commission
Horizon 2020
European Union funding
for Research & Innovation

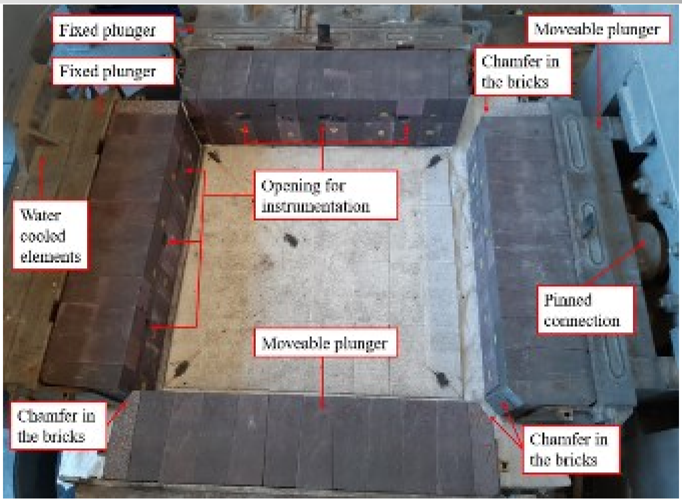


**Figure 40 – Plungers – General arrangement.**

The plungers' lining was made of dry-stacked magnesia-chromite bricks (Table 3). This brick has an elevated cold crushing strength (80 MPa), high resistance to creep in compression and a high refractoriness under load ($T_{0.5}$ = 1700 ºC). The plunger linings had 250 mm in thickness, 300 mm in height and 1100 mm in length. The bricks were dry-stacked on the steel part of the plungers (Figure 40a). The details of the bricks and the plunger final arrangements are shown in Figure 40. To avoid the contact of the plunger linings during the movement of the hydraulic jacks, 40 x 40 mm chamfers have been made in the edges of the linings, as detailed in Figure 40d. A drawback of this system is the non-uniformity in the loading of the brick positioned at the edge of the specimen.

**Table 3 – Chemical composition of the plungers' bricks.**

***Chemical analysis: Fired substance (1025 ºC) according to ISO 12677***

| ***MgO*** | **$Cr_2O_3$** | **$Al_2O_3$** | **$Fe_2O_3$** | **CaO** | **$SiO_2$** |
|---|---|---|---|---|---|
| *56.5 %* | 25.0 % | 6.0 % | 10.0 % | 0.6 % | 1.3 % |

a) b)

c) d)

Figure 41 – Plunger lining details: a) Plungers without the linings, b) Bricks of plungers' lining, c) Plungers with linings and d) Details in the lining to allow the plungers' movements.

The heating chamber was composed of an external steel shell insulated with ceramic wool (200 mm thickness). The heating elements chosen were Kanthal Super 1900, with thirty-six heating elements being used in the first tests, and latter being reduced to thirty to increase the power of the system. The total estimated power of the furnace was 59 kVA at 1500 ºC. The details of the heating chamber are given in Figure 42. A 100 kVA transformer with a secondary voltage of 95 V was used to feed the resistances. Two type S thermocouples were used to measure the temperature inside the heating chamber.

The correct insulation of the biaxial press is a key aspect to limit heat losses and reach the desired temperature. Ceramic wool blankets were used to insulate the bottom of the press, the edges of the linings, the interface between the furnace and the plungers and the exposed face of the plunger bricks. The ceramic wool was composed of $SiO_2$, CaO and MgO with a density of 128 kg/m$^3$. Different thicknesses (19, 25 and 50 mm) were used for improved insulation conditions.

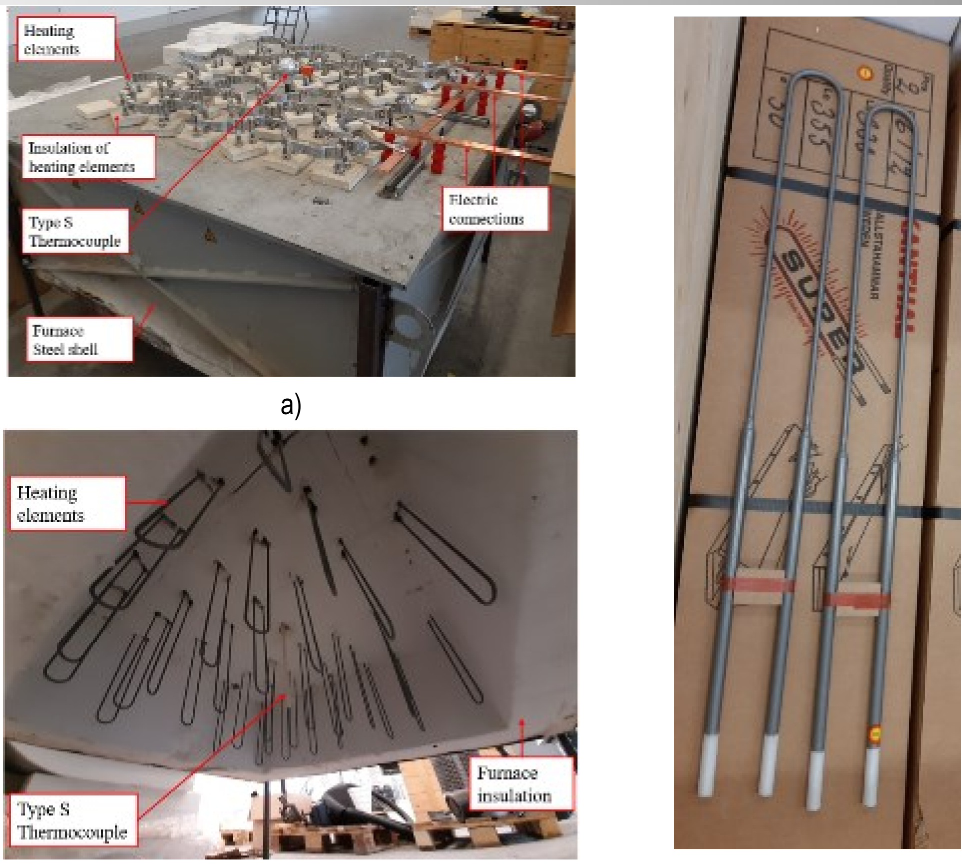


a) b) c)

Figure 42 – Heating chamber: a) Overview, b) Bottom view and c) Heating elements details.

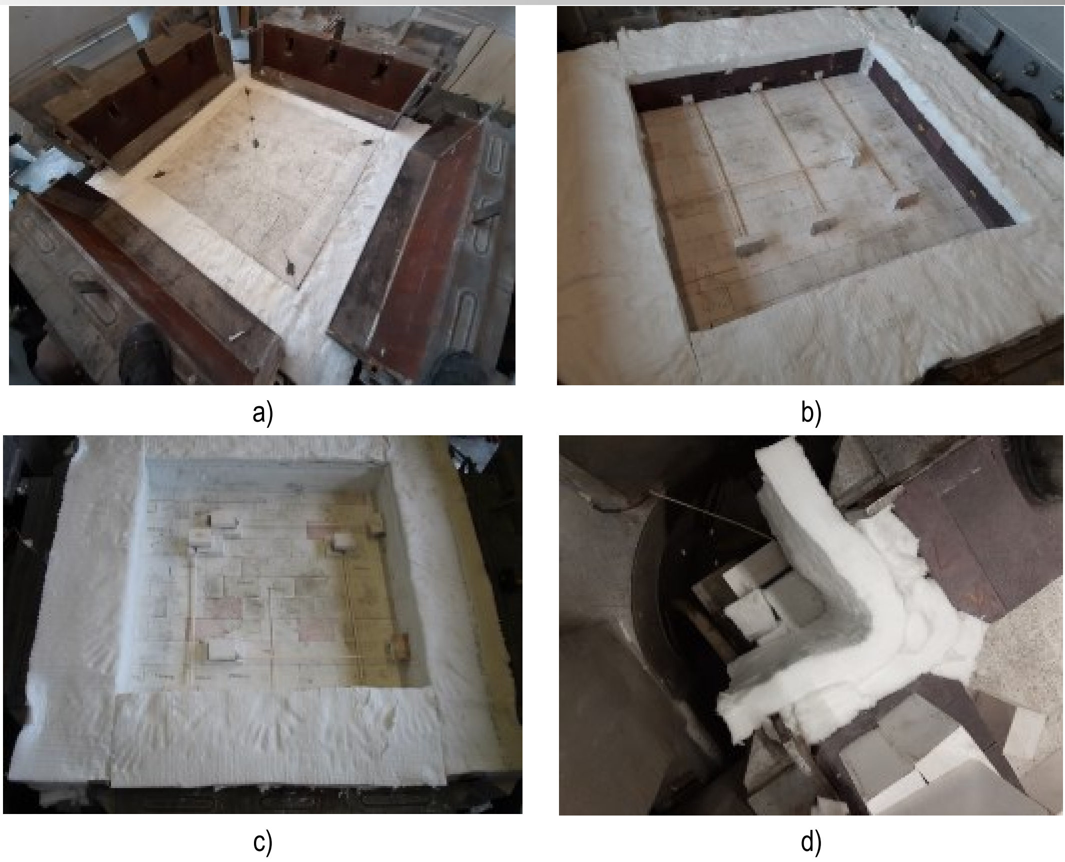


**Figure 43 – Insulation details: a) Bottom, b) Plunger interface with the heating chamber, c) Exposed face of the plungers and d) Details of plunger chamfers.**

A water-cooling system was used to control the temperatures in the plungers. Only the metallic part of the plungers was cooled (Figure 44a). The system was composed of two pipelines, one used for input of the cold water and the other used for output of the hot water. The input and output hydraulic connections of the plungers were equipped with type K thermocouples to measure the water's temperature. A mechanical valve was used to control the water flow.



European Commission
Horizon 2020
European Union funding
for Research & Innovation

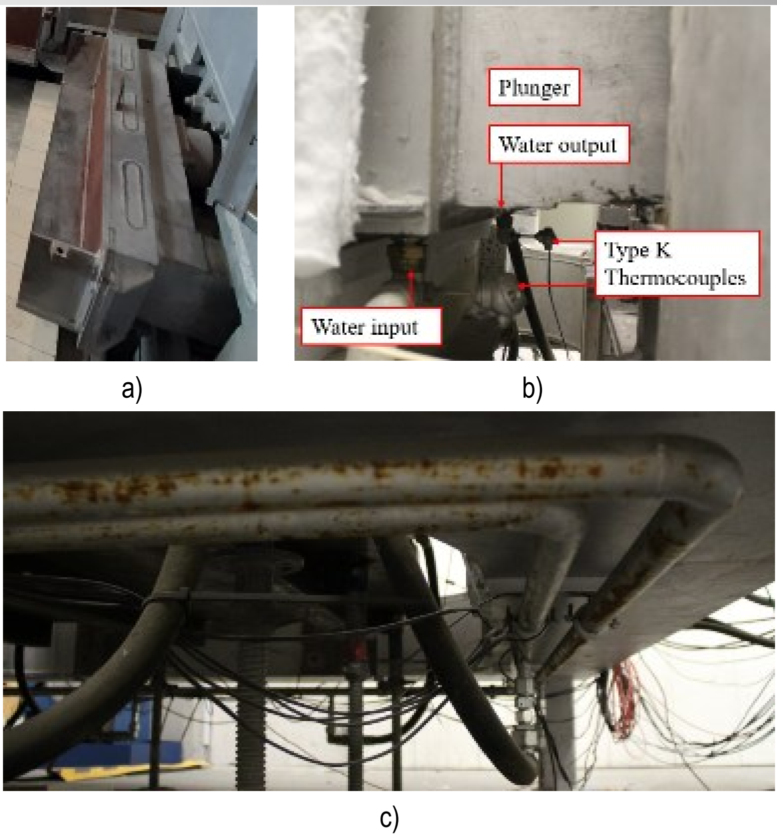


Figure 44 – Water cooling details: a) Cooled part of plungers, b) Thermocouples of the system and c) Pipes.

## 3.2 SPECIMENS AND INSTRUMENTATION

The specimens consisted of dry-stacked masonry walls made of the same bricks used in the uniaxial experimental campaign presented in the previous section. The properties of the material were described in previous deliverables. Figure 45 presents the general arrangement of the specimens. The tested specimens had eleven courses of bricks, each course had seven bricks and one half brick. The thickness of the wallet (140 mm) was based on the usual thickness of the working linings of steel ladles. The in-plane dimensions of the wall (1100 x 1125 mm) were based in the inner dimension of the test field of the biaxial press.

The displacements were measured using inductive LVDTs WA-50 manufactured by HBM. The measurement range of the equipment is 50 mm. For the tests performed at ambient temperature, the LVDTs were fixed at the tip of a corundum tube (ø15 x ø11 x 400mm), the other tip was fixed in the bricks using two steel angle sections (Figure 46). A second corundum tube (ø8 x ø5 x 1225 mm) was placed concentrically to the external tube and fixed in the sample using another steel piece and a screw (Figure 46). The general arrangement of the LVDT system is presented in Figure 46. This system allowed the measurement of the relative displacement between both fixed supports. The location of the LVDTs for test series S06.AT.LBJ, S07.AT.LHJ and S08.AT.LBI is given in Figure 47, Figure 48 and Figure 49, respectively.

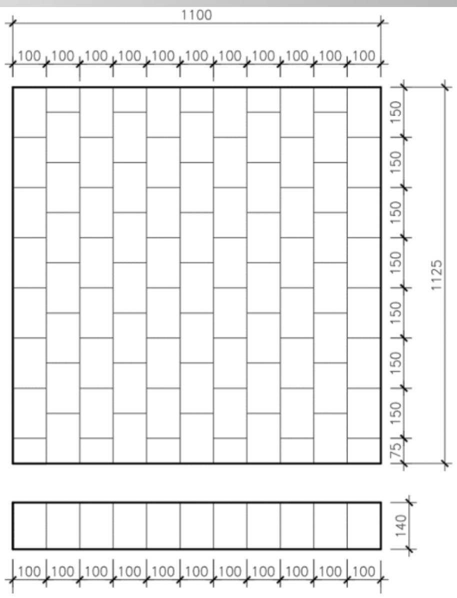


Figure 45 – Biaxial specimens' dimensions [mm].

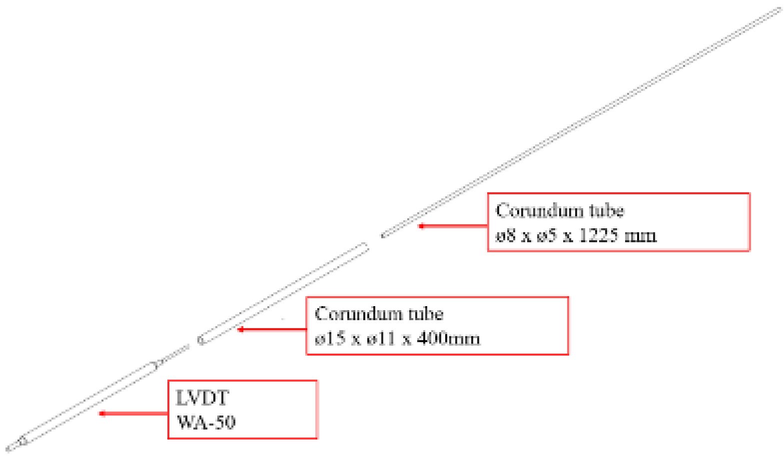


a)

b) c) d)

Figure 46 – LVDTs used in the ambient temperature test: a) Schematic detail, b) Overview, c) Detail of fixation and d) Detail of fixation.

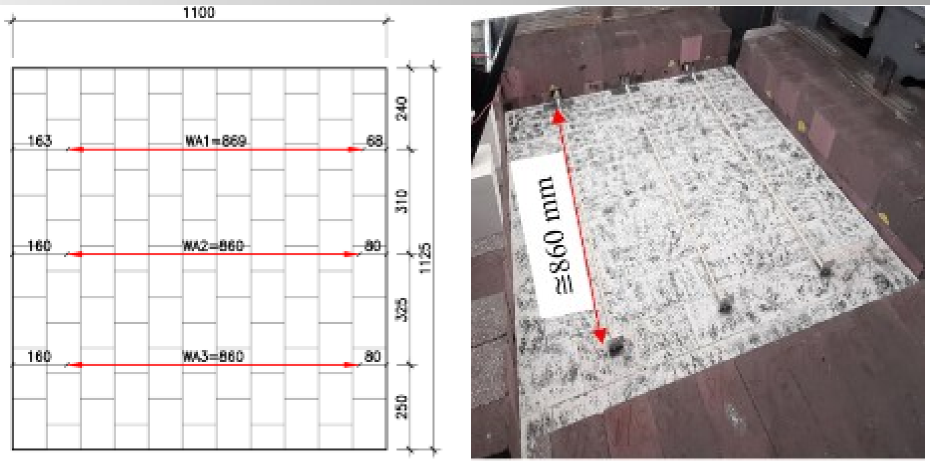


a) b)

**Figure 47 – LVDTs used at test series S06.AT.LBJ: a) Location and b) Overview.**

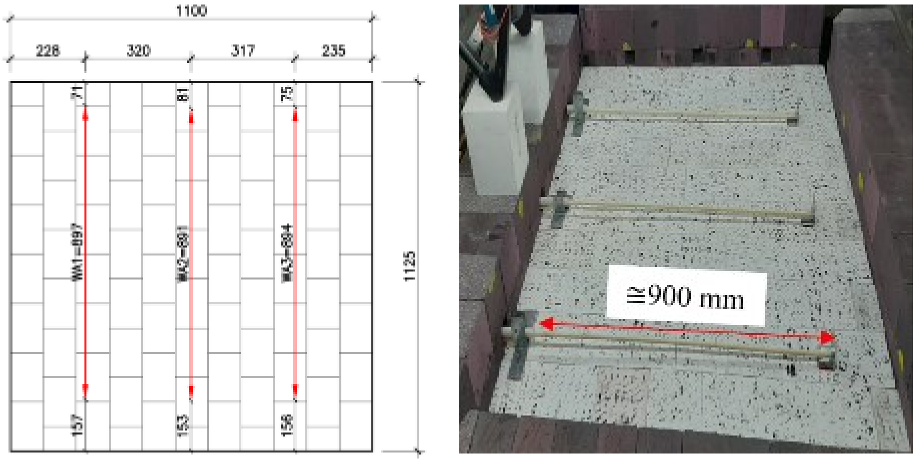


a) b)

**Figure 48 – LVDTs used at test series S07.AT.LHJ: a) Location and b) Overview.**

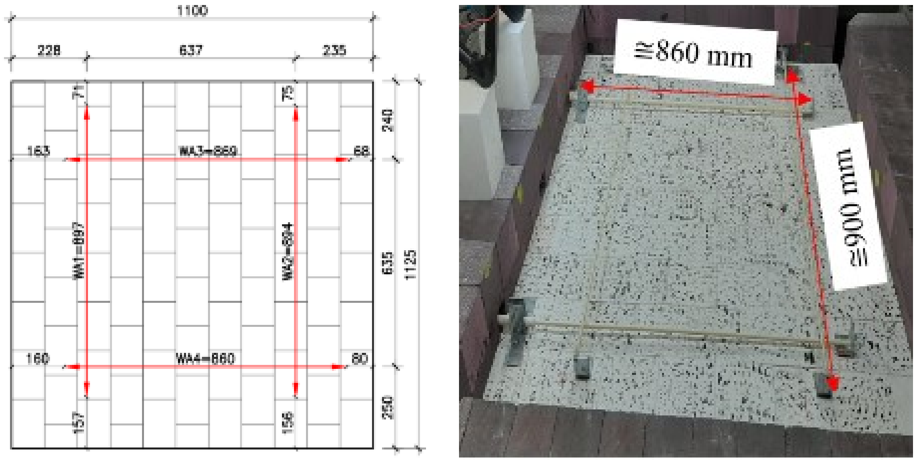


a) b)

**Figure 49 – LVDTs used at test series S08.AT.LBI: a) Location and b) Overview.**

The LVDT system used in the high temperature tests followed the same concept of the one used in the ambient temperature tests but with some extra components (Figure 50). The LVDT (2) was fixed to a metallic tube (1) by two screws (3). In the other tip of the metallic tube (1) a corundum tube (4) was fixed, the corundum tube (4) was also fixed in the specimen. A second corundum tube (5) was placed concentrically to the tubes (1 and 4) and fixed to the specimen. A third corundum tube (6) with a type B thermocouple was placed inside the tube (5). A metallic piece (7) was used to fix the tubes (5) and (6) to the LVDT (1). The components of the LVDT system are detailed in Figure 51. The location of the LVDTs for test series S09.HT.CBJ, and S10.HT.CBI/ S11.HT.RBI are given in Figure 52 and Figure 53, respectively.

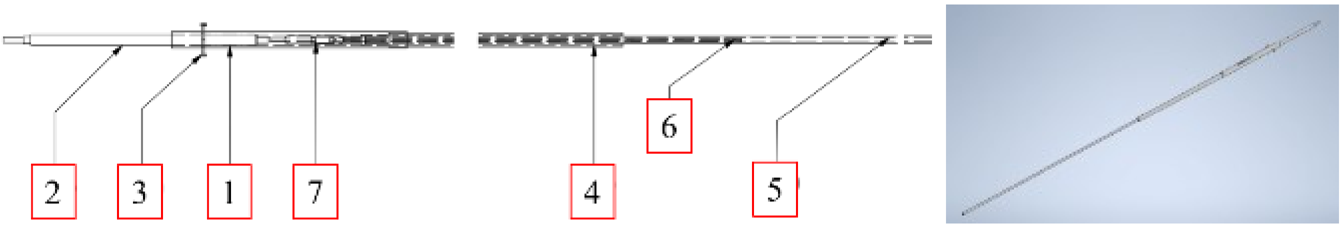


**Figure 50 – LVDT system for elevated temperatures.**

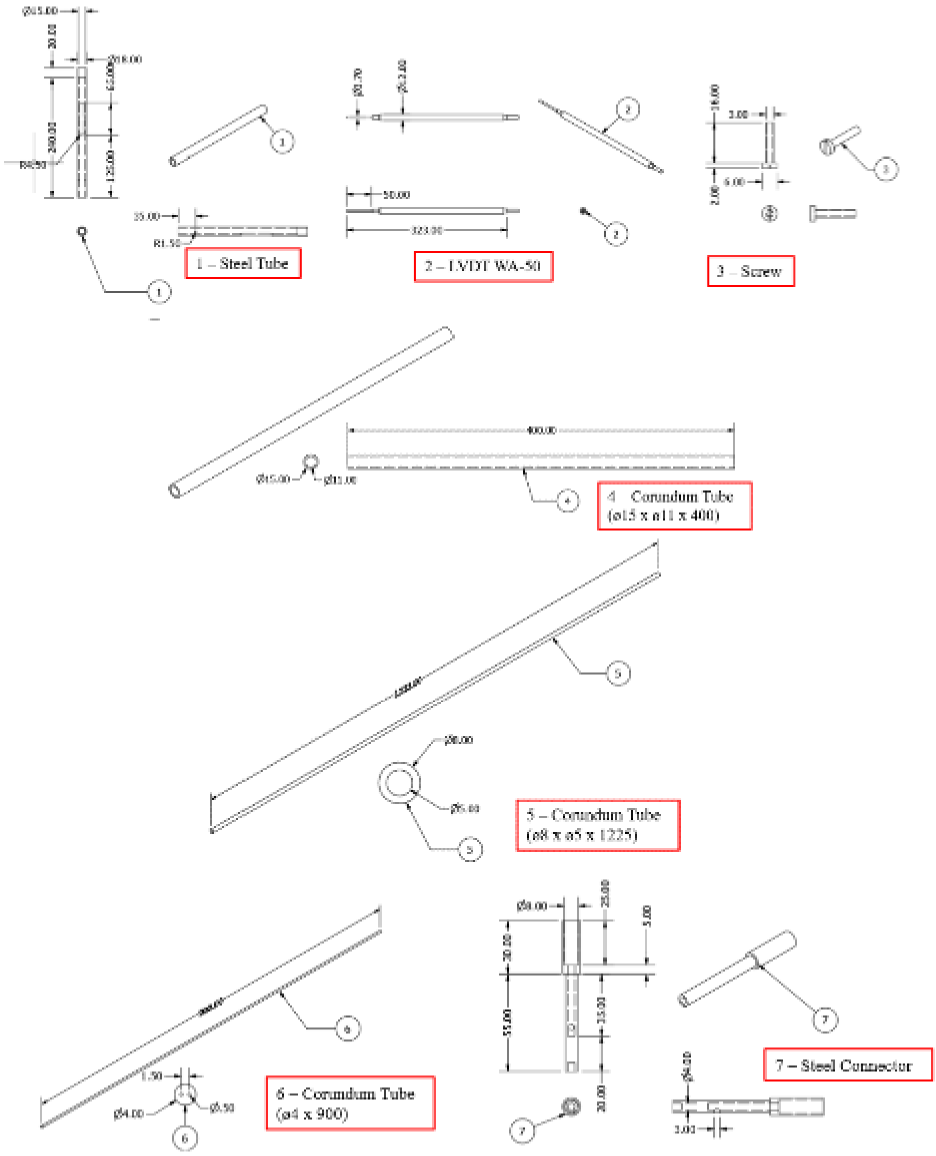


**Figure 51 – Components of the LVDTs system.**

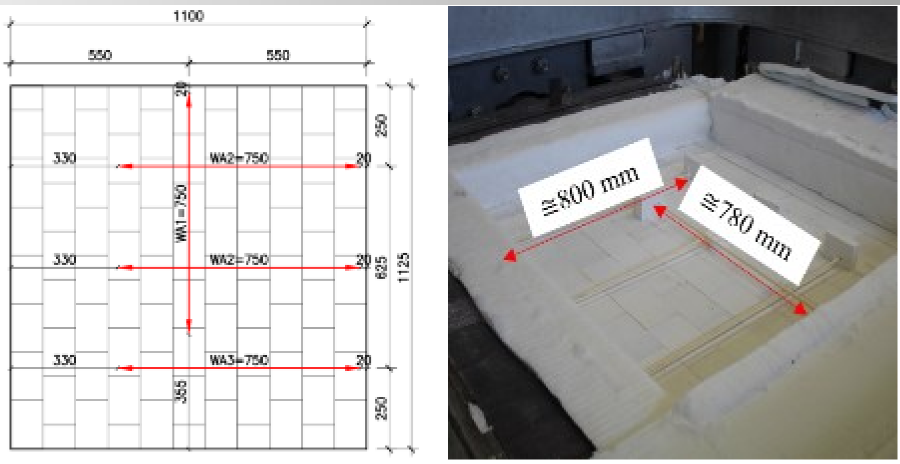


a) b)

**Figure 52 – LVDTs used at test series S09.HT.CBJ: a) Location and b) Overview.**

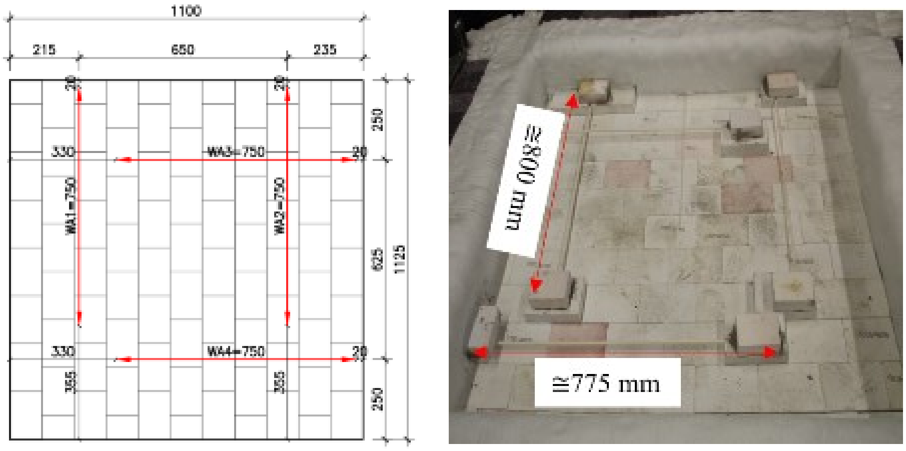


a) b)

**Figure 53 – LVDTs used at test series S10.HT.CBI and S11.HT.RBI: a) Location and b) Overview.**

DIC (Dupre et al, 2018; Belrhiti et al, 2017; Besnard et al, 2006) was also used to measure the in-plane displacements fields in the tests performed at ambient temperature. Despite recent developments in the use of DIC at high temperatures (Teixeira et al, 2019; Kackzmareck et al, 2019), the absence of windows in the furnace did not allow the use of the technique for the other tests. An 18 MPx (5184 x 3486) camera was used for image acquisition and three LED reflectors were used for lighting. The adopted configuration allowed to plot the in-plane displacements and strain field obtained during the tests. The image processing was performed using subsets of 120 × 120 pixels. The speckle pattern application had the following steps: *i*) the bricks were laid on a horizontal plane; *ii*) the speckle pattern was applied by means of a paintbrush; *iii*) a dwell time of 24 hours was considered for drying. The speckle pattern application, its details and the DIC system are shown in Figure 54, the DIC results were used to validate the measurements of the LVDTs.

The thermal instrumentation comprised five Type B thermocouples installed at the cold face of the wall, five Type B thermocouples installed in the hot face and two Type S thermocouples in the heating chamber. The thermocouple wires (ø 0.5 mm) were placed inside alumina tubes for protection and to avoid undesired contact of the wires. The Type B thermocouples are composed of Platinum-Rhodium (30 %) / Platinum-Rhodium (6 %) alloys and can operate from 0 - 1700 ºC. The Type S are made with Platinum-Rhodium (10 %) / Platinum and can operate from 0ºC to 1600 ºC. The Type S thermocouples installed in the middle of the heating chamber were also placed inside an alumina tube, as shown in Figure 55. One thermocouple was used to feed the furnace controller and the other one was connected to the data acquisition system. The thermocouples of the cold face were placed in the upper face of the last insulation layer, in contact with the cold face of the specimen (Figure 56).

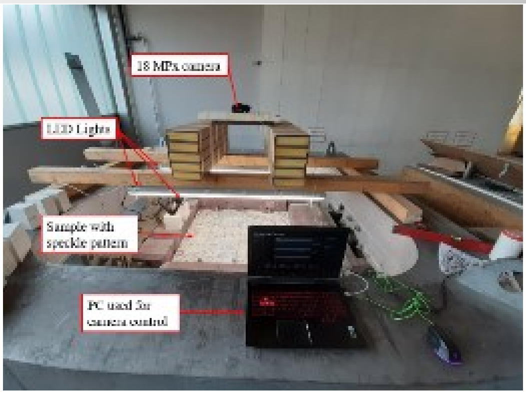


c)

d)

**Figure 54 – Digital Image Correlation: a) DIC set-up and b) DIC details.**

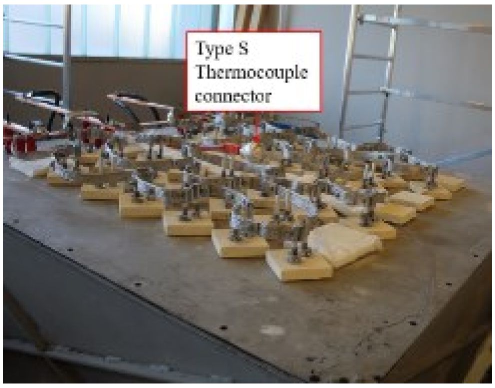


a)

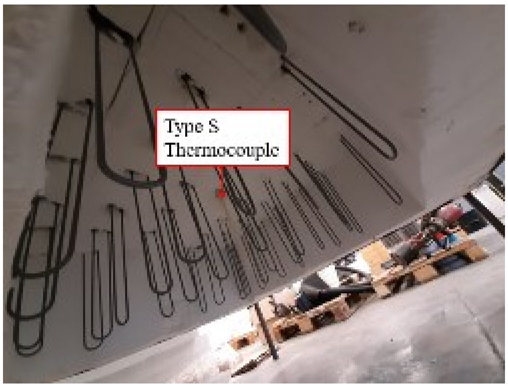


b)

**Figure 55 – Heating chamber thermocouple: a) External view and b) Internal view.**

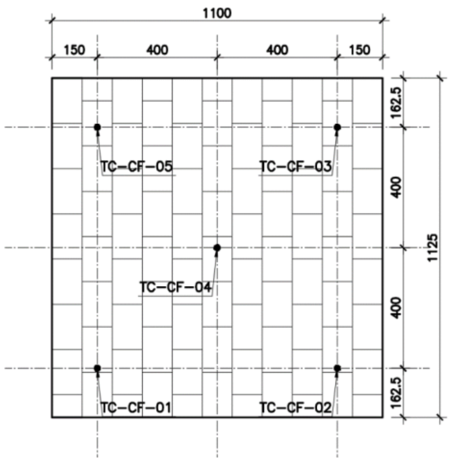


a)

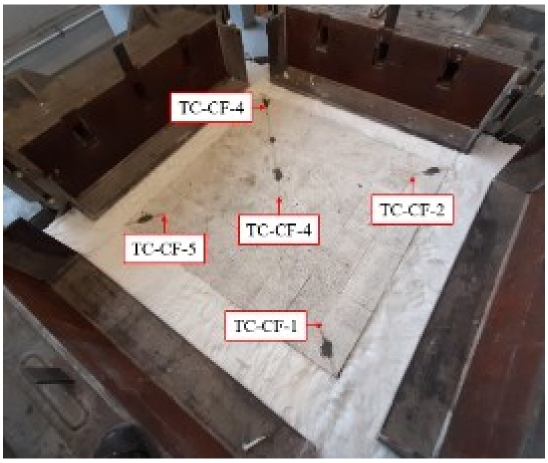


b)

**Figure 56 – Thermocouples of cold face: a) Location and b) Details.**

The LVDT instrumentation of test series S09.HT.CBJ was different from the one used for test series S10.HT.CBI and S11.HT.RBI. The thermocouples of the hot face were installed inside the LVDT tubes; therefore, their positions were also different. The location of the thermocouples used in test series S09.HT.CBJ is given in Figure 57. Figure 58 presents the details of the thermal instrumentation of S10.HT.CBI and S11.HT.RBI.

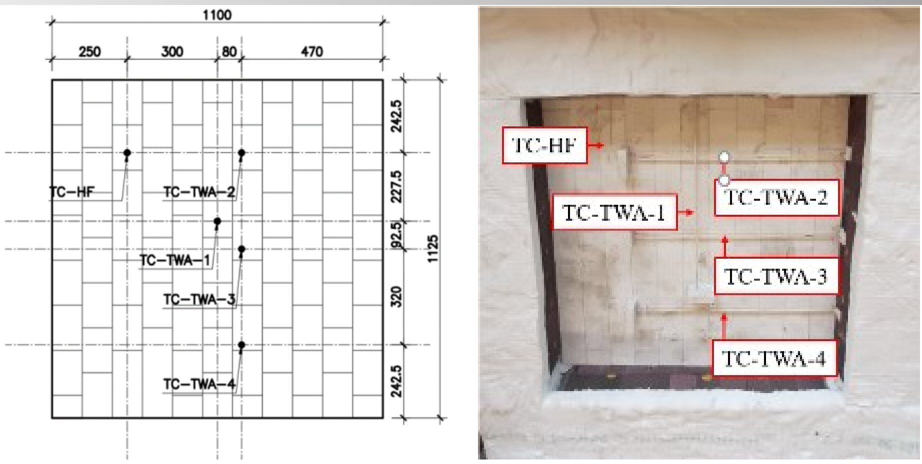


a) b)

**Figure 57 – Thermocouples of hot face – S09.HT.CBJ: a) Location and b) Thermocouple distribution.**

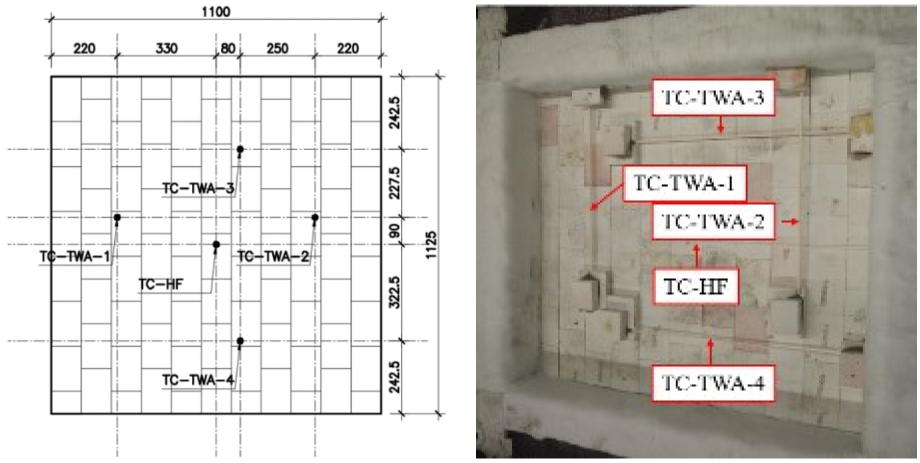


a) b)

**Figure 58 – Thermocouples of hot face – S10.HT.CBI and S11.HT.RBI: a) Location and b) Thermocouple distribution.**

## 3.3 TEST PROCEDURE

The following test procedures were used in the different test series:

- **Test series S06.AT.LBJ:** The objective of test series S06.AT.LBJ was to assess the loadbearing capacity of the refractory masonry walls loaded in direction of the bed-joints, with a mechanical constraint, provided by the blocked pungles, in the direction of the head-joints. The test procedure in series S06.AT.LBJ had the following steps: *i*) the masonry specimens were built in the testing field; *ii*) the instrumentation was installed; *iii*) a pre-compressive load of 20 kN was applied in both directions to ensure that the LVDTs are reading; *iv*) the specimen was loaded in the direction perpendicular to the bed joints under displacement control at a rate of 0.02 mm/s up to the maximum load of 6 MPa; *v*) when the maximum load was reached, the specimen was unloaded at the same rate; *vi*) steps *iv* and *v* were repeated twice.
- **Test series S07.AT.LHJ:** The objective of test series S07.AT.LHJ was to assess the loadbearing capacity of the refractory masonry walls loaded in the direction of the head-joints, with a mechanical constraint in the direction of the bed-joint. The test procedure was the same of S06.AT.LBJ, however, the loading direction was different and the displacement rate was 0.007 mm/s.
- **Test series S08.AT.LBI:** Series S08.AT.LBI aimed to assess the mechanical behaviour of masonry wallets at ambient temperature loaded under biaxial conditions. Steps *i*, *ii* and *iii* of the test procedure were similar to the ones presented for series S06.AT.LBJ. Then: *iv*) the specimen was loaded in both directions under displacement control at a rate of 0.007 mm/s up to the maximum load of 6 MPa. Trial tests were performed to determine the optimum parameters of the

controller (speed, displacement increment and acceleration) that will result in $\sigma_X/\sigma_Y = 1$, Then the optimum parameters were used for the biaxial tests. *v*) when the maximum load was reached in both directions, the specimen was unloaded at the same rate; *vi*) steps *iv* and *v* were repeated twice.

- **Test series S09.HT.CBJ:** The objective of series S09.HT.CBJ was to assess the creep behaviour of refractory masonry walls subjected to uniaxial creep. Steps *i*, *ii* and *iii* of the test procedure were similar to the ones presented for series S01.AT.LBC. Then: *iv*) the furnace was placed in position; *v*) the sample was heated; *vi*) a dwell time of 18 hours was considered; *vii*) the mechanical load was applied in direction *X (same as LBJ)* under displacement control at a rate of 0.007 mm/s; *viii*) the hydraulic jacks were set to force control to keep the current force; *ix*) the specimen was monitored for 18 hours, with temperatures and displacements being recorded; *x*) the specimen was unloaded and two more load cycles were performed.
- **Test series S10.HT.CBI:** The objective of series S10.HT.CBI was to assess the creep behaviour of refractory masonry walls subjected to biaxial creep. Steps *i)* to *vi)* of the test procedure were similar to the ones presented for series S09.HT.CBJ. Then: *vii*) the mechanical load was applied in both directions under displacement control at a rate of 0.007 mm/s; *viii*) the hydraulic jacks were set to force control to keep the current force; *ix*) the specimen was monitored for 16 hours; *x*) the specimen was unloaded and two more load cycles were performed.
- **Test series S11.HT.RBI:** The objective of series S11.HT.RBI was to assess the relaxation behaviour of refractory masonry walls subjected to biaxial loading. Steps *i)* to *vi)* of the test procedure were similar to the ones presented for series S09.HT.CBJ. Then: *vii*) a mechanical load of 4 MPa was applied in both directions under displacement control at a rate of 0.007 mm/s; *viii*) the hydraulic jacks were set to keep the same position; *ix*) the specimen was monitored during the relaxation process; *x*) the specimen was unloaded; *xi*) steps *vii)* to *x)* are repeated once with the load level of 6 MPa.

The heating procedure comprised the following steps: *i*) from ambient temperature to 500 ºC over a period of ten minutes; *ii*) from 500 ºC to 1500 ºC over a period of ten hours; *iii*) dwell time of 18 hours at 1500 ºC.

## 3.4 RESULTS AND DISCUSSION

The experimental results are presented and discussed in this section. For each test series, results in terms of displacements, strains, forces, stresses, temperatures are presented and discussed. Wherever possible, comparisons with literature results are made.

### 3.4.1 Test series S06.AT.LBJ

Test series S06.AT.LBJ aimed to evaluate the mechanical behaviour of masonry wallets loaded in bed joints direction with lateral restraints in the direction of the head joints. The evolution of the in-plane displacements measured in the tests are presented in Figure 59. The LVDTs used to measure the in-plane displacements (WA-2, WA-3 and WA-4 in the bed-joint direction) and the average of their values (WA-Avg) are presented. As expected for masonry walls and as observed in the previous tests, a small scattering of the in-plane displacements can be observed due to the dimension errors of the bricks and non-flatness of the surface in contact with the plungers.

The measured forces during the test are shown in Figure 60. It should be noted that after reaching the maximum applied load level, there was around 100 seconds dwell time. This dwell time allowed the camera to take several images of the wall at the maximum load level. The lateral restraint provided by the blocked plunger prevented elongation of the wall in the direction perpendicular to the loading (due the Poisson's effect), consequently, a reaction force was observed in this direction (direction perpendicular to the head-joints). In test series S06.AT.LBJ.01 and S06.AT.LBJ.02 these maximum reaction forces were 103. kN (0.67 MPa) and 101.3 kN (0.66 MPa), respectively.

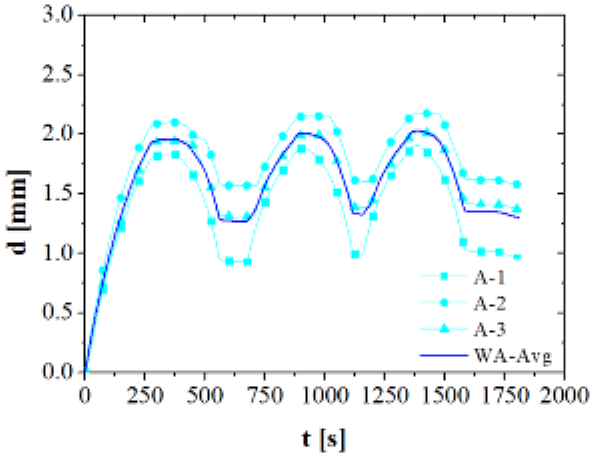


a)

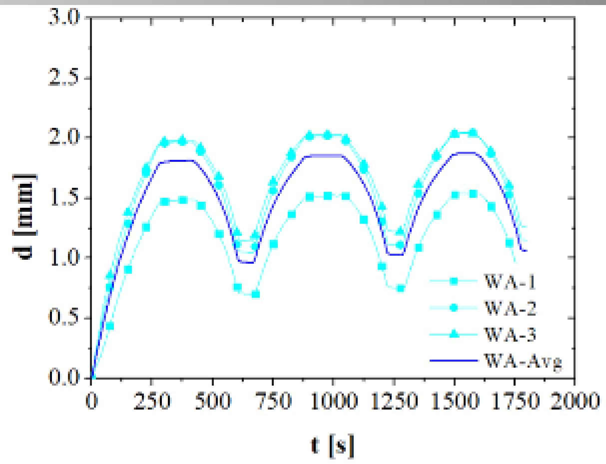


b)

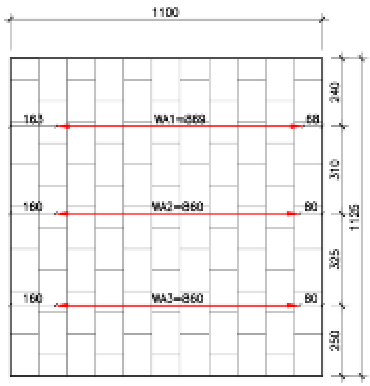


c)

**Figure 59 – Test series S06.AT.LBJ – In-plane displacements in the bed-joint direction: a) S06.AT.LBJ.01, b) S06.AT.LBJ.02 and c) LVDT locations.**

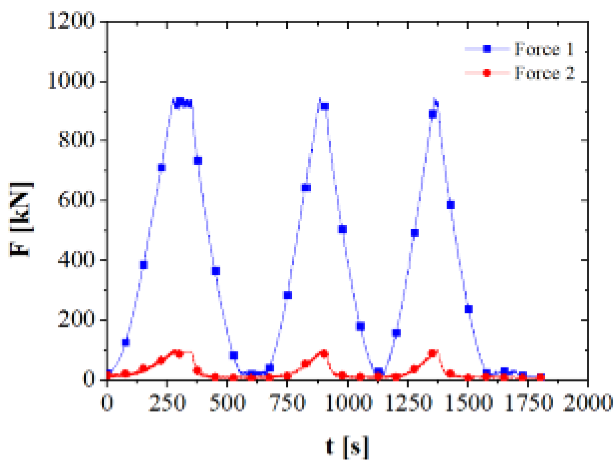


a)

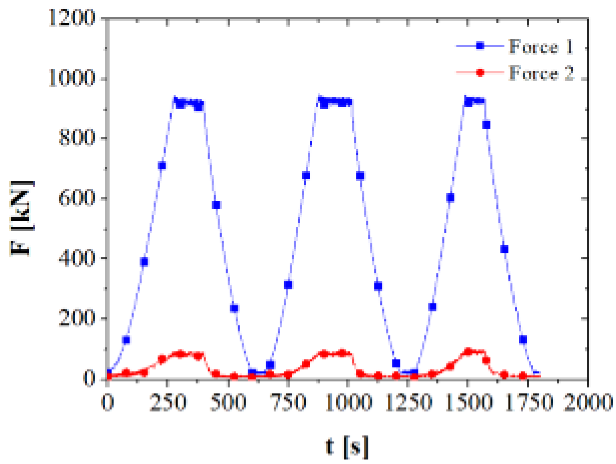


b)

**Figure 60 – Test series S06.AT.LBJ – Applied force in the direction perpendicular to the bed-joints (Force 1) and reaction force perpendicular to the head-joints (Force 2): a) S06.AT.LBJ.01 and b) S06.AT.LBJ.02.**

The stress-strain curves obtained in test series S06.AT.LBJ are presented in Figure 61. A small scattering was observed between the tests results. As noticed in test series S02.AT.CIC, an increasing of the wall Young's modulus is observed after the loading stage, caused by the increasing of the contact area between the bricks. The maximum strain obtained for test series S06.AT.LBJ.01 and S06.AT.LBJ.02 was 0.0024 and 0.0022, respectively. As observed in test series S02.AT.CIC (Section 2.3.2), residual strains are obtained after the first loading cycle. The average residual strain after the first load cycle for test series

S06.AT.LBJ.01 and S06.AT.LBJ.01 was 0.0015 and 0.0012, respectively. The increasing of the residual strains after the second and third load cycles were not significant.

In test series S06.AT.LBJ, a sudden drop of stresses at the beginning of the unloading stage was observed. This was caused by the methodology used to measure the forces. The forces were calculated based on the pressure gages of the hydraulics, as the experimental setup does not allow the use of loadcells, due to the limited space. As observed in test series S02.AT.CIC, a few cracks were detected in the specimen (Figure 62) despite the small load level applied (6 MPa). The cracks were mostly located at the cross-joints and were caused by the non-uniform loading and support conditions of the blocks.

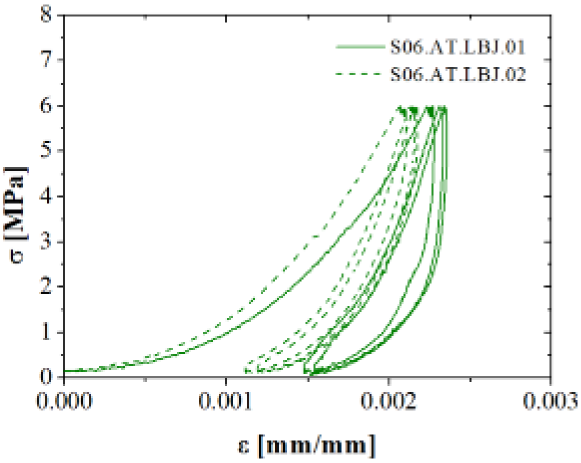


**Figure 61 – Test series S06.AT.LBJ – Stress-strain curves.**

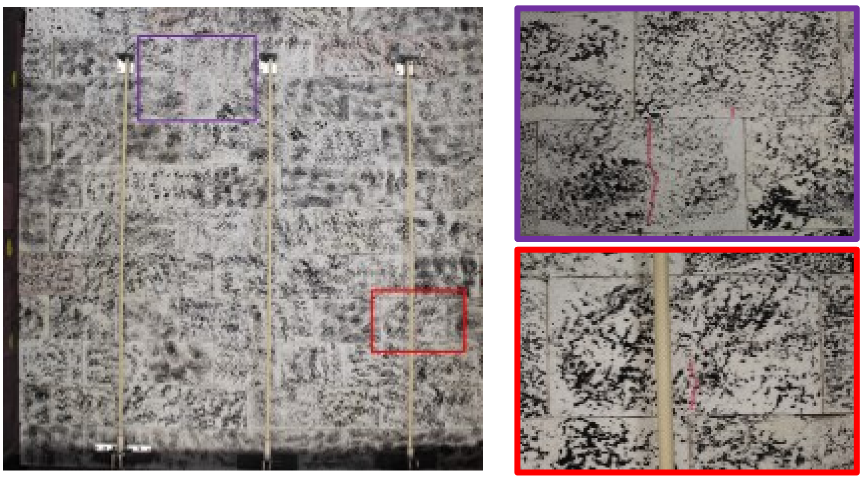

**Figure 62 – Test series S06.AT.LBJ – Cracks observed (in red) in the specimen S06.AT.LBJ.01. Left picture macroscopic view, right pictures specific zoomed sections.**

The full displacement fields obtained using DIC, in the direction perpendicular to bed-joints, of S06.AT.LBJ.01 at 25 %, 100 % of maximum load level and after unloading are presented in Figure 63. It should be noted that all DIC results presented are turned 90º in the XY plane in comparison to Figure 59c presenting LVDT locations. In agreement with S01 and S02, non-uniform displacement fields can be seen. Higher values of the displacement at the left side of the wall can be observed. In addition, after unloading, there was a permanent deformation of the wall. This is due to the fact that the final joint thickness after unloading is usually smaller when compared to the initial one. This behaviour was also observed from cyclic loading and unloading of two stacks of bricks.

### 3.4.2 Test series S07.AT.LHJ

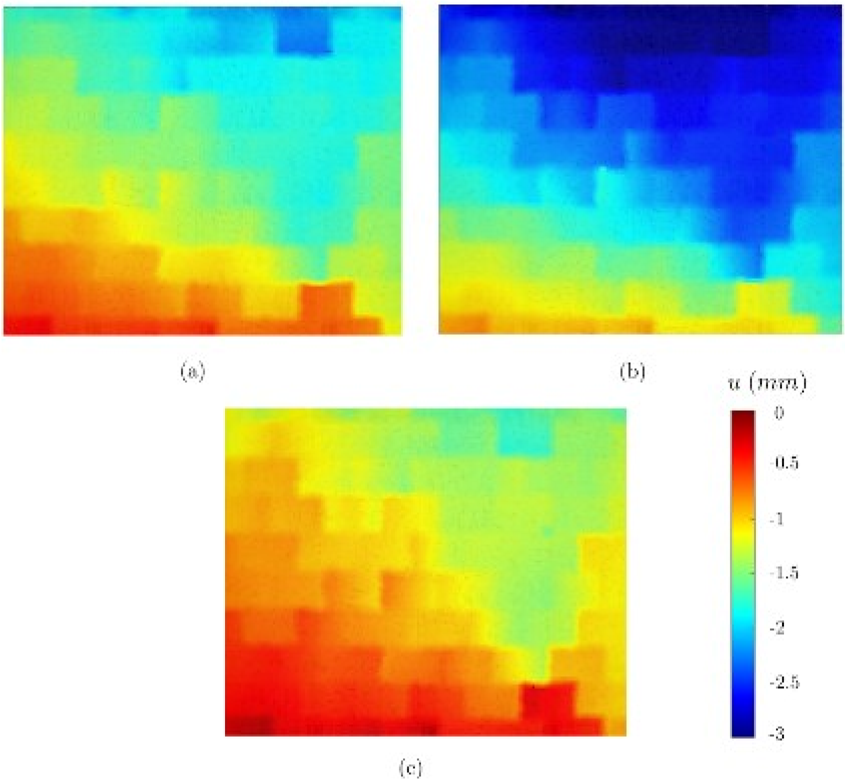


**Figure 63 - Displacement fields in S06.AT.LBJ.01, in the direction perpendicular to bed-joints (vertical direction in this picture), at: (a) 25 %, (b) 100 % of maximum load level and (c) after unloading.**

Test series S07.AT.LHJ, aims to evaluate the mechanical behaviour of masonry wallets loaded in the direction perpendicular to the head-joints, with lateral restraints in the direction perpendicular to the bed-joints. The evolution of the in-plane displacements measured in the tests are presented in Figure 64. The LVDTs used to measure the in-plane displacements (WA-1, WA-2 and WA-3 in the direction perpendicular to the head-joints) and the average of their values (WA-Avg) are presented. Higher scattering between the measurements of the LVDTs was observed in comparison to uniaxial compression tests in the direction perpendicular to bed-joints. This higher scattering is caused by the high dimensional errors of the bricks in the direction perpendicular to head-joints (± 2 mm). However, the scattering between the average displacements of the two tests is still acceptable (around 25%). The maximum strain obtained for test series S07.AT.LHJ.01 and S07.AT.LHJ.02 was 0.0015 and 0.0010, respectively. As observed in test series S06.AT.LBJ, no significant increase on the maximum strains were observed for the second and third load cycles when compared to the first cycle. The residual strains caused by the crushing of initial non-plane surfaces of the bricks was also observed in this test series. The average residual strain after the first load cycle for test series S07.AT.LHJ.01 and S07.AT.LHJ.01 was 0.0010 and 0.0005, respectively. As observed in test series S06.AT.LBJ, the increase of the residual strain after the second and third load cycles was not significant.

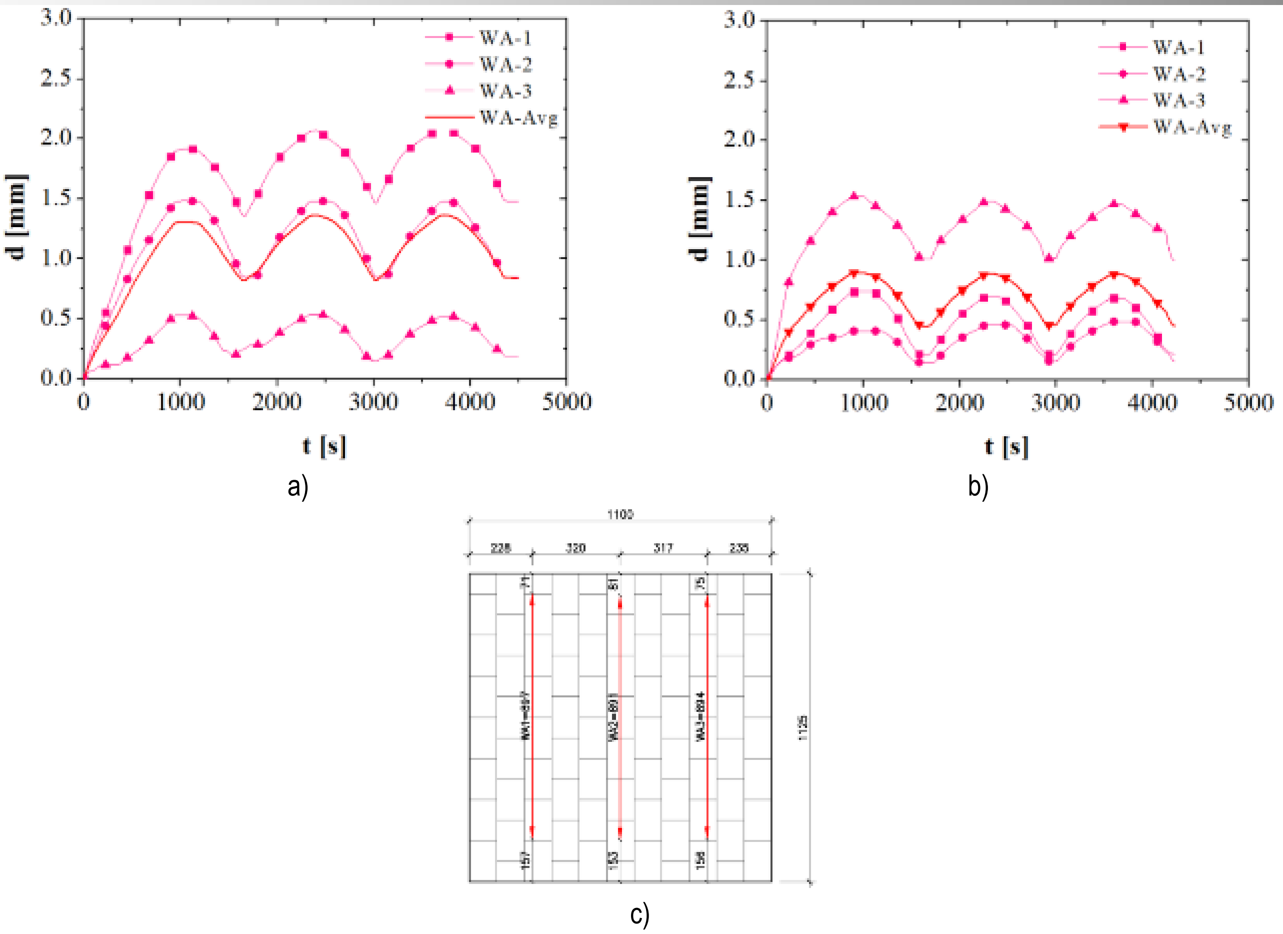


**Figure 64 – Test series S07.AT.LHJ – In-plane displacements in the direction perpendicular to the head-joints: a) S07.AT.LHJ.01, b) S07.AT.LHJ.02 and c) LVDT locations.**

The measured forces and stresses during the test are shown in Figure 65 and Figure 66, respectively. The lateral restraint provided by the blocked plunger prevents the elongation of the wall in the direction perpendicular to the loading (Poisson's effect), therefore, a reaction force (Force 1 in this case) was observed in this direction (direction perpendicular to bed-joints). In test series S07.AT.LHJ.01 and S07.AT.LHJ.02 the maximum reaction forces were 149.8 kN (0.95 MPa) and 115.8 kN (0.74 MPa), respectively. Due to the higher stiffness of the wall in the direction perpendicular to the head-joints, the reaction forces were slightly higher than the ones obtained in test series S06.AT.LBJ.

The stress-strain curves obtained in test series S07.AT.LHJ are presented in Figure 67. A higher scattering of the results were observed when compared to test series S06.AT.LBJ. As noticed in test series S02.AT.CIC and S06.AT.LBJ, an increasing of the wall Young's modulus is observed after the loading stage. The sudden drop of stresses at the beginning of the unloading stage was previously discussed and it is also observed in this test series.

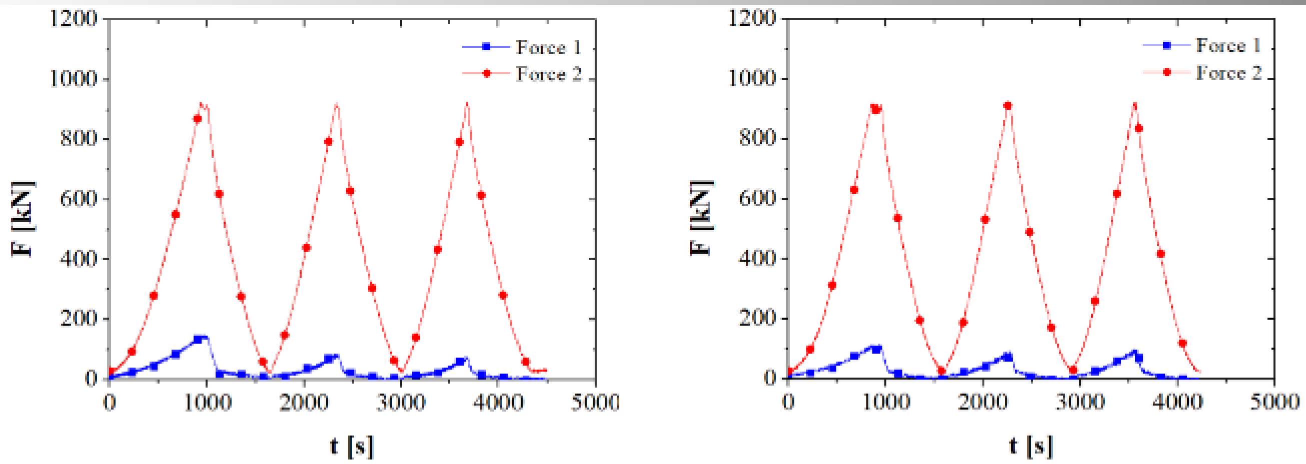


a) b)

Figure 65 – Test series S07.AT.LHJ – Applied force in the direction perpendicular to the head-joints (Force 2) and reaction force perpendicular to the bed-joints (Force 1): a) S07.AT.LHJ.01 and b) S07.AT.LHJ.02.

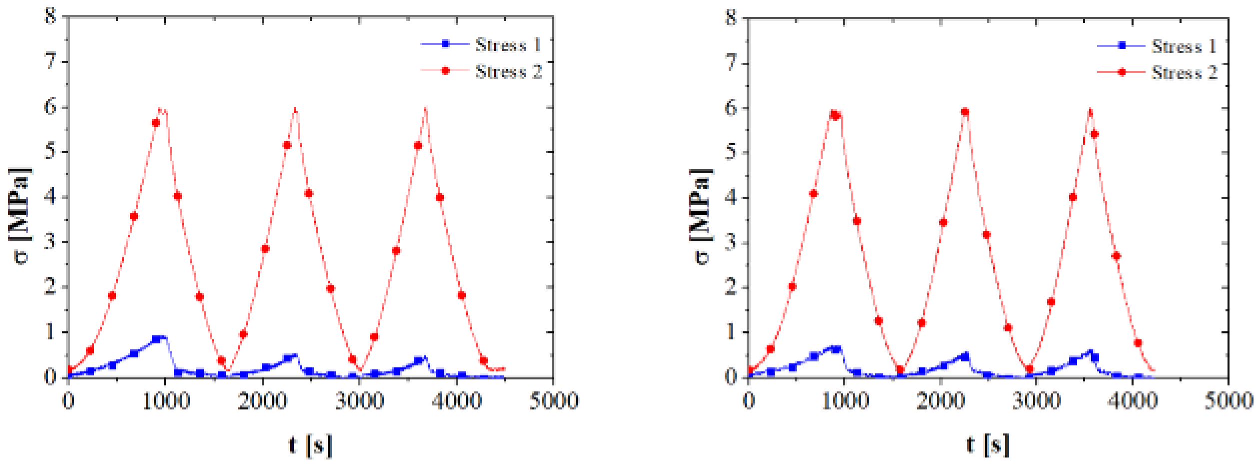


a) b)

Figure 66 – Test series S07.AT.LHJ – Applied stress in the direction perpendicular to the head-joints (Stress 2) and reaction stress perpendicular to the bed-joints (Stress 1): a) S07.AT.LHJ.01 and b) S07.AT.LHJ.02.

The stress-strain curves obtained in test series S07.AT.LHJ are presented in Figure 67. A higher scattering of the results were observed when compared to test series S06.AT.LBJ. As noted in test series S02.AT.CIC and S06.AT.LBJ, an increasing of the walls Young's modulus is observed after the loading stage. The sudden drop of stresses at the beginning of the unloading stage was previously discussed and it is also observed in this test series.

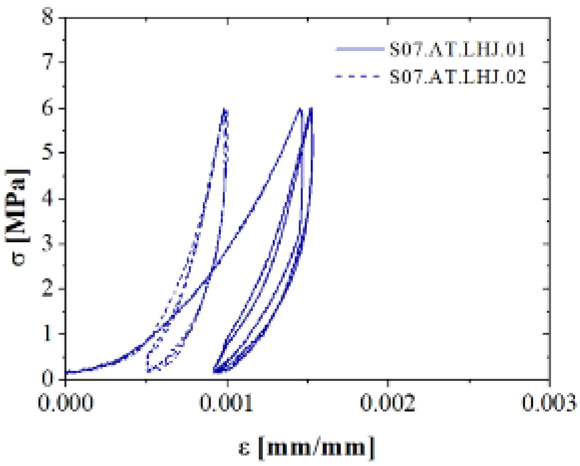


Figure 67 – Test series S07.AT.LHJ – Stress-strain curves.

In spite of the small load level applied to the specimen (6 MPa), some cracks were observed close to the head-joints, as shown in Figure 68a. The crushing of the bricks edges was also identified (Figure 68b and c), most likely caused by the concentration of stresses due to shape imperfections in the bricks. A few cracks were also observed close to the cross-joints (Figure 68d), caused by the reaction force in the direction perpendicular to the loading.

a)

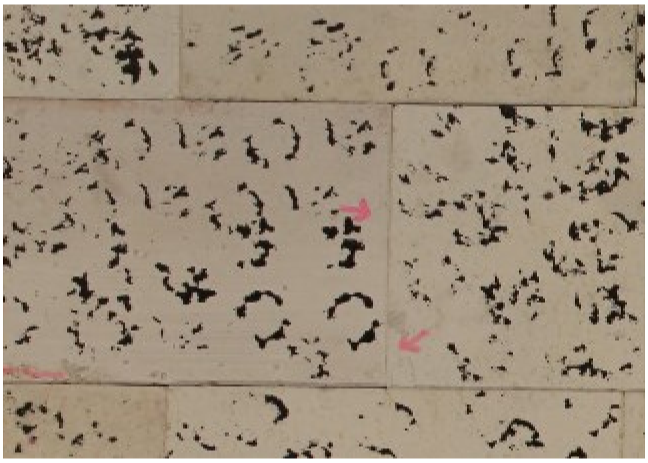

b)

c)

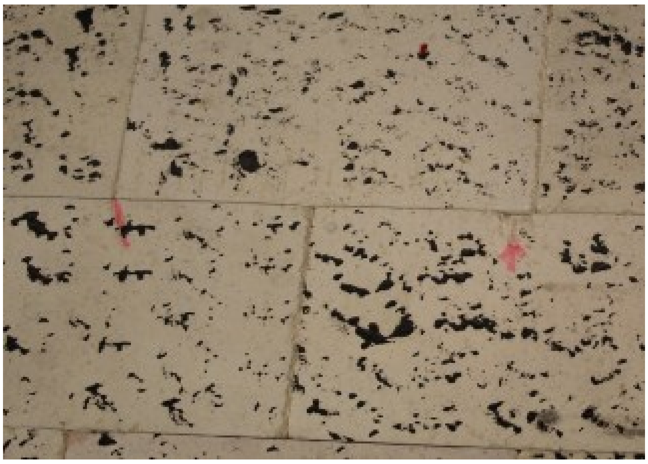

d)

**Figure 68 – Test series S07.AT.LHJ – Cracks observed in the specimen S07.AT.LHJ.01: a) cracks observed close to the head-joints, b) crushing of the bricks edges, c) crushing of the bricks edges and d) cracks observed close to the cross-joints.**

### 3.4.3 Test series S08.AT.LBI

Test series S08.AT.LBI aims to evaluate the mechanical behaviour of masonry wallets loaded in biaxial conditions at ambient temperature. The evolution of the in-plane displacements measured in the tests are presented in Figure 69. The LVDTs used to measure the in-plane displacements (WA-1 and WA-2 in the direction perpendicular to the head-joints, WA-3 and WA-4 in the direction perpendicular to the bed-joints) and the average of their values in each direction (WA-Avg-X and AW-Avg-Y corresponding respectively to the directions perpendicular to the bed-joints and head-joints) are presented. The measured forces and stresses during the test are presented in Figure 70 and Figure 71, respectively. It was possible to observe that the loading occurred simultaneously in both directions.

The stress-strain curves obtained in test series S08.AT.LBI are presented in Figure 72. The friction between the plungers and the specimen resulted in smaller strains and consequently an apparent higher stiffness in this test series. A small scattering of the results was observed. A sudden drop of stresses at the beginning of the unloading stage was previously discussed and it was also observed in this test series. The friction between the plungers and the wall is more significant in biaxial conditions. Therefore, smaller displacements were observed in the results of test series S08.AT.LBI. The compassion of the maximum and residual strains obtained in S06.AT.LBJ, S07.AT.LHJ and S08.AT.LBI is presented in

Table 4. A significant reduction in the strains were observed for direction X and Y, moreover, the reduction in the residual strains after the first loading cycling was also observed. Figure 73 presents a comparison of the stress-strain curves obtained at the biaxial tests at ambient temperature. The cracks observed in the specimen was similar to the ones already discussed in the previous sections. Figure 74 shows the cracks observed close to the bed-joints and the crushing in the edges of the bricks close to the head-joints.

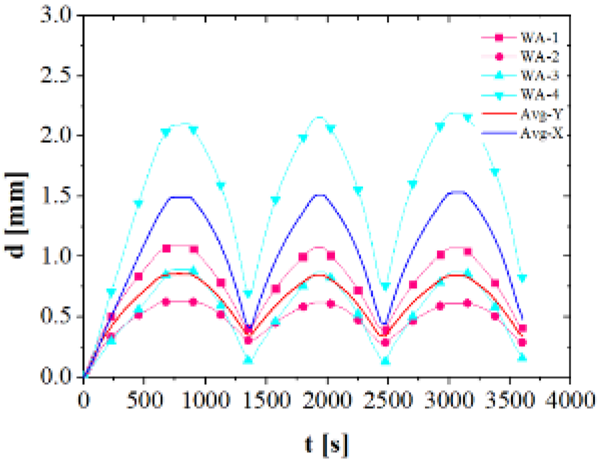


a)

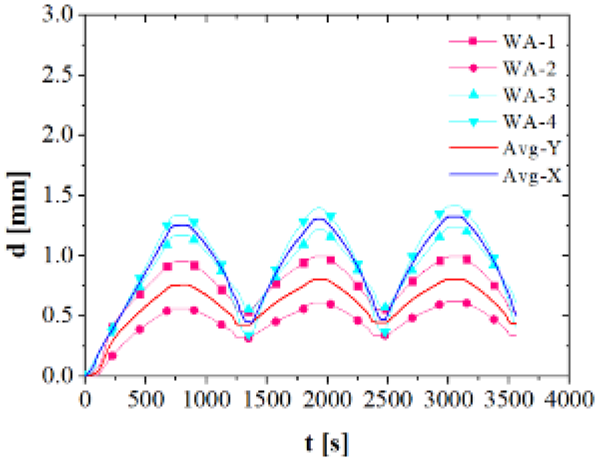


b)

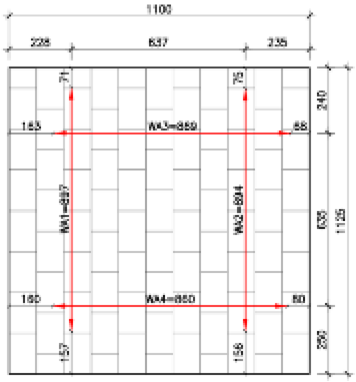


c)

**Figure 69 – Test series S08.AT.LBI – In-plane displacements in the direction perpendicular to the head-joints (WA-1 and WA-2), in the direction perpendicular to the bed-joints (WA-3 and WA-4): a) S08.AT.LBI.01, b) S08.AT.LBI.02 and c) LVDT locations.**

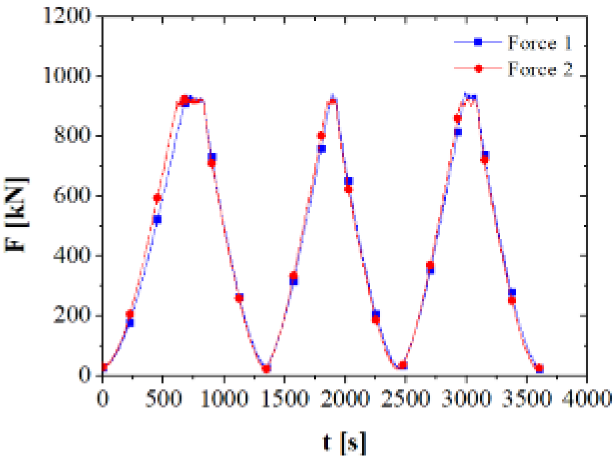


a)

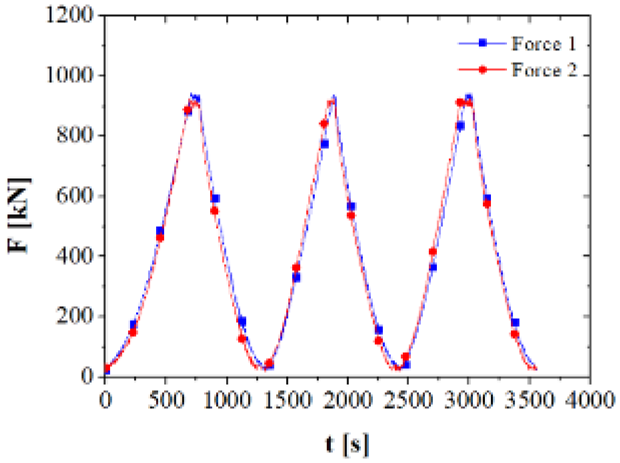


b)

Figure 70 – Test series S08.AT.LBI – Applied forces in the direction perpendicular to the bed-joints (Force 1) and perpendicular to the head-joints (Force 2): a) S08.AT.LBI.01 and b) S08.AT.LBI.02.

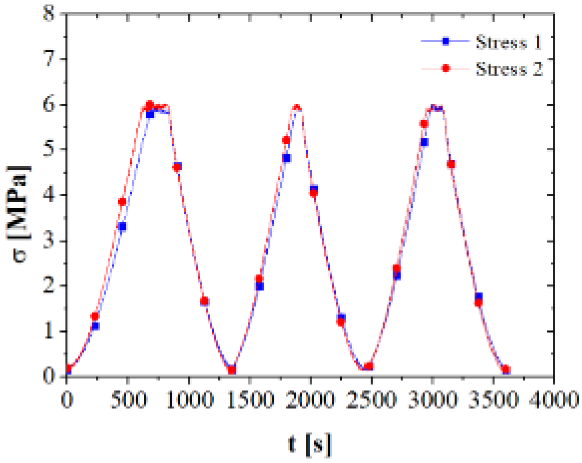


a)

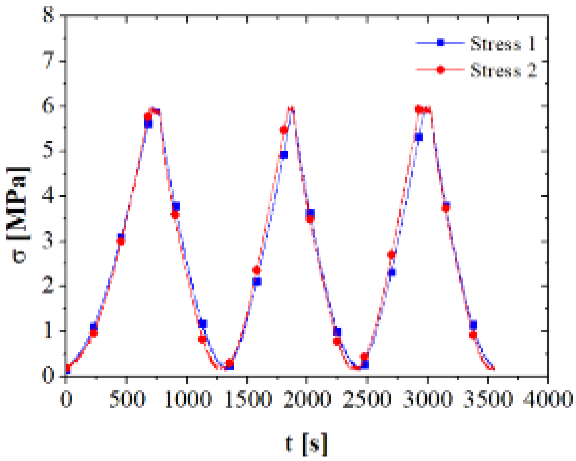


b)

Figure 71 – Test series S08.AT.LBI – Applied stresses in the direction perpendicular to the bed-joints (Stress 1) and perpendicular to the head-joints (Stress 2): a) S08.AT.LBI.01 and b) S08.AT.LBI.02.

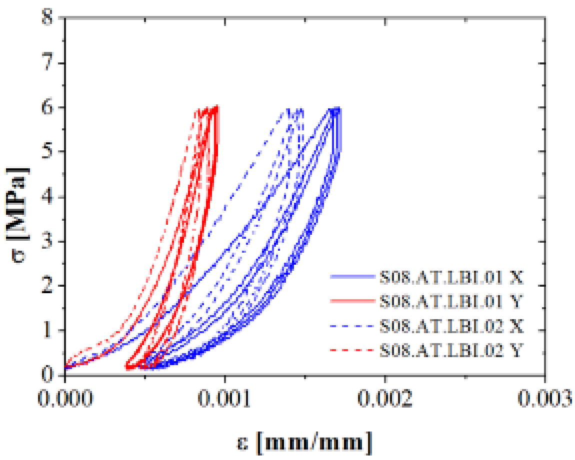


Figure 72 – Test series S08.AT.LBI – Stress-strain curves.

Table 4 – Comparison of the maximum and residual strains in test series S06.AT.LBJ, S07.AT.LHJ and S08.AT.LBI.

| *Test Series* | Specimen | $\varepsilon_{max}$ X | $\varepsilon_{max}$ Y | $\varepsilon_{res}$ X | $\varepsilon_{res}$ Y | $\varepsilon_{max,avg}$ X | $\varepsilon_{max,avg}$ Y | $\varepsilon_{res,avg}$ X | $\varepsilon_{res,avg}$ Y |
|---|---|---|---|---|---|---|---|---|---|
| *S06.AT.LBJ* | 01 | 0.0024 | - | 0.0015 | - | 0.0023 | - | 0.0014 | - |
| | 02 | 0.0022 | - | 0.0012 | - | | | | |
| *S07.AT.LHJ* | 01 | - | 0.0015 | - | 0.0010 | - | 0.0013 | - | 0.0008 |
| | 02 | - | 0.0010 | - | 0.0005 | | | | |
| *S08.AT.LBI* | 01 | 0.0016 | 0.0010 | 0.0005 | 0.0004 | 0.0015 (-34.7%) | 0.0009 (-30.7%) | 0.0005 (-64.3%) | 0.0005 (-37.5%) |
| | 02 | 0.0014 | 0.0008 | 0.0005 | 0.0005 | | | | |

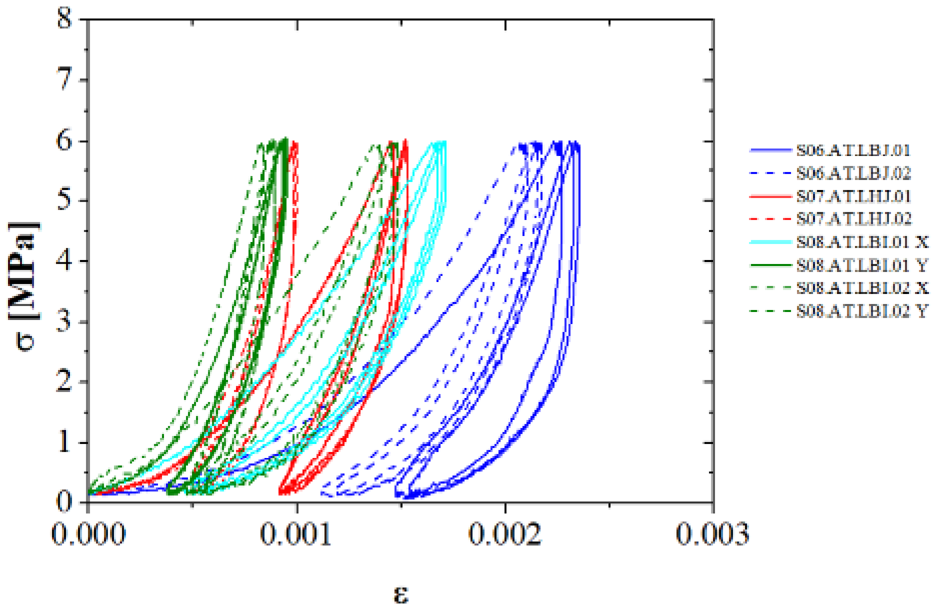


Figure 73 – Comparison of stress-strain curves obtained for test series S06.AT.LBJ, S07.AT.LHJ and S08.AT.LBI.

a)

b)

Figure 74 – Test series S08.AT.LBI – Cracks observed in the specimen: a) Cracks at cross joints and b) Crushing at head joint.

The full displacement fields in the (horizontal) direction perpendicular to the head-joints obtained using DIC of S05-02 at 25 %, 100 % of maximum load level and after unloading are presented in Figure 75. Again, it should be noted that all DIC results presented are turned 90º in the XY plane in comparison to Figure 69c presenting LVDT locations. The full displacement fields in the (vertical) direction perpendicular to the bed-joints, obtained using DIC of S05-02 at 25 %, 100 % of maximum load level and after unloading, are presented in Figure 76. The noise in the images is caused by the alumina tubes used to measure the displacements. Nonuniform vertical displacement field can be seen in Figure 75. A more uniform vertical displacement field can be seen in Figure 76. The negative signs in the colourmap are due to the coordinate system used in DIC analysis. Absolute values should be considered when comparing the two DIC figures with the force displacement diagrams or stress-strain diagrams.

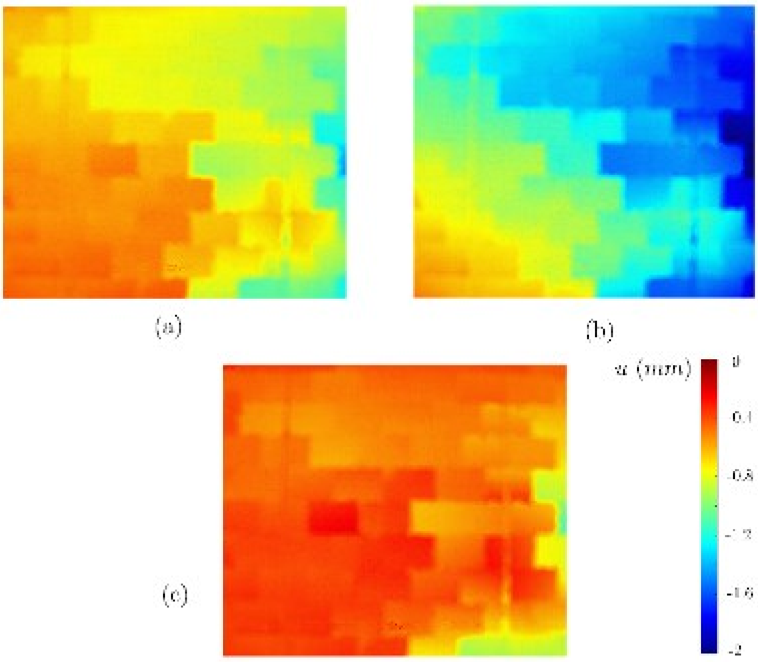


**Figure 75-Displacement fields in the direction perpendicular to head joints (horizontal direction in this picture) in specimen S08.AT.LBI.01 at: (a) 25 %, (b) 100 % of maximum load level and (c) after unloading.**

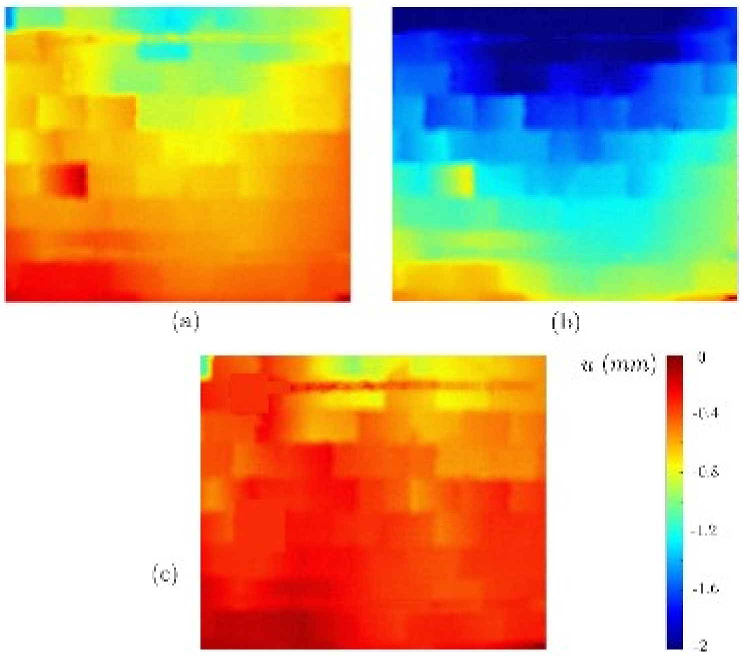


**Figure 76-Displacement fields in the direction perpendicular to bed joints (vertical direction in this picture) in specimen S08.AT.LBI.01 at: (a) 25 %, (b) 100 % of maximum load level and (c) after unloading.**

### 3.4.4 Preliminary test at 1200 ºC

A preliminary test was performed to calibrate the heating system of the machine. In this test, several changes were performed in the electrical connections: secondary voltage of the transformer and connections configuration (star and delta). This first test did not reach the desired temperature (1500 ºC), as the heating system did not have the required power, it was only possible to achieve 1200 ºC. The heating system was improved for the other tests. The results of this preliminary test at 1200 ºC is nevertheless given in this section. The temperatures measured by the thermocouples embedded in the bricks are presented in Figure 77. The temperatures recorded at the beginning of the test were around 180 ºC because the furnaces was previously turned on for testing. The temperature of the furnaces was not recorded for this test.

This preliminary test was performed as a uniaxial creep test in the direction perpendicular to the bed joints. The evolution of the in-plane displacements and strains are presented in Figure 78. The LVDTs used to measure the in-plane displacements (WA-2 and WA-3) in the direction perpendicular to bed-joints and the average of their values (WA-Avg) are presented. It should be noted that the LVDT WA-4 (supposed to measure in the same direction) did not work properly during this test and it was therefore ignored. A small scattering was observed between the measurements of LVDTs WA-2 and WA-3. The identification of the creep strains was straightforward during the holding stage (between 0.30 and 1.25 h).

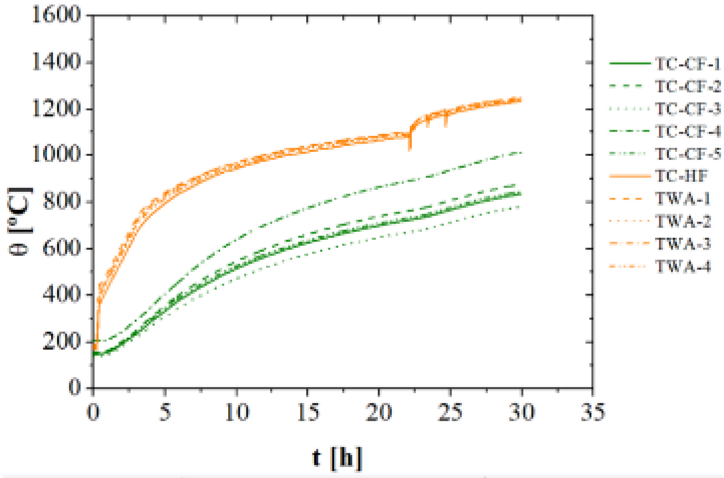


a)

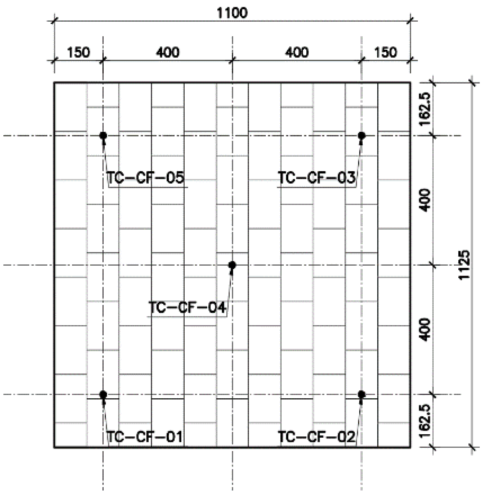


b)

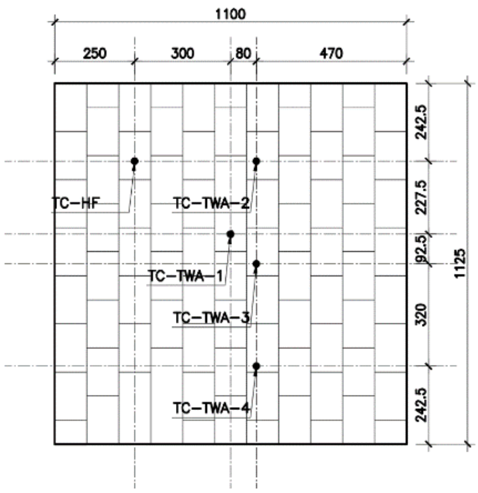


c)

**Figure 77 – Preliminary test: a) Temperatures, b) Thermocouples of the cold face and c) Thermocouples of the hot face.**

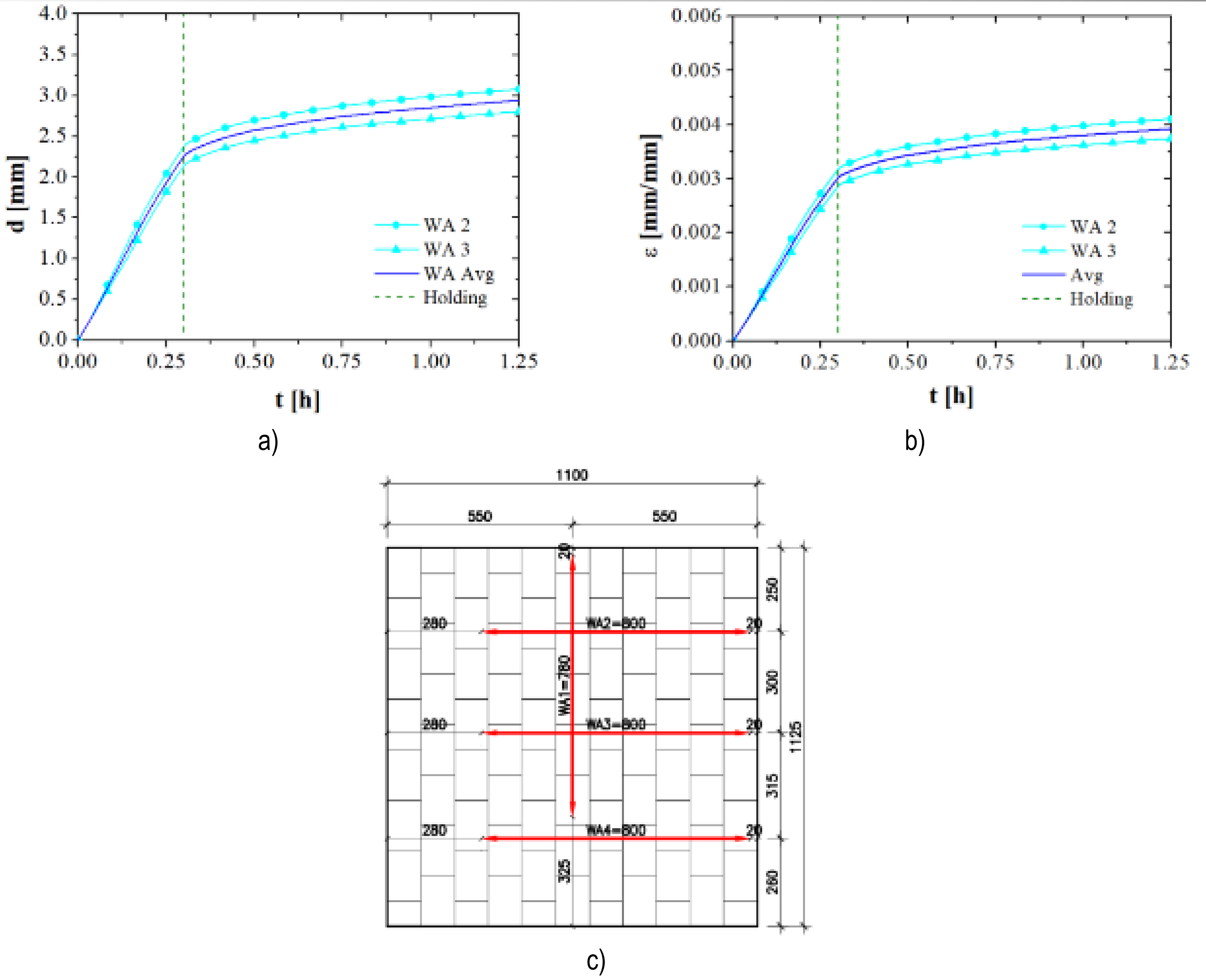


**Figure 78 – Preliminary test: a) In-plane displacements, b) Strains and c) LVDT locations.**

The measured forces and stresses during the test are shown in Figure 79. The lateral restraint provided by the blocked plunger induces a reaction force in the direction perpendicular to the head-joints. The maximum reaction force was 67.2 kN (0.44 MPa). This value is smaller than the reaction forces obtained in test series S06.AT.LBJ (103.6 kN and 101.3 kN), as the elevated temperature reduces the stiffness of the specimen and the creep could also reduce the reaction force. The stress-strain curves obtained in this preliminary test is presented in Figure 80. During the loading stage, the average strain is 0.0030, which comprises of the elastic strain in the bricks, the strains due to crack closure and crushing of initial non-plane surfaces, as well as creep strain. This strain is 25 % higher than the average obtained in test series S06.AT.LBJ ($\varepsilon = 0.0024$). During the holding stage, the total strain increases from 0.0030 to 0.0038, mostly caused by creep.

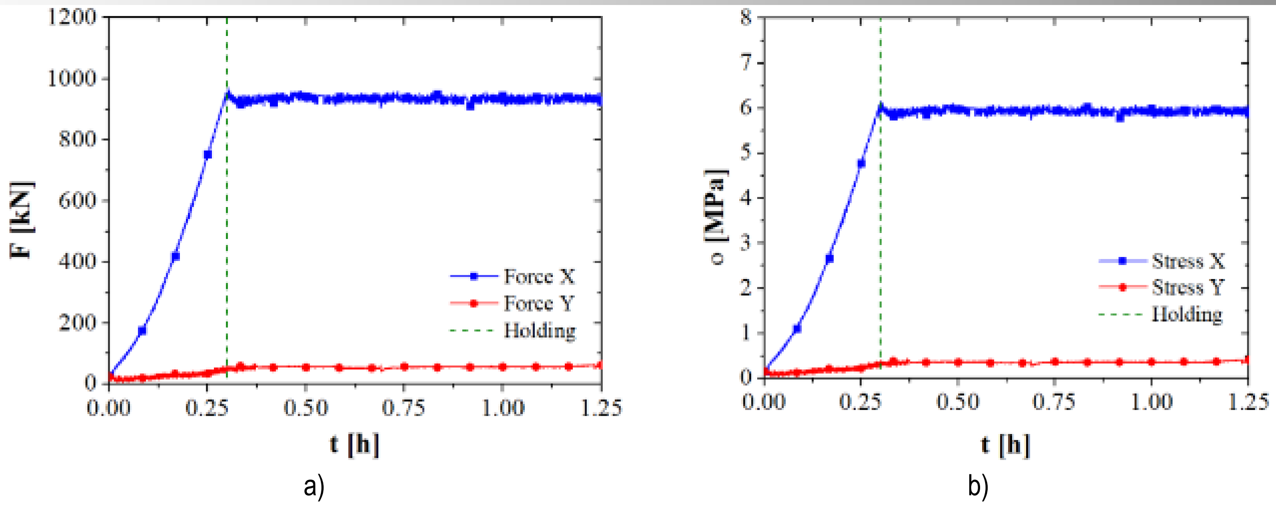


**Figure 79 – Preliminary test: a) Forces and b) Stresses in the X and Y directions, corresponding respectively to the direction perpendicular to the bed-joints and the direction perpendicular to the head-joints.**

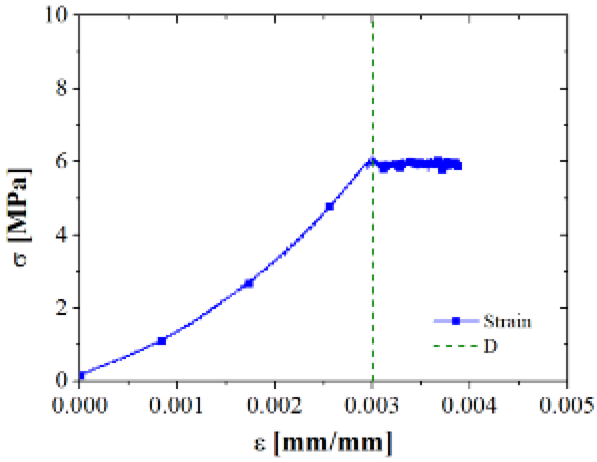


**Figure 80 – Preliminary test: Stress-strain curves in the direction perpendicular to the bed-joints.**

### 3.4.5 Test series S09.HT.CBJ

The previous tests (S06.AT.LBJ, S07.AT.LHJ and S08.AT.LBI) have evaluated the structural response of refractory masonry under diversified loading conditions at room temperature. This test series, S09.HT.CBJ, aims to characterize the behaviour of refractory masonry uniaxially loaded at high temperature. The temperatures measured by the thermocouples embedded in the bricks are presented in Figure 81. The curves presented in red are the target heating and the temperature measured in the furnace. Due to the high thermal capacitance of the test system (specimen and furnace), the furnace was not able to follow the programmed curve. The temperatures in the hot face started to increase rapidly when the thermal load was applied. Due to the relatively low thermal conductivity of refractory materials, the temperatures on the cold face took some time to start increasing. The temperatures in the thermocouples of the hot face (TWA-1 to TWA-4 and TC-HF) were directly exposed to the furnace radiation. Therefore, the thermocouples measuring at this face are in good agreement with the furnace temperature. The temperatures in the thermocouples installed in the middle of the cold face (TC-CF-4) is slightly higher than the other thermocouples of the cold face due to heat loses in the edges of the specimen.

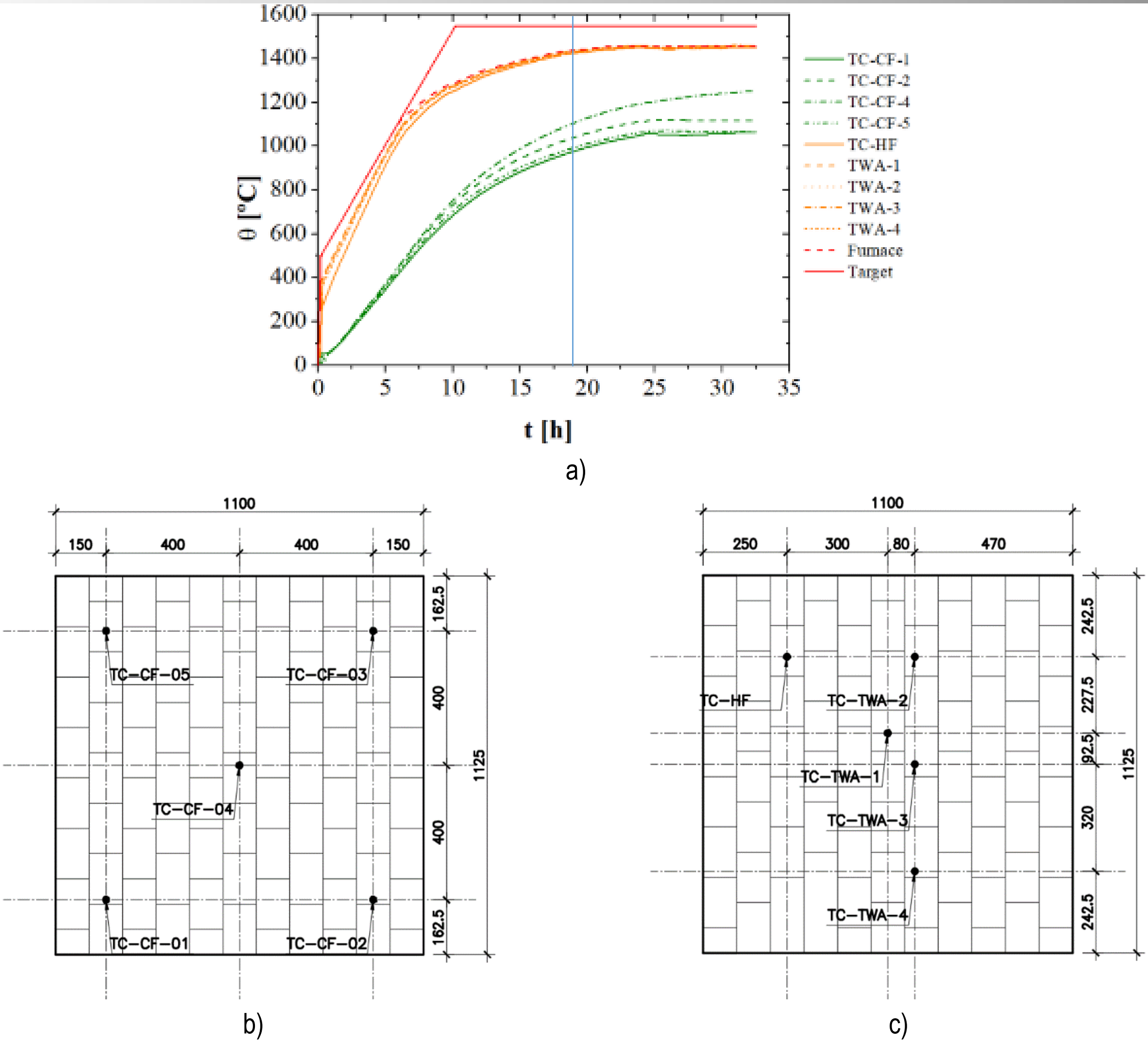


**Figure 81 – Test series S09.HT.CBJ : a) Temperatures, b) Thermocouples of the cold face and c) Thermocouples of the hot face.**

The evolution of the in-plane displacements and strains of specimen S09.HT.CBJ.01 and S09.HT.CBJ.02 are presented in Figure 82 and Figure 83. For specimen S09.HT.CBJ.01, three LVDTs were used to measure the in-plane displacement in the direction perpendicular to the bed-joints (WA-2, WA-3 and WA-4) while, two LVDTs (WA-2 and WA-4) were used in the case of specimen S09.HT.CBJ.02 (since WA-3 was not functional). The values of measured displacement of the LVDTs, and their average (WA-Avg) are presented in Figure 82 and Figure 83.

The measured forces and stresses during the tests are shown in Figure 84. During load holding step, the reduction and increase in the forces are caused by some problems in the controller of the hydraulic jack. Nevertheless, this noise did not greatly impact the test. The lateral restraint provided by the blocked plunger induces a reaction force in the direction perpendicular to the head-joints. The maximum reaction force (force Y) was around 62.1 kN (0.4 MPa) for specimens S09.HT.CBJ.01 and S09.HT.CBJ.02. These values are smaller than the reaction forces obtained in test series S06.AT.LBJ (103.6 kN and 101.3 kN), as the elevated temperature reduces the stiffness of the specimen and the creep could also reduce the reaction force. During the holding step, these values (force Y) decreased due to the relaxation behaviour in the direction perpendicular to the head-joints (locked positions of the plungers in contact with the sides of the wall).

The stress-strain curves obtained in test series S09.HT.CBJ are presented in Figure 85. The behaviour of specimens S09.HT.CBJ.01 and S09.HT.CBJ.02 are compared in Figure 86. By the end of the loading stage the average strains are around 0.005 and 0.006 for specimens S09.HT.CBJ.01 and S09.HT.CBJ.02, respectively. Sixteen hours after the beginning of the holding stage, the measured strains are 0.015 and 0.016 for specimens S09.HT.CBJ.01 and S09.HT.CBJ.02, respectively. Analysing the strain evolutions for both specimens, it is possible to observe the primary and secondary creep stages in the specimen. The average strain by the end of load application step was 0.015. This value is significantly higher than the maximum strain obtained in test series S06.AT.LBJ ($\varepsilon$ = 0.0024) and in the preliminary test at 1200 ºC ($\varepsilon$ = 0.0030), as the creep rate is higher for the temperature range of test S09.

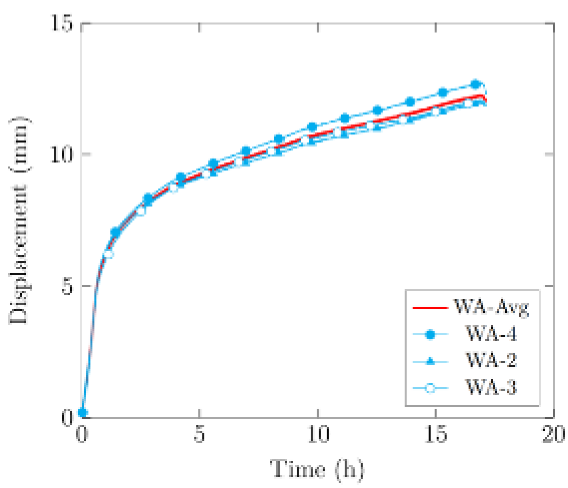


a)

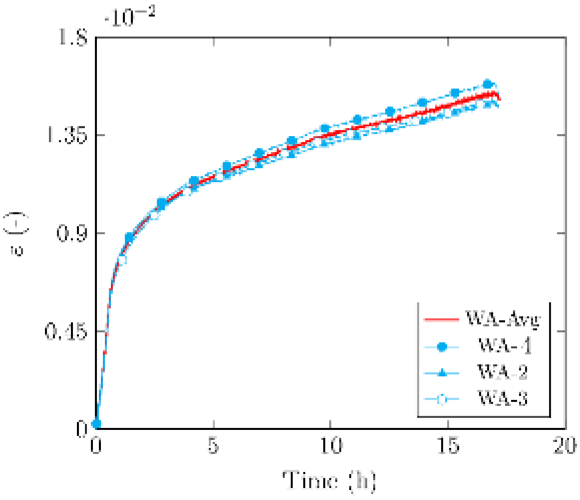


b)

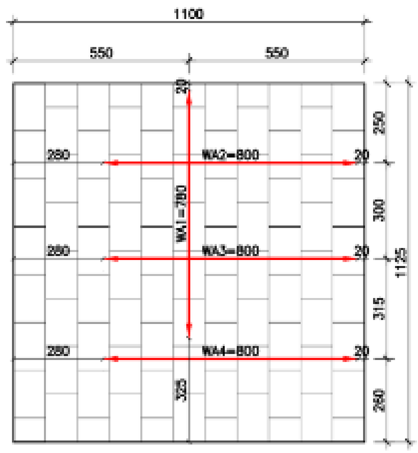


c)

**Figure 82 – Test series S09.HT.CBJ.01: a) In-plane displacements, b) Strains and c) LVDT locations.**

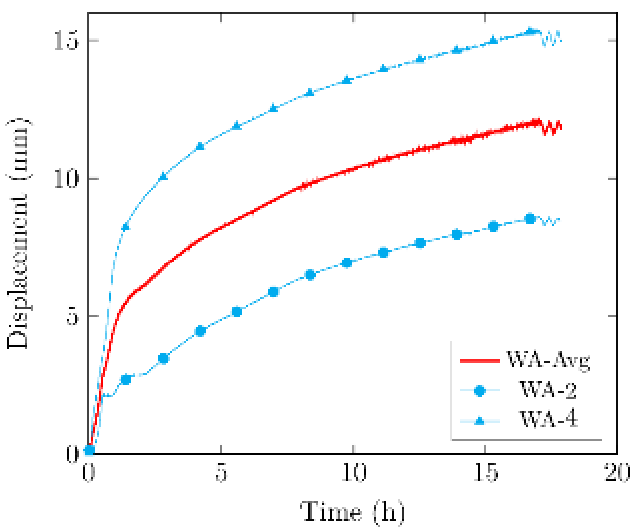


a)

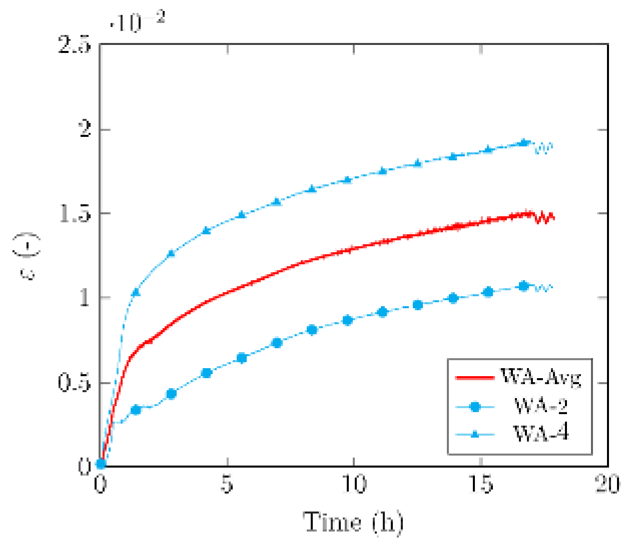


b)

**Figure 83 – Test series S09.HT.CBJ.02: a) In-plane displacements and b) Strains perpendicular to the bed-joints.**

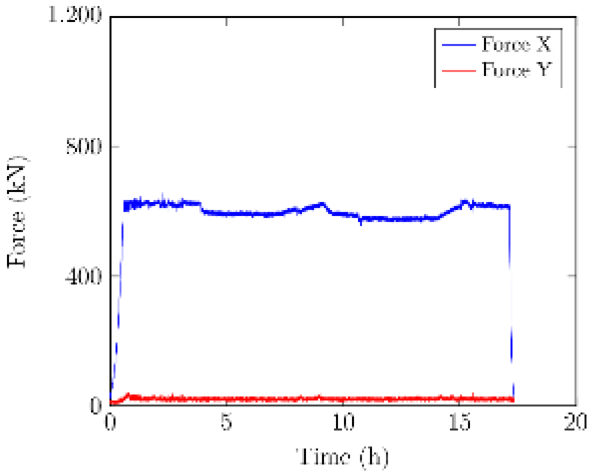


a)

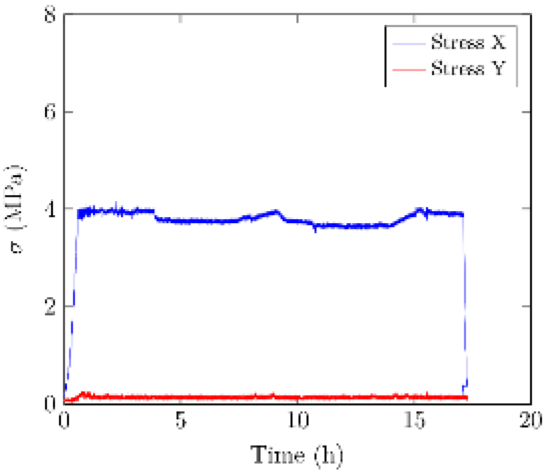


b)

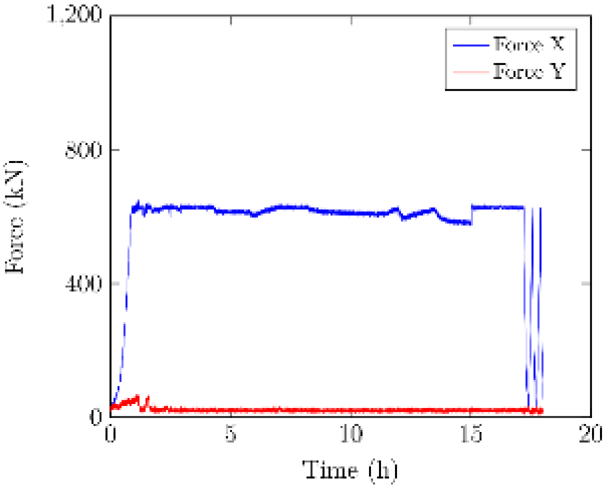


c)

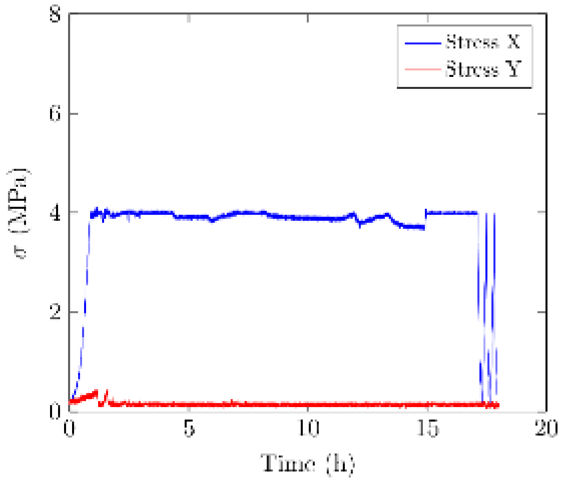


d)

**Figure 84 – Test series S09.HT.CBJ – a) Forces S09.HT.CBJ.01, b) Stresses S09.HT.CBJ.02, c) Forces S09.HT.CBJ.02 and d) Stresses S09.HT.CBJ.02 in the X and Y directions, corresponding respectively to the direction perpendicular to the bed-joints and the direction perpendicular to the head-joints.**



European Commission
Horizon 2020
European Union funding
for Research & Innovation

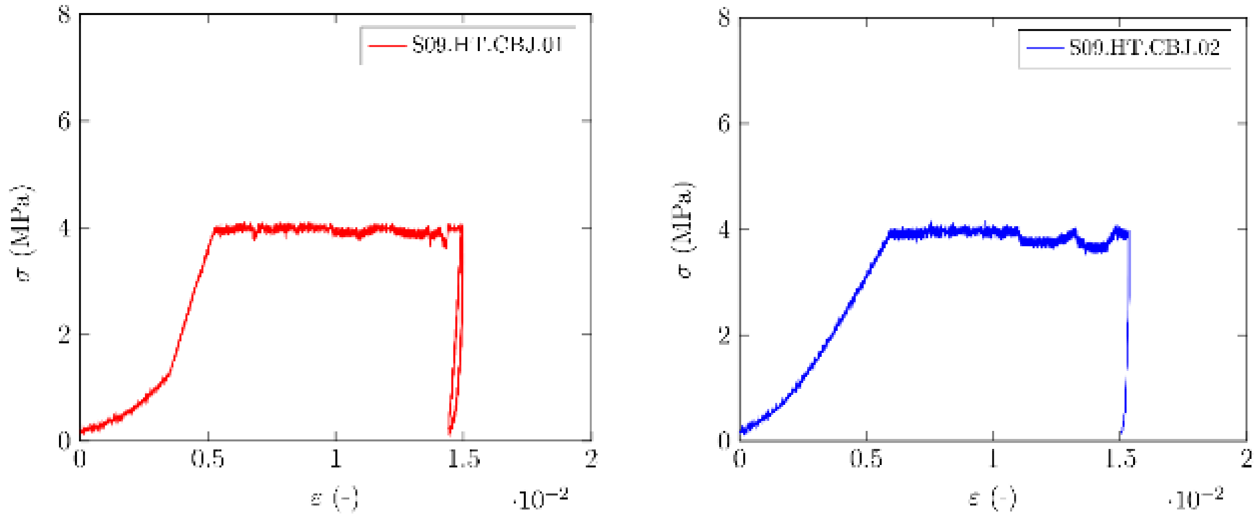


a) b)

**Figure 85 – Test series S09.HT.CBJ – Stress-strain curves: a) S09.HT.CBJ.01 and b) S09.HT.CBJ.02 in the direction perpendicular to the bed-joints.**

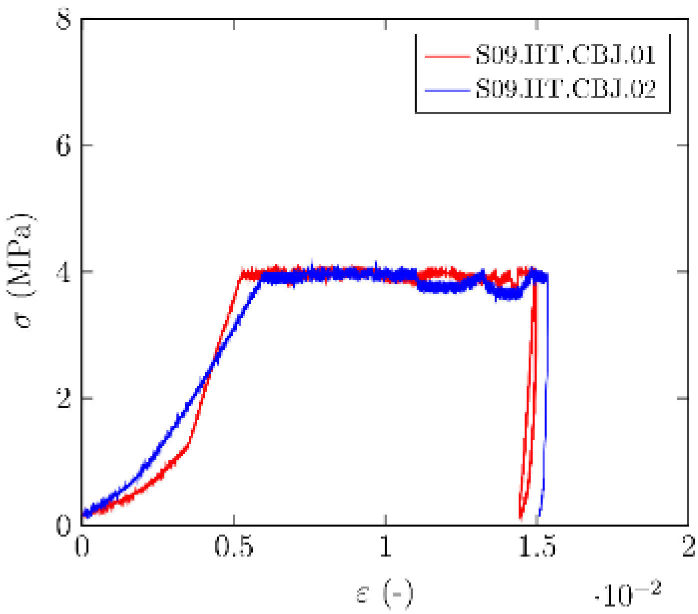


**Figure 86 – Test series S09.HT.CBJ – Comparison of the stress-strain curves in the direction perpendicular to the bed-joints**

The cracks close to the cross joints, caused by the bricks' height imperfections, presented in the previous test series, were also observed in this test series. At high temperatures (1480 ºC at the hot face), the creep effects are dominant. Therefore, the part of the brick subjected to higher compressive stresses presented higher creep strains, as observed in Figure 87. The difference in the bricks dimensions after the test, and the crack in the middle of the brick, indicate that the left part of the brick experienced a higher creep strain. The temperature curve defined for the heating of the specimens was relatively high. Industrial linings are usually heated up for a heating rate from 25 ºC/h to 50 ºC/h. As discussed previously (Section 3.3), the curve used in these tests comprised of heating from ambient temperature to 500 ºC in 10 minutes, due to limitations in the experimental setup. After the initial slope, a heating rate of 150 ºC/h was used between 500 ºC and 1550 ºC. Some cracks were observed in the same plane as the hot face of the brick, at a depth of 50 mm, as shown in Figure 88. These cracks were most likely caused by the high heating rate used. The rockwool used for insulation melted during the test. The molten material made contact with the specimen and some corrosion was identified caused by the reaction between the alumina spinel brick and the rockwool, as shown in Figure 89. Nevertheless, only surface damage was observed. Again, due to the chamfers in the plungers, failure was observed in the corner unit, as shown in Figure 90.



European Commission
Horizon 2020
European Union funding
for Research & Innovation

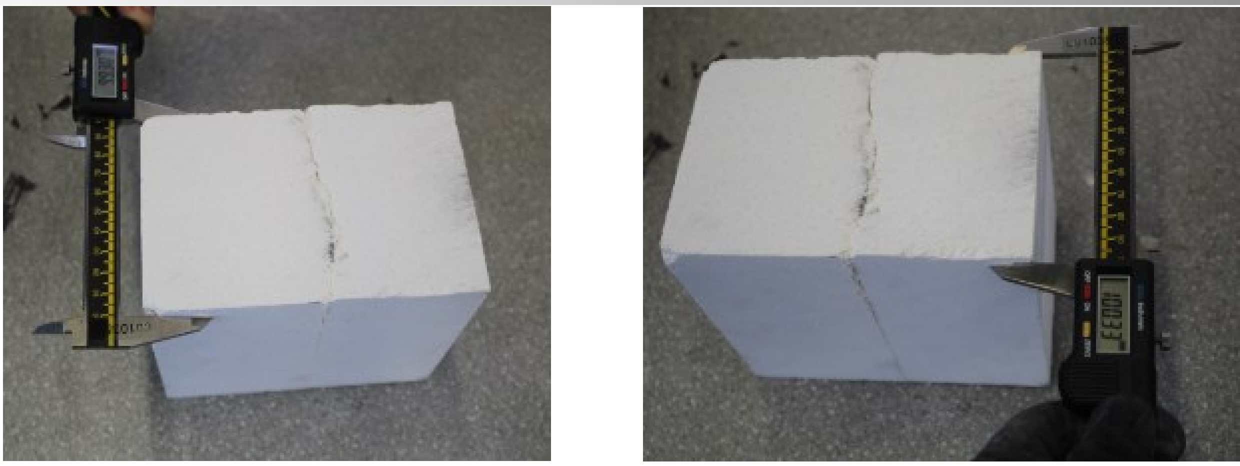

a) b)

Figure 87 – Test series S09.HT.CBJ – Different creep strains due to brick's height imperfections.

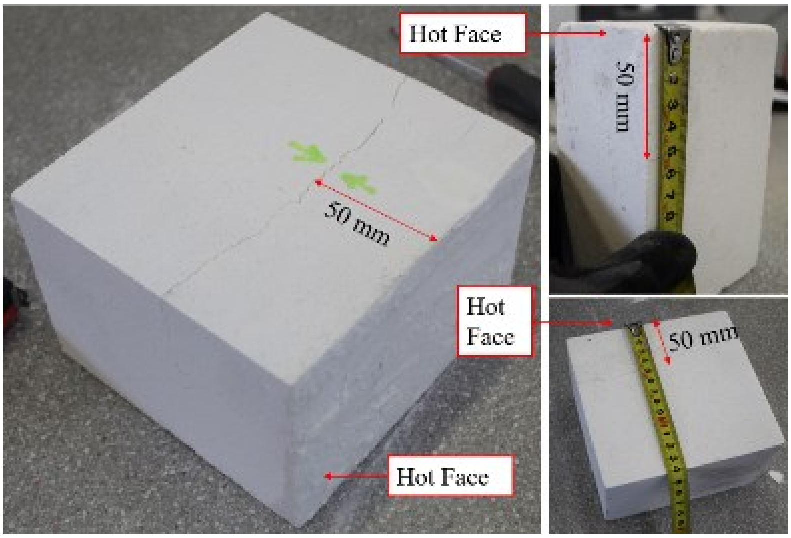


Figure 88 – Test series S09.HT.CBJ – Cracks 50 mm away from the hot face.

Figure 89 – Test series S09.HT.CBJ – Reaction between alumina-spinel bricks and rockwool insulation.

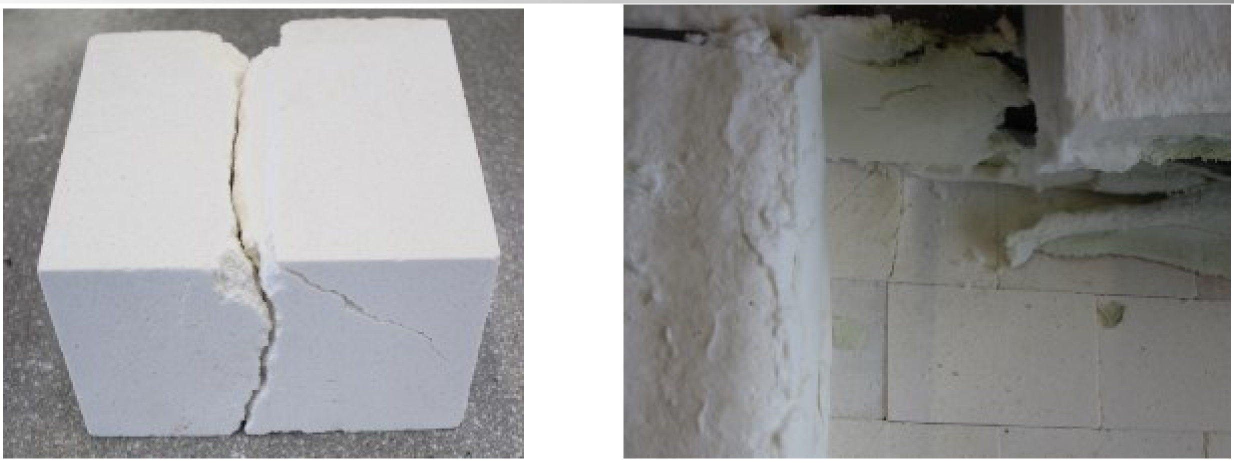

a) b)

**Figure 90 – Test series S09.HT.CBJ – Failure at the brick adjacent to the plunger chamfers:**
**a) details of the failure and b) Location of the brick.**

### 3.4.6 Test series S10.HT.CBI

The previous test series S09.HT.CBJ aimed to evaluate the response of refractory masonry uniaxially loaded at high temperature. This test series, S10.HT.CBI, aims to assess their structural response under biaxial loading. The temperatures measured by the thermocouples embedded in the bricks are presented in Figure 91. The curves presented in red are the target heating and the temperature measured in the furnace. The average temperatures recorded at the hot face during the test was 1482 ºC. A small variation was observed in the hot face due to heat loses caused by the movement of the plungers, nevertheless it was not significant. The thermocouple of the cold face TC-CF-4 was in the middle of the specimen, therefore, it was less prone to heat loses, when compared to the thermocouples of the edge of the wall. The temperature recorded by the thermocouple TC-CF-4 was 1266 ºC at the beginning of the test and increased to 1299 ºC by the end of the test. The average temperature of TC-CF-1, TC-CF-2 and TC-CF-5 was 1123 ºC during the mechanical phase of the test.

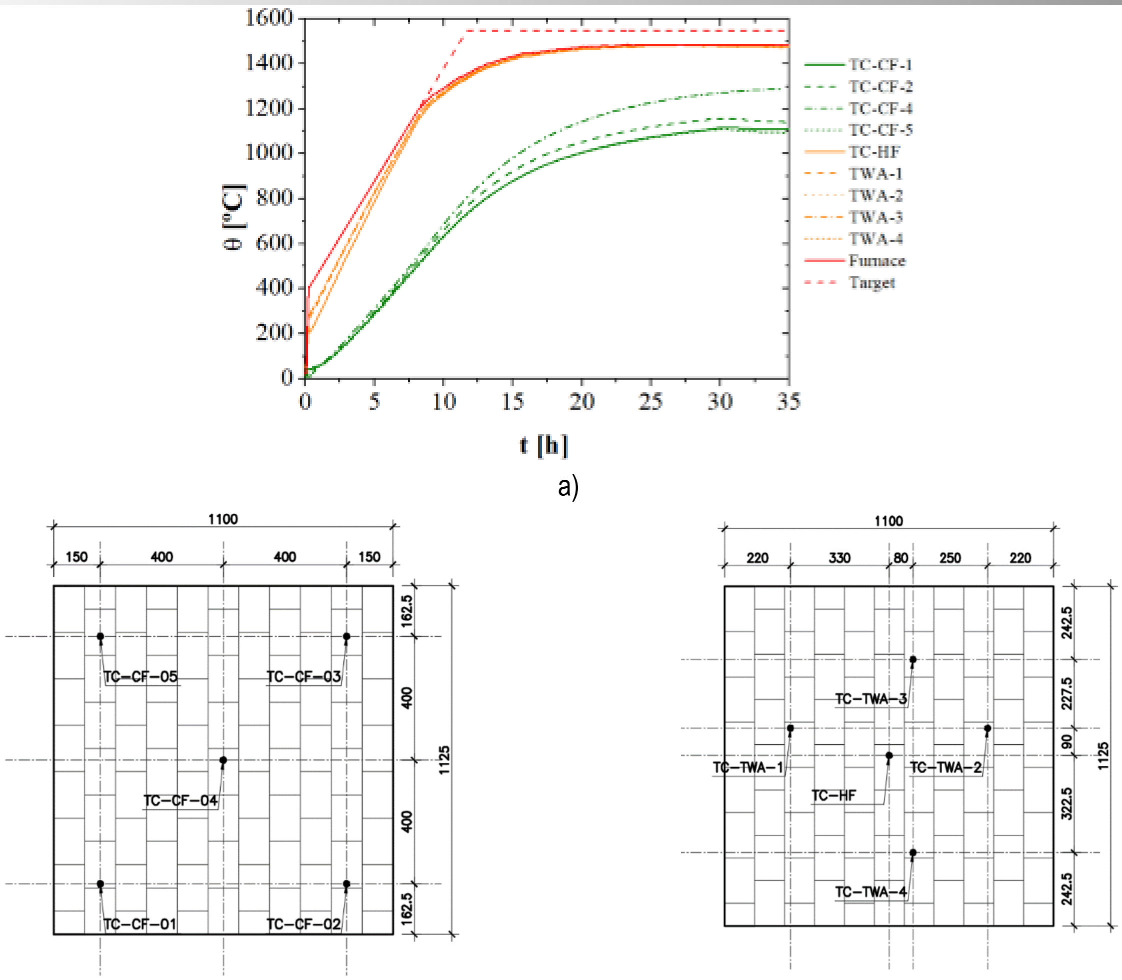


a)

b) c)

**Figure 91 – Test series S10.HT.CBI: a) Temperatures, b) Thermocouples of the cold face and c) Thermocouples of the hot face.**

The evolution of the in-plane displacements and strains are presented in Figure 92. The LVDTs used to measure the in-plane displacements in direction Y, perpendicular to the head-joints, (WA-1 and WA-2) and direction X, perpendicular to the bed-joints, (WA-3 and WA-4) and the average of their values in each direction (Avg-X and Avg-Y) are shown. The measured forces and stresses during the test are presented in Figure 93. Some drops in the forces recorded in the X direction were observed, this was caused by a problem in the jack controller. Nevertheless, the noise did not affect the results of the test. The stress-strain curves obtained in test series S10.HT.CBI are presented in Figure 94. During the loading stage the average strain was 0.0044 and 0.0032 in the X and Y direction, respectively. The measured strain comprises of the elastic strain in the bricks, the strains due to crack closure and crushing of the initial non-plane surfaces, as well as creep strain. During the holding stage, the total strain increased to 0.0066 and 0.0053 in the X and Y direction, respectively. The increasing in the strains was mostly caused by creep, as discussed in S09.HT.CBJ.

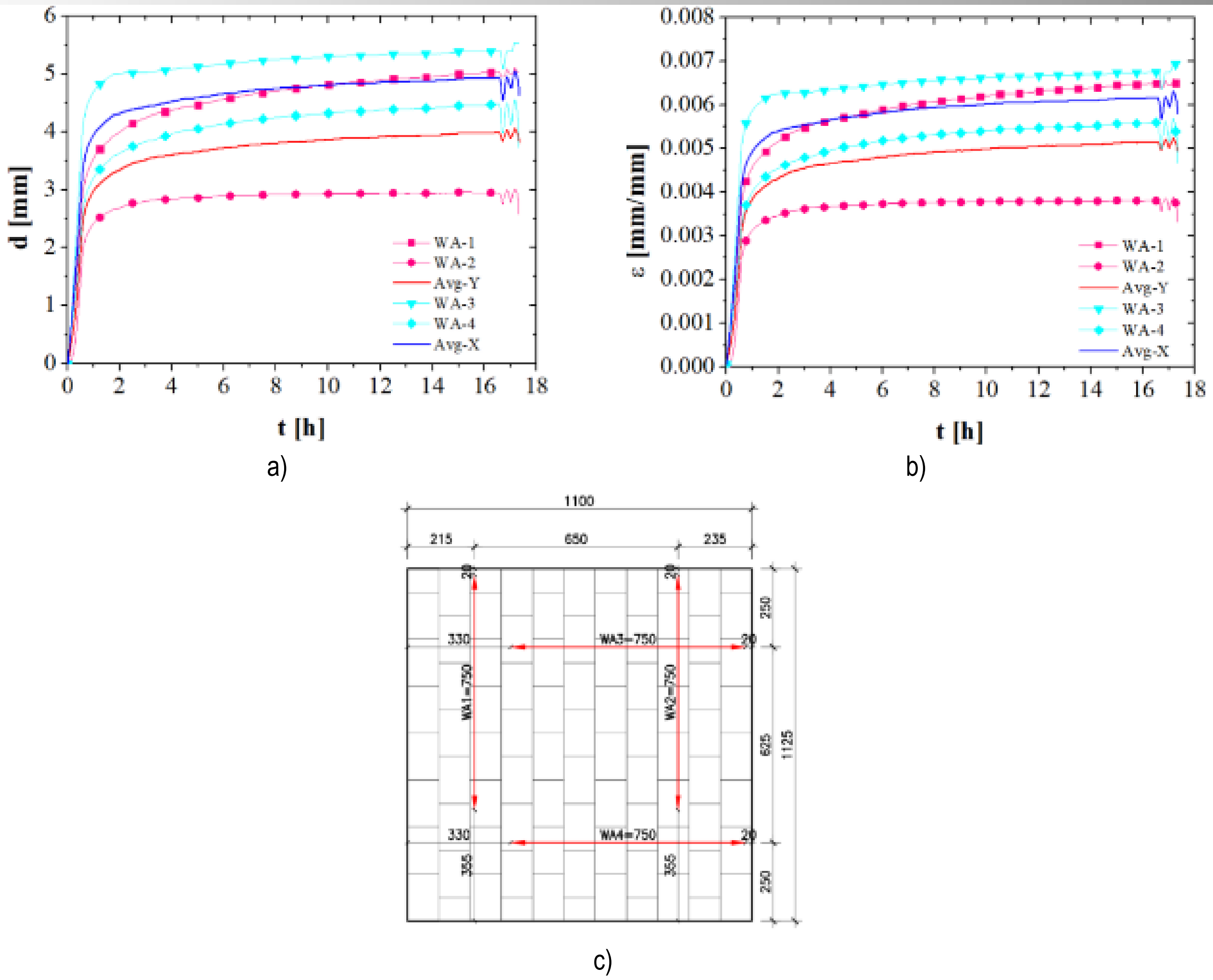


**Figure 92 – Test specimen S10.HT.CBI.01 – a) In-plane displacements, b) Strains and c) LVDT locations (the X and Y directions, correspond respectively to the direction perpendicular to the bed-joints and the direction perpendicular to the head-joints).**

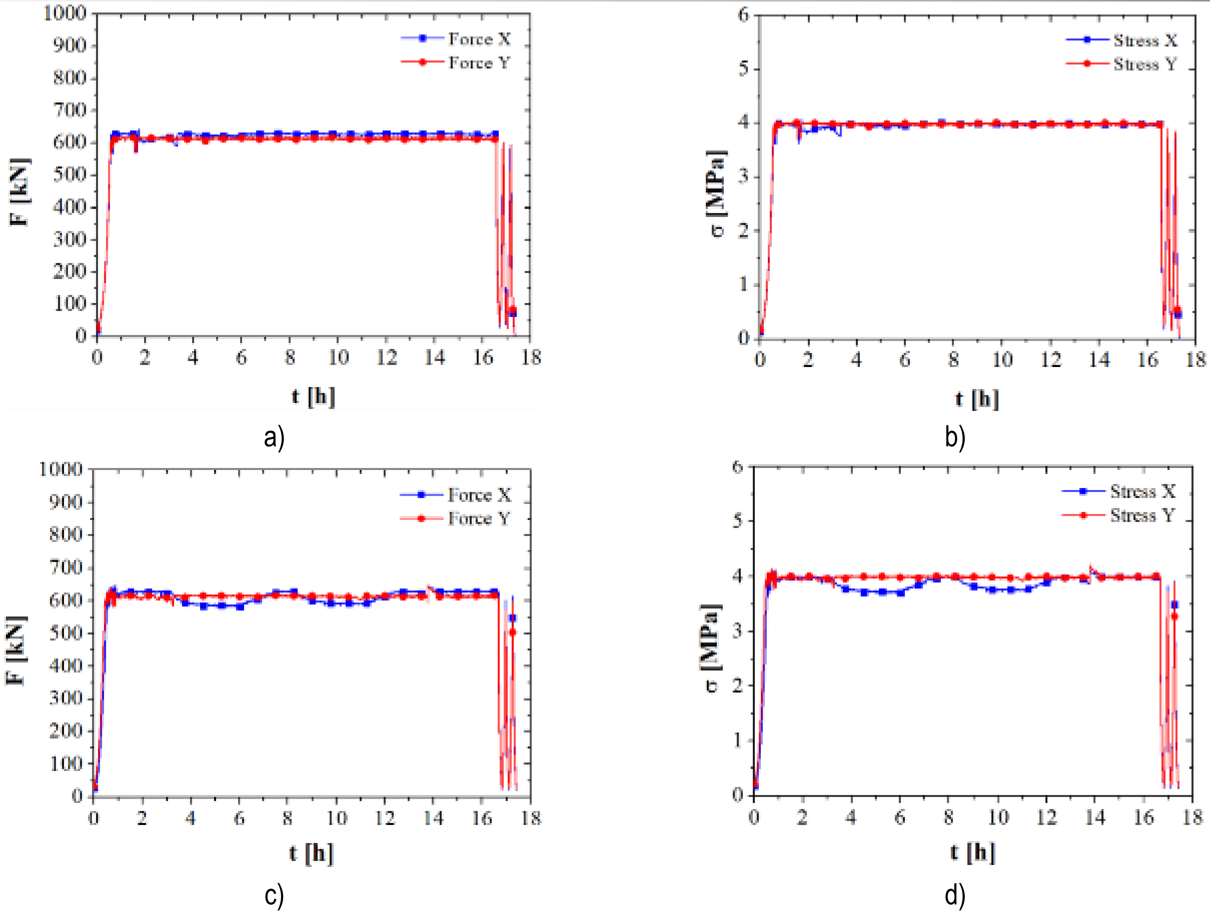


**Figure 93 – Test series S10.HT.CBI:**
**a) Forces S10.HT.CBI.01, b) Stresses S10.HT.CBI.01, c) Forces S10.HT.CBI.02 and d) Stresses S10.HT.CBI.02 (the X and Y directions, correspond respectively to the direction perpendicular to the bed-joints and the direction perpendicular to the head-joints).**

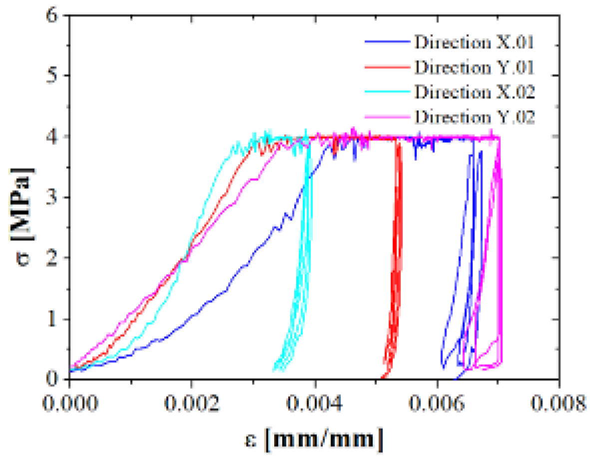


**Figure 94 – Test series S10.HT.CBI – Stress-strain curves (the X and Y directions, correspond respectively to the direction perpendicular to the bed-joints and the direction perpendicular to the head-joints).**

The typical cracks, observed in the middle of the bricks presented in the previous test series, were also observed. At high temperature, this crack was associated to large creep strains, as shown in Figure 95. The difference in the brick dimensions after the tests, and the crack in the middle of the brick, indicate that the right part of the brick experienced a higher creep strain. As noted in test series S07.AT.LHJ and S08.AT.LBI, some crushing areas were observed close to the head joints (Figure 96a). Several bricks were stuck together at the head joints, as shown in Figure 96b. As observed in test series S09.HT.CBJ, the corner brick also failed due to the chamfers in the plungers. The reaction between the rockwool used for insulating and the alumina spinel brick was ever more significant in this test. The molten insulation was in contact with the specimen and some pits of corrosion were observed in the surface of the specimens, as shown in Figure 97. However, it did not affect the thermomechanical behaviour of the overall sample.

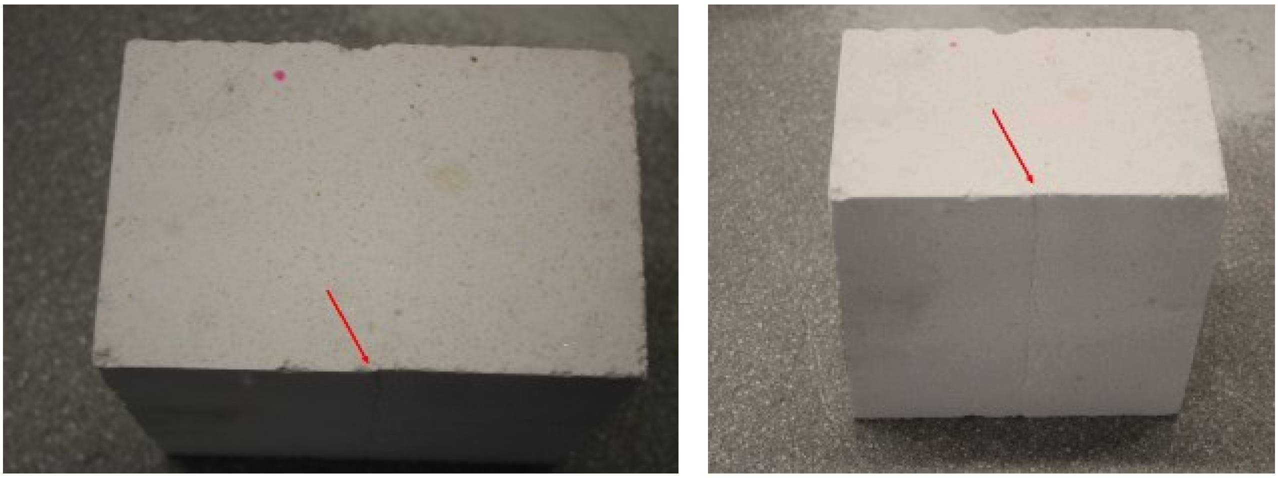

a) b)

**Figure 95 – Test series S10.HT.CBI – Different creep strains due to the bricks height imperfections: a) upper view and b) front view.**

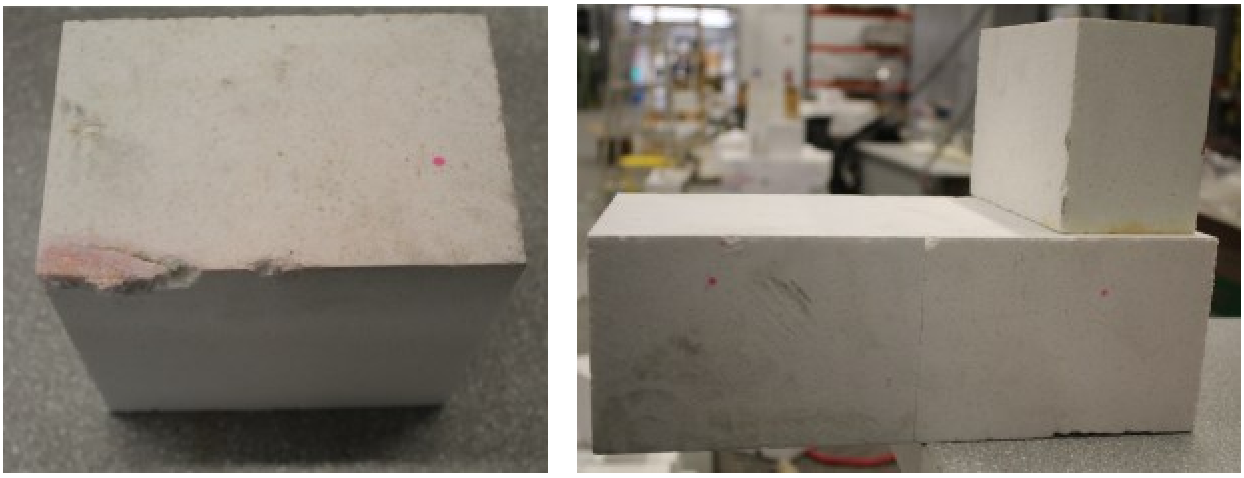

a) b)

**Figure 96 – Test series S10.HT.CBI: Failure at the head joint: a) Crushing and b) Bricks stuck together.**

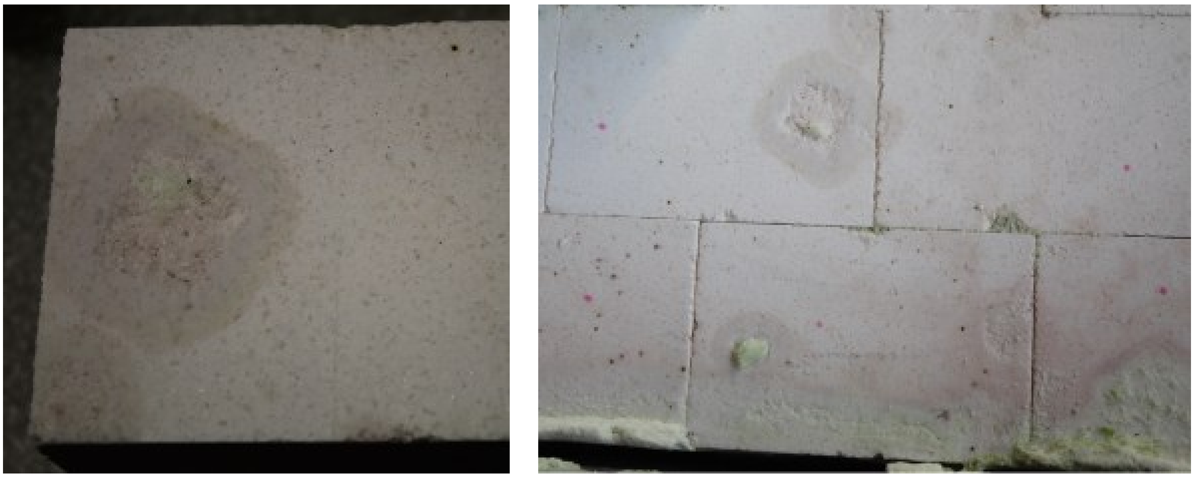

a) b)

**Figure 97 – Test series S10.HT.CBI: Reaction between alumina-spinel bricks and rockwool insulation: a) and b).**

### 3.4.7 Test series S11.HT.RBI

Test series S11.HT.RBI aims to characterize the wallets under biaxial relaxation. The typical temperature evolution obtained for test series S11.HT.RBI is given in Figure 98. The temperatures measured in the hot face were around 1460 ºC during the relaxation test. The centre of the cold face was around 1300 ºC. Due to the heat loses in the edges of the specimen, the thermocouples of at the edges of the cold face measured temperatures around 1150 ºC.

The displacements and strains measured for the specimen S11.HT.RBI.01 are presented in Figure 99. The measurements of the LVDTs confirmed that no significant displacements happened during the relaxation stage. The location of the LVDTs is given in Figure 99c. The evolution of forces and stresses measured during the relaxation tests are given in Figure 100. When the controller of the hydraulic jacks lock their positions the relaxation process starts. The forces (and stresses) measured in the specimens drop significantly, for example, the forces in specimen S11.HT.RBI.01 decrease from 505.2 kN (direction X) and 597.2 (direction Y) to 286.0 kN and 337.1 kN, respectively, in 30 minutes. Again, the X and Y directions, correspond respectively to the direction perpendicular to the bed-joints and the direction perpendicular to the head-joints. After one hour, the forces reach 240.6 kN and 272.4 kN. The rate of forces relief decreases during the relaxation process. Unfortunately, it was not possible to keep the same test procedure for the second stage of the test due to restrictions imposed by the Austrian authorities when the S11.HT.RBI.02 test was performed. As a consequence for this second test, the first holding time after the initial load application step was longer than that of the first test and the second holding time was shorter than that of the first test. Figure 101a presents the comparison of the force evolution in specimens S11.HT.RBI.02 and S11.HT.RBI.02, for the first 6.5 hours, and a small scattering was observed. The stress-strain curves are presented in Figure 101b.

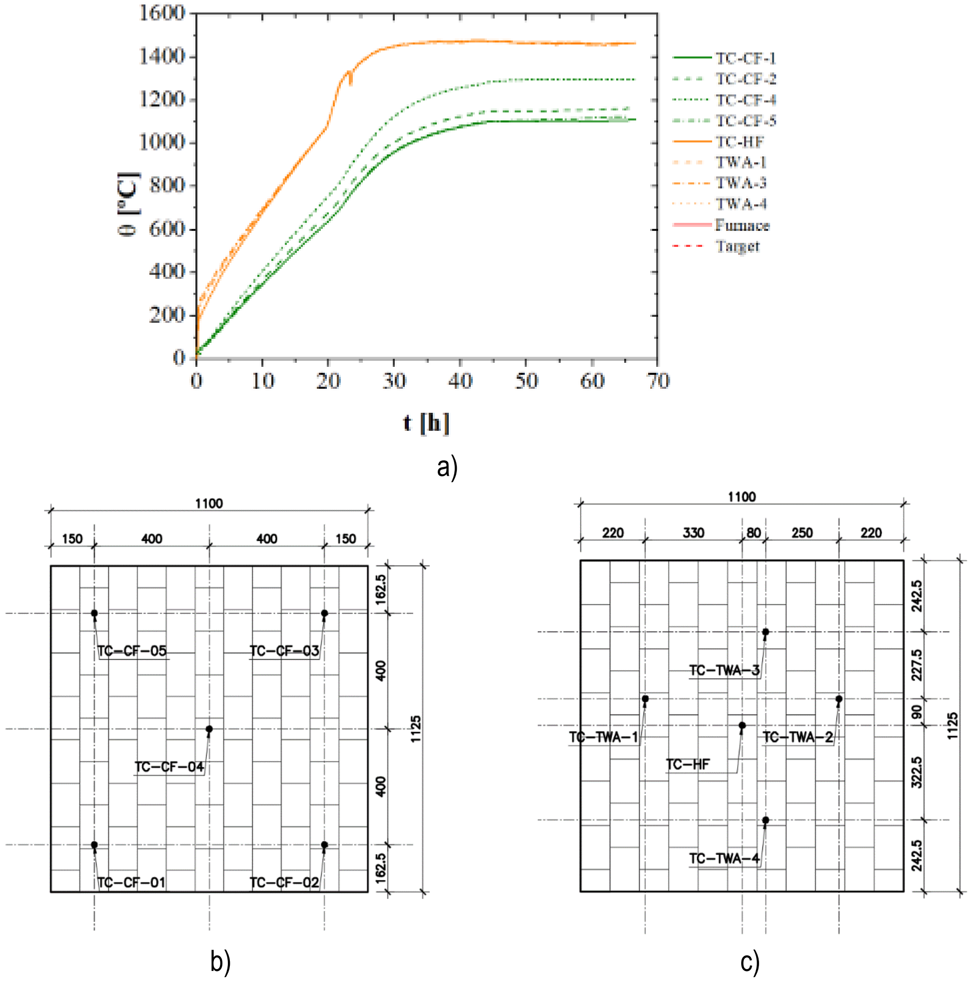


**Figure 98 – Test series S11.HT.RBI – a) Temperatures, b) Thermocouples of the cold face and c) Thermocouples of the hot face.**

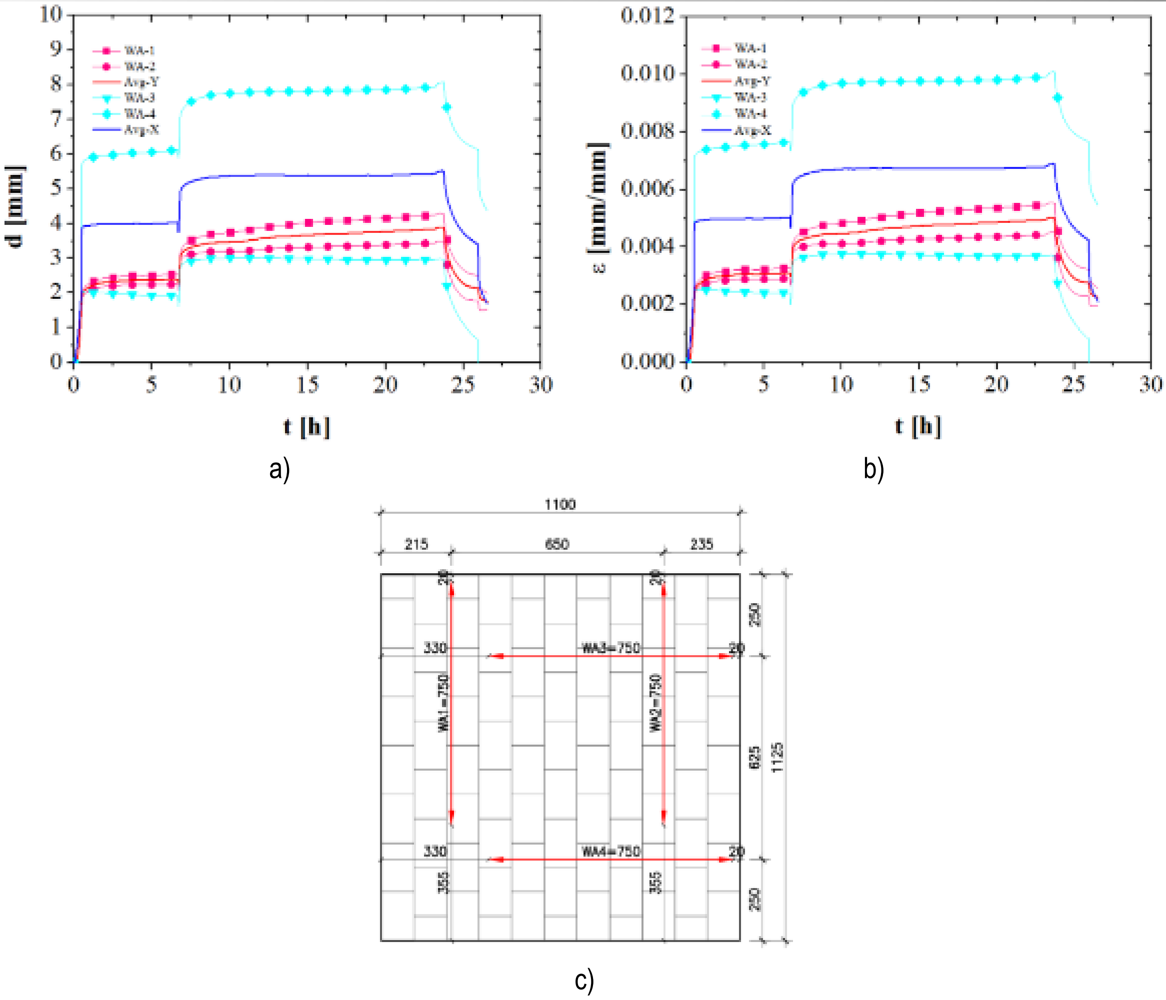


**Figure 99 – Test series S11.HT.RBI – a) In-plane displacements, b) Strains and c) LVDT locations (the X and Y directions, correspond respectively to the direction perpendicular to the bed-joints and the direction perpendicular to the head-joints).**

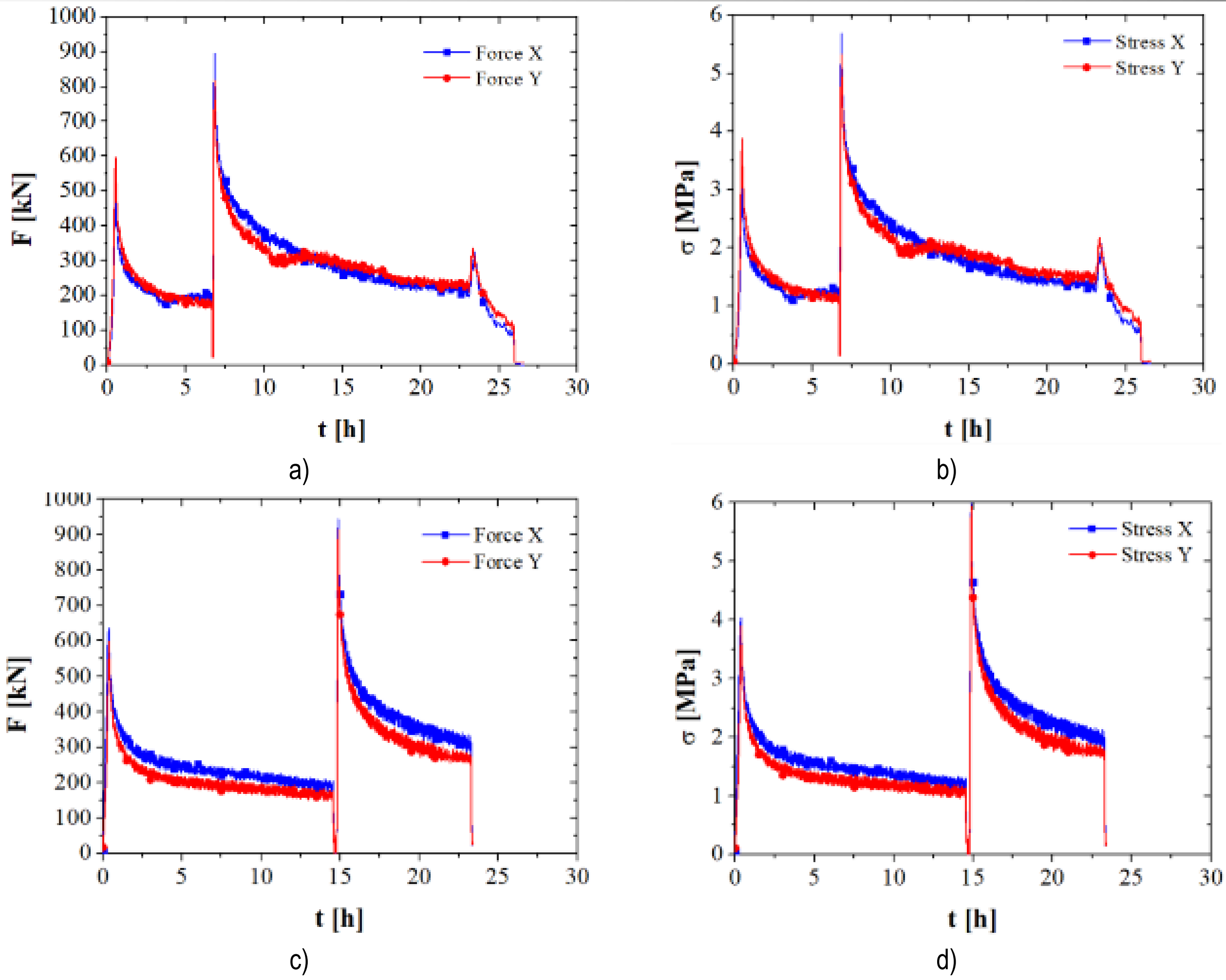


**Figure 100 – Test results of Series S11.HT.RBI:**
**a) Forces S11.HT.RBI.01, b) Stresses S11.HT.RBI.01, c) Forces S11.HT.RBI.02 and d) Stresses S11.HT.RBI.02 (the X and Y directions, correspond respectively to the direction perpendicular to the bed-joints and the direction perpendicular to the head-joints).**

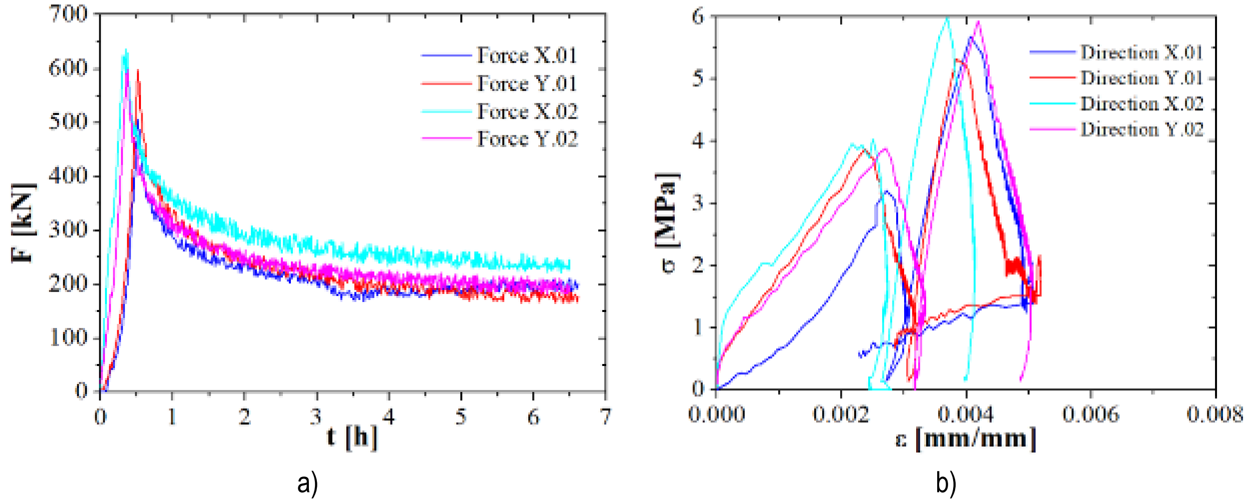


**Figure 101 – Test series S11.HT.RBI: a) Force evolution in the initial 6 hours and b) Stress-strain curves during the two loading sequences (the X and Y directions, correspond respectively to the direction perpendicular to the bed-joints and the direction perpendicular to the head-joints).**

# 4 Conclusion

As observed in the literature, refractory masonry has a highly heterogeneous behaviour resulting in a high scattering of their properties, which was observed in the experimental results. This scatter was found in the experimental results, including the in-plane stiffness, the load-bearing capacity, the temperature distribution, the evolution of the reaction forces and the in-plane and out-of-plane displacements. The heterogeneous behaviour of refractories should be considered in the design of the linings, increasing the safety factors of the structures or using the most unfavourable values for the analysis.

Test series S01.AT.LBC aimed to assess the loadbearing capacity of the specimens. The experimental results showed three different stages of the stress-strain curves: *i*) joint closing state; *ii*) linear behaviour; and *iii*) plastic and damageable behaviour and failure. In the first stage, the stress-strain curve had a parabolic shape, the contact area between the bricks increased with the applied load and consequently the in-plane stiffness of the wallet increased as well. The second stage was evidenced by a linear behaviour on the stress-strain curve, the increasing of the contact area between the bricks and the stiffness increasing of the wallet was no longer significant. In the third stage the plastic effects started to increase, the cracks in the specimen led to a reduction on the wall's stiffness and a brittle failure was observed. The effects of the brick's height imperfections on the uneven stress distribution in the specimen and on the load percolation path was considerable.

Test series S02.AT.CIC aimed to evaluate the behaviour of the walls under cyclic loading. Four load cycles with increasing load level were applied to the specimen. The crushing of initial non-plane bricks' surfaces caused by the mechanical loading were observed and evidenced by the residual strains obtained after each load cycle. The residual strains increased with the load level. The crushing of non-plane bricks surfaces increased the contact area between the bricks, and consequently the wall's in-plane stiffness. Despite the small load level applied to the specimen, some cracks were found in the bricks, caused by the non-uniformity on the load and support conditions of the bricks.

Test series S03.HT.LL8, S04.HT.RTE and S05.HT.LL10 were tested at high temperatures. The temperature evolution in S03.HT.LL8 and S04.HT.RTE were similar, as the specimens of these series had the same geometry. A small scattering on the temperature measurements in the furnace was obtained, most likely caused by different insultation conditions of the experimental setup, however it has no significant impact on the test results. Additionally, some scatter was obtained in the readings of the thermocouples embedded in the bricks. The position of the thermocouples may change during the grouting procedure; therefore, they might end up being installed at slightly different depths. The differences in depth of the thermocouples and the differences in the thermal boundary conditions and exposure to the furnace's resistances in different parts of the wall were responsible for the scattering of this data. Nevertheless, a relatively homogenous temperature distribution was found in the wall.

In the test series S03.HT.LL8, the specimens were tested under a constant load level of 8 MPa. The mechanical load was applied at ambient temperature and a negative displacement was observed, due to joint closure and brick stiffness. When the furnace was turned on, a positive strain rate was observed. The effects of the thermal elongation surpassed the effects of the mechanical loading after 248 minutes on average. A small scattering on the displacements was found during the test. Despite the small load level applied to this test series, cracks were observed in the wall by the end of the tests, caused by the unevenness of loading and support conditions of the bricks. The opening of head-joints was also observed.

Test series S04.HT.RTE was tested with restrained thermal elongation. A mechanical load of 5MPa was applied at ambient temperature, the hydraulic jack was locked in position and the furnace was turned on. The restrained thermal elongation led to a reaction force that increased the stress level on the specimens. By the end of the tests, an average increase of 1.25 MPa was observed in the load. The cracks and head-joint opening observed in S03.HT.LL8 were also obtained. A relatively small scattering was found in the displacement and reaction forces' evolution. In test series S05.HT.LL10 the specimens with higher slenderness ratio were tested under a load level of 10 MPa and the wall failure at high temperatures was observed. The thermal bowing of the specimen, caused by the temperature gradient across the thickness of the wall, resulted in an eccentricity in the load application and led to failure in specimen S05.HT.LL10.02.

Due to limitations in the uniaxial experimental setup, it was not possible to reach service temperatures of the industrial linings in the experimental campaign. The service temperatures of the working lining of steel ladles are around 1650 ºC. The maximum temperatures measured in the specimens were around 900 ºC. A second experimental campaign was developed at RHI-Magnesita, using a biaxial press. Here, different tests were performed: a) at ambient temperature, the specimens were tested under: *i*) uniaxial loading in the direction perpendicular to the bed-joints; *ii*) uniaxial loading in the direction perpendicular to the head-joints, and *iii*) biaxial loading; b) at elevated temperatures the specimens were tested for: *i*) uniaxial creep in the direction perpendicular to the bed-joints, *ii*) biaxial creep, and *iii*) biaxial relaxation.

Test series S06.AT.LBJ aimed to assess the mechanical behaviour of dry-stacked masonry loaded in the direction perpendicular to the bed-joints with restrained deformation in the direction perpendicular to the head-joints. Three load cycles were applied to the samples. As observed in S02.AT.CIC, the crushing of initially non-plane surfaces of the bricks, caused by the mechanical load, was observed. Residual strains were observed after the first load cycle. The crushing of the surfaces resulted in the increasing of the contact area of the bricks and consequently the increasing of the wall's stiffness. Test series S07.AT.LHJ had the same goal of test series S06.AT.LBJ, but the wall was loaded in the direction perpendicular to the head-joints with restrained thermal elongation in the direction perpendicular to the bed-joints. The strain level was lower when compared to the previous series, as the number of joints was smaller. Test series S08.AT.LBI evaluated the mechanical behaviour of the specimens under biaxial loading. When the strains are compared to the strains obtained in the previous series (S06.AT.LBJ and S07.AT.LHJ), it can be seen that the friction between the plungers and the specimens leads to reductions in the strain level, as remarked above.

The goal of test series S09.HT.LBJ was to assess the creep behaviour of dry-stacked masonry loaded in the bed joints' direction. The temperature fields were measured along the test and the temperature evolution may be used for the calibration of numerical heat transfer analyses. The creep effects led to a significant increase in the strains in comparison with the test results from S06.AT.LBJ. Test series S10.HT.CBI assessed the creep behaviour of specimens loaded in biaxial directions. The creep effects led to a significant increase of the strains in comparison with the test results from S08.AT.LBI. The analysis of the stress-strain curves led to the observation that the creep strain during the holding stage is similar in both directions. Test series S11.HT.RBI was designed to evaluate the relaxation effects of dry-stacked masonry biaxially loaded. The evolution of stresses over the duration of the test, led to the observation of the relaxation in the wallet. The experimental result indicated that the relaxation was similar in the direction of the bed joints and head joints. Despite the small load level, all tested samples presented some cracks in the bricks, as was observed in the uniaxial experimental campaign. Most of the cracks were located close to the cross joints, caused by brick height imperfections. The specimens loaded in the head joints showed some spalling close to these joints as a result of stress concentrations.

This document gathers a considerable database on the thermomechanical characterization of refractory linings under different and complex conditions. This database will prove essential for the development, calibration and validation of numerical models aimed at improving the predictive capacity of the behaviour of such installations.

# 5 References


T. Prietl, "Ermittlung materialspezifischer Kennwerte von feuerfesten Werkstoffen und Zustellungen unter uni- und biaxialen Lastbedingungen für die Nichteisenmetallindustrie," PhD Thesis, University of Leoben, 2006, 192 pages.

Prietl, T.; Zach, O.; Studnicka, H. "The evaluation of refractory linings thermomechanical properties". Erzmetall – World of metallurgy, 59, 2006, pp. 127–132

Lopes, R.; Rodrigues, J.P.; Pereira, J.M.; Lourenço, P. B. – "Experimental Research on Structural Concrete Masonry Walls Subjected to Fire", IFireSS 2017 – 2nd International Fire Safety Symposium

Oliveira, R.; Rodrigues, J.; Pereira, J.; Lourenço, P.; Lopes, R. "Experimental and numerical analysis on the structural fire behaviour of three-cell hollowed concrete masonry walls". Engineering Structures, Available online 14 November 2020, 111439

Dupré, J.C.; Doumalin, P.; Belrhiti, Y.; Khlifi, I.; Pop, O.; Huger, M. "Detection of cracks in refractory materials by an enhanced digital image correlation technique". Journal of Materials Science, vol. 53, 2018, pp. 977-993

Belrhiti, Y.; Dupre, J.C.; Pop, O.; Germaneau, A.; Doumalin, P.; Huger, M.; Chotar, T. "Combination of Brazilian test and digital image correlation for mechanical characterization of refractory materials". Journal of the European Ceramic Society, vol. 37, 2017, pp. 2285–2293

ISO 834-1 (1999), Fire resistance tests – elements of building construction, Part 1: general requirements. International Organization for Standardization, Geneva, Switzerland.

Besnard, G.; Hild, F.; Roux, S. ""Finite-Element" Displacement Fields Analysis from Digital Images: Application to Portevin–Le Châtelier Bands". Experimental Mechanics, vol. 46 (6), 2006

Allaoui, S.; Rekik, A.; Gasser, A., Blond, E.: Andreev, K. "Digital Image Correlation measurements of mortarless joint closure in refractory masonries". Construction and Building Materials, vol. 162, 2018, pp. 334-344

Gasser, A.; Terny-Rebeyrotte, K.; Boisse, P. "Modelling of joint effects on refractory lining behaviour". Journal of Materials: Design and Applications, vol. 218, issue 1, 2004, pp.19-28.

Andreev, K.; Sinnema, S.; Rekik, A.; Allaoui, S.; Blond, E.; Gasser, A. "Compressive behaviour of dry joints in refractory ceramic masonry". Construction and Building Materials, vol. 34, 2012, pp. 402-408.

Zahra, T.; Dhanasekar, M."Characterisation and strategies for mitigation of the contact surface unevenness in dry-stack masonry". Construction and Building Materials, vol. 169, 2018, pp 612-628

Ngapeya, G.; Waldmann, D.; Scholzen, F. "Impact of the height imperfections of masonry blocks on the load bearing capacity of dry-stack masonry walls". Construction and Building Materials vol. 165, 2018, pp. 898-913

Teixeira, L.; Gillibert, J.; Blond, E.; Sayet, T. "Creep characterization of refractory materials at high temperatures using the Integrated Digital Image Correlation". Unified International Technical Conference of Refractories, Yokohama - Japan, 2019, pp. 899-902

Kaczmarek, R.; Dupre, J.C.; Doumalin, P.; Pop, I.O.; Teixeira, L.B.; Gillibert, J.; Blond E. and Huger, M. "Thermomechanical behaviour of an alumina spinel refractory for steel ladle applications". Unified International Technical Conference of Refractories, Yokohama - Japan, 2019, pp. 422-425